POLITECNICO
MILANO 1863

Politecnico di Milano
Dipartimento di Elettronica, Informazione e Bioingegneria
Doctoral Programme In Ingegneria delle Telecomunicazioni

Design and Control recipes for Complex photonic integrated circuits

Doctoral Dissertation of:
Maziyar Milanizadeh

Supervisor:
Prof. Andrea Ivano Melloni

Co-Supervisor:
Prof. Francesco Morichetti

Tutor:
Prof. Andrea Virgilio Monti-Guarnieri

The Chair of the Doctoral Program:
Prof. Barbara Pernici

2020 - XXXIII Cycle

تقدیم به خانواده عزیزم

Acknowledgements

Life is what happens when you're busy making other plans.

- John Lennon

Unexpected things happen in life bringing levels of joy and satisfaction that you can not achieve by planing before hand and I am humbled to look at past four years of my life in photonic devices group and deeply believe I would not change it a bit in any other way. Words can not explain how great full I am for this opportunity given to me by Prof. Andrea Melloni and Prof. Francesco Morichetti. They introduce me to the beautiful word of optics and integrated photonics, patiently guide me through it. Thank you for accepting my never ending questions and curiosities and helping me grow in this field.

I would like to thank Nicola Peserico for being the craziest office mate I can ask for and Piero Borga for the most calm and kind one. Special thanks to my dear colleagues Douglas Auguiar, Isis Maqueira, Andrea Annoni, Matteo Petrini, Christian De Vita, Sara Ahmadi, Tiger(s) Jonuzi, Elena Damiani, Francesca Milesi , Alessandro Brugnoni, Nina Codreanu, Riccardo Mazzanti, Daniele Melati, Valeria Donadio for all the launch breaks, aperitivi and specially all the times we tried to make the bosses to go for lunch and avoid Kilomangiaro. I can never forget some memories like understanding Italian politics with Nicola, HW meetings with Douglas, Dracula Castle with Isis, sending first digital packet with Matteo, weird alignments with Sara, finding hair in bonding machine with Elena and many more.

I would like to thank Francesco Zanneto for going through many experiments with me and accepting all my jokes about the electronics problems. I need to thanks Prof. Marco Sampietro and Prof. Giorgio Ferrari and rest of electronics group for all the support in all our joint projects. A special thanks to Clean room staff Claudio Somaschini, Alessia Romeo, Andrea Scaccabarozzi, Lorenzo Livietti and Marco Asa for introducing me to clean room environments and answering my questions on the processes.

I would like to thanks my parents for supporting me through my life, accepting my decisions and helping me in difficult times, Mahbod to be the best brother any one can ask for. To you I will be eternally grateful. At the end, I should thanks my beautiful flower, my beloved wife Shaghayegh for dressing happiness to my life, accepting me as I am and making me feel proud every moment. You always tried to understand my complexities and helped me through difficult times. Merc Jigar.

Milan, Italy.
Oct. 2020.

Abstract

In this work, we present the key ingredients and the best practices for implementing simple, effective and robust control and calibration procedures for arbitrary Photonic Integrated Circuit (PIC) architectures. These procedures are introduced in different phases of PIC integration, from design and simulation to calibration and testing. Through design solutions and techniques we suggest effective approaches to guarantee the performance of the fabricated device in presence of fabrication imperfections and along the desired reconfiguration states. Tuning and calibration recipes like a technique to cancel out the effects of mutual crosstalk among thermal tuners, the exploitation of labeling to identify different optical signals, the use of input modulated signal to automatically reshape the frequency response of the device, offer robust control approaches for PIC. Examples of applications are then illustrated to show the validity and generality of these approaches, namely a cross-bar interconnect of Microring Resonator (MRR)s, Mach-Zehnder Inteferometer (MZI) loaded with MRR as a tunable bandwidth filter, coupled MRR filter and MZI which are implemented in different technologies. Further, the automatic and dynamic generation of the lookup table on Dense Wavelength Division Multiplexing (DWDM) grid is demonstrated and applied to hitless tunable filters. The lookup table achieved with the proposed approach can dynamically update itself to new conditions of the chip or new requirements of operation, such as variations in channel modulation format or perturbation induced by neighboring devices due to a change in their working point. This work is concluded in two final chapters, mixing together all these

receipts to design and control two complex family of PICs and illustrate their performances through different applications. Re-configurable optical add/drop filter capable of Hitless tuning on C+L telecommunication band as the first device and integrated meshes capable of modification and manipulation of free space beams as the second PIC.

Contents

Introduction

The important thing is to never stop questioning and learning.

- Albert Einstein

Photonics can be considered the topic of the twenty-first century if electronics was of the previous one. In particular, the miniaturization of optical components will play an important role in the success of advanced photonics devices, based on optical waveguides. Photonics integrated circuits PIC have applications in variety of areas, such as optical communication, environmental monitoring, biological and chemical sensing, etc. The need of energy per bit reduction and to handle enormous density of data needed to be transmitted at every instance, high-bit-rate communications are dominated by optical transmissions. Today, as optical components continue to replace electronics in variety of applications, the trend is to put more photonic devices onto a single chip. Unlike microelectronics, which have reaped the benefits of size reduction according to Moore's law, PIC have remained approximately the same size over the past ten years. Practical dimensions for optical devices are limited not by minimum lithographic feature sizes, as they are in microelectronics, but rather by the choice of dielectric materials and geometrical structures suitable for low-loss propagation. High refractive index contrast technologies and resonance based devices are pushing PIC towards this goal and are leading to dense and complex devices.

Vast adoption of PIC in different applications dictates tighter and more versatile design needs. In particular tune-ability has became an essential requirement in design process of PIC not only to overcome every-day improving fabrication tolerances but to realize re-configurable devices. This concept gave birth to programmable integrated photonics aiming at design common integrated optical hardware configurations, which by suitable programming, can implement variety of functions. This interest is driven by the surge of a considerable number of emerging applications in the field of telecommunications, quantum information processing, sensing and neurophotonics that will require flexible, re-configurable, low cost, compact and low power consuming devices. Realizing these high demanding complex devices, requires new techniques and approaches both in design and in control phase of PIC production.

Design and control approaches should bind together for development of complex reconfigurable PIC. This means along the design process we need to take into account tunability of the device in different scenario of application and for variety of possible perturbations. In this work, we aim to examine some of these approaches and suggest solutions and recipes to improve the performance of these techniques. In particular we discuss the unavoidable cross talk between the effect of actuators in dense PIC and offer a robust solution to completely remove its footprint in control techniques. Through experimental demonstration on different PICs, we evaluate the performance of cross-talk free systems and exhibits its generality. Chapter 3 is dedicated to develop this concept.

In contrast, Chapter 4 is dedicated to tackle some of the already known problems in complex PIC including signal and device ambiguities to differentiate a channel between DWDM grid or understand the slope of symmetrical frequency response devices. To improve resource and time consuming traditional method in tuning of PIC based on direct reshaping of the frequency response, we suggest using signal optical power as the merit and based on this concept we introduce automatic tuning of tunable and non-tunable devices to different channels. We demonstrate tuned filters based on this idea adapt their frequency response to the power spectrum of the signal. Filter replication, as a direct result of this concept, improves the efficiency in calibration phase of PIC development by offering the direct cloning of the frequency behavior of a golden device to the same family of the structures. We introduce automatic generation of Look Up Table (LUT) for PICs that can dynamically update itself along the operation of the device to new requirement. This chapter is concluded by two packaging and design redundancy solution to reduce the failure chance of large

scale integrated meshes of MZI and reduction of electrical I/O which corresponds to huge design area saving for dense PIC. These techniques are examined on variety of devices on different technologies to demonstrate the generality of the solutions.

This work is brought to end by putting together all the suggested techniques and recipes to design and control two complex family of PICs. Chapter 5 discusses an add/drop tune-able filter based on high order coupled MRR devices. Equipped with nano-second hitless tuning capability and Free Spectral Range (FSR) free response on 100 nm operation band, this device is suitable for telecommunication network nodes on C+L band. Its transparency versus polarization is demonstrated through Bit Error Rate (BER) evaluation on double polarization-100 Gbit/s channels. In despite, Chapter 6 discusses integrated photonic meshes based on MZI to handle and modify free space beams. We introduce self-maintaining close loops of control units capable of tuning and reconfiguration of large scale meshes and analyze their effects on the performance of the free space beams. We conclude this chapter by demonstrating free space beam front compensation via integrated meshes for phase and amplitude scattering mediums in image and far field plain. This concept can be adopted to identify the scattering medium or maintain a diffraction limited channel.

CHAPTER 1

Towards programmable photonics

1.1 Introduction to photonic integrated circuits

In the last decades optical communications contributed to the huge diffusion of the telecommunication market, pushing the development of new technologies to enable higher performances and lower costs. We are witnessing the introduction of the light at every level of the communication network. Long distance links, national backbones and metropolitan networks are equipped with optical fibers that guarantees higher performances and lower costs than older technologies, e.g. radio or coaxial links. In Europe, U.S. and Japan there are projects to introduce fibers also in the short distance links (Next Generetion Access Network) ensuring a great rise of the bandwidth for the final consumer user. Optical bus will be introduced in the next future in the rack backplanes, on the boards and finally also into the chips on the boards, joining electronic devices and substituting them in the information delivering.

Then the photonic technologies are in a very predominant position in the today telecommunication scenario, that becomes the driving force behind the development of photonic integration. For example, optical components become the enabling factors for the optical networks when

a complexity enhancement is required (e.g. where there is the necessity to move from point-to-point links to more complex network structures, introducing advanced all-optical switching technologies). Obviously not only telecommunication area takes advantage of this progress in technology but also different fields such as sensor for physical, medical or civil monitoring.

Photonic integration has a very long history dating back to the '70s. Starting from the first products the trend continued with more complicated structures bringing, in the present day, to the possibility to implement complex functions in very small chips, following more or less the path traced by the electronics some decades before. But at the moment the research on optical components is late compared with the market requests, which show the necessity to integrate a lot of functions on a single chip with very low costs. This generate the great push toward the photonic integration, in particular for PIC with high complexity (in terms of number of components per PIC).

Nowadays, integrated photonics technologies are envisioned as fundamental for applications such as optical communications [1–3], optical interconnects [4–6], bio-sensing [7–9], 5G networks [10, 11] and quantum photonics [12].

Among all the technological platforms that can be used to realize PIC, two semiconductors technologies have been emerging in the last decade: Indium Phosphide and Silicon. Thanks to the high index contrast offered by these photonic platforms, it is possible to integrated a large number of devices on the same chip and to implement complex functionalities for the generation, manipulation and detection of light. Indium phosphide offers the possibility of monolithically integrating on-chip waveguide, detectors, modulators and light sources [13], while silicon allows an unprecedented number of integrated components [14].

To reach the objective of replacing electronic circuits with low power consumption photonic circuits, especially for telecom/datacom applications [15, 16], it is necessary to handle more and more complex functions in the optical domain [17]. To realize such complex functions, photonic circuits must reach an higher level of complexity, interconnecting many photonic devices on the same chip.

Despite the device miniaturization achievable with silicon photonics technologies [18], the integration of these devices is a separated issue [19] that must be challenged to deliver advanced functionalities on photonic integrated chips [18, 20]. This scaled complexity must be matched with the urgent needs of adaptability and programmability to enable the realization

of arbitrary, reconfigurable, complex circuits thus shifting the paradigm from a device-level to a "system-on-a-chip" one.

1.2 The control paradigm

The extreme device miniaturization reached by state-of-the art photonic technologies now enables the realization of hundreds or even thousands of photonic elements in a footprint of less than 1 mm^2 [14]. Although many building blocks potentially provide the required degrees of freedom to realize flexible and arbitrarily complex photonic architectures, reconfigurable optical circuits aggregating many different functionalities are still encountering strong difficulties to emerge. The reason is that in photonics, similarly to electronics, device miniaturization is not synonymous with large scale of integration, and some keys still need to be found to make photonics step up from the current device level to complex, adaptive and reconfigurable integrated circuits.

In other side, PICs are evolving towards on-chip reconfigurable architectures and general purpose programmable photonic processors, enabling the implementation of many different functionalities on-demand [21–24]. These schemes rely on the use of a large number of optical interferometers, such as MZI and MRRs, whose individual working point is inherently related to the phase delay between the interfering optical beams. Therefore, any kind of phase perturbation may substantially affect the overall behavior of the PIC.

To reach these goals, feedback control is mandatory to steer and hold the entire system to the desired functionality, and make it immune to fabrication tolerances, functional and environmental drifts, and mutual crosstalk effects. In fact sensitivity to temperature fluctuations is one of the strongest limiting factors to the exploitation of integrated optical devices. This effect is particularly relevant in Silicon Photonics (SiP), where the large thermo-optic coefficient (TOC) of silicon ($1.8 * 10^{-4} K^{-1}$ at 300 K [25]) is responsible for a wavelength shift of any interference-based device of about $10 GHz \cdot K^{-1}$. In interferometric devices, a waveguide width deviation of only 1 nm can produce a frequency shift of about 100 GHz in the spectral response [26, 27]. Due to this sensitivity, and to the tolerances of current fabrication technologies, the response of fabricated PIC hardly matches the design performance; moreover, it is possible that reconfiguration capabilities will be needed to adapt in real time the circuit to new requirements (i.e. dynamic switching and routing, channels ad-

d/drop and so on). Due to functional drifts and components ageing over time, is not possible to have an accurate and robust control only relying on lookup tables; hence, there is a need of an automatic feedback loop to set the new working point automatically and to control real time the PIC to counteracts unwanted drifts.

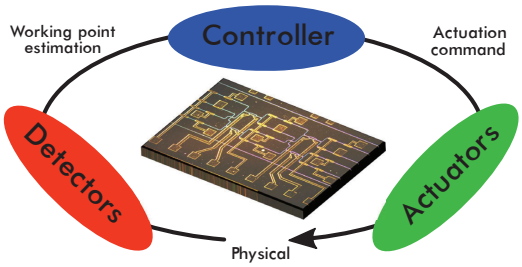

Figure 1.1: *Closed loop control of PIC. The signals from detectors placed in strategic positions throughout the circuits is used by a controller to estimate the current working point. Actuators are then driven to modify the working point of the circuit accordingly to the logic implemented in the controller.*

The paradigm of a feedback loop for integrated photonics is shown in Fig. 1.1. One or more detectors (see Sec. 2.2) are placed in strategic positions throughout the circuit; these detectors, which can be fast or slow depending on what is being measured, generate control signals proportional to the measure they are performing. A controller reads the control signals and estimates the working point of the PIC based on the information provided; the controller then drives the actuators to steer the working point accordingly to the algorithm implemented in the controller itself. The actuators rely on physical effects to modify the working point of the PIC (see Sec. 2.3). Conveniently, control systems should be low cost, energy efficient, insensitive to fluctuations of the optical power, applicable to both passive and active devices, and should not require additional photonic structures.

Optical Design and control approaches should bind together for development of complex reconfigurable PIC. This means along the design process we need to take into account tunability of the device in different scenario of application and for variety of possible perturbations. In this work we study some of these techniques and introduce new approaches to design and control complex PICs, reconfigurable along the operation band.

1.3 Key proposed innovative concepts and the state of the art

The work reported in this thesis has outcomes in diverse areas under the Integrated Photonics umbrella. Solutions and techniques from design to calibration and control phase of PIC implementation are discussed and analyzed through numerical simulations and experimental trials of different functions implemented in multiple technologies.

- **Thermal crosstalk free system**
  Chapter 3 discuss the idea of cross talk between effect of actuators in PIC. For the example of thermo-optic actuators, due to heat flow from actuator to other parts of chip, perturbation is introduced in unwanted places of circuit from each actuator. To mitigate this perturbations other heaters need to change their working point which lead to other perturbations which in some cases can cause instability in control algorithms. Several solutions have been proposed to mitigate thermal cross-talk on a photonic chip. Thermal isolation trenches allow the localization of the heat around the actuated waveguide and can also improve the heater efficiency [22] [28]. However, this approach puts some constraints on the layout and footprint of the PIC. In this work we suggest instead of individual modifications of actuators, they are modified by specific weights which are obtained from eigen-solution of the coupled system (introduced as Thermal eigenmode Decomposition (TED)). Through numerical simulations and experimental trials we examine the efficiency of this technique. We suggest an effective technique to evaluate coupled system to deliver the optimum cross-talk cancellation with TED based techniques.

- **Tuning to signal spectrum**
  Section 4.2 discuss a new approach in tuning algorithm to identify the progress of the algorithm. Traditionally, PIC tuning is implemented targeting a specific frequency response. This approach can be valuable for testing, and pre-calibration procedures, but it is not practical for automated tuning of the PIC during its operation because it is resource and time consuming. For instance, it may require a tunable source and/or a spectrum analyzer to monitor the response at wavelengths of interest. Likewise, time domain approaches, based on the measurement of the BER or eye diagram distortion, require considerable load of Digital Signal Processing (DSP) as well as electrical power consumption. In any case both approaches are hardly practical when the device is in use. In this work we suggest using the Power Spec-

tral Density (PSD) of the channel as merit in tuning algorithm and we demonstrate through experimental trials we can tailor the frequency response of the filter , even if its not design to be modified, to the PSD of the channel, finding the best filter tuning condition for that specific channel. Using the optical power at the output of a golden filter (filter with acceptable frequency behavior) we can tune the same family of devices. In other words replication of filter frequency response which can save time and resource in calibration phase of PIC implementation. In section 4.1 we discuss extension of this idea forcing devices to operate on specific channel through Wavelength Division Multiplexing (WDM) grid via labeling technique.

- **Automatic calibration and dynamic look up tables**
  Based on the concept of using signal optical power in tuning and filter replication, in section 4.3 we introduce dynamic LUTs which can be automatically created for arbitrary PIC. They can be updated due to new requirements of the operation or new conditions of the chip like perturbations from neighboring circuits. Traditionally PICs are kept in their optimum working point through pre-defined tables which are expensive to produce during the calibration of the device. These tables need to be updated due to aging of the device or new requirement of the operations. We suggest adopting TED-based algorithms while using optical power of the channel to automatically create these tables and through locking algorithms these LUTs are updated matching new conditions of operations.

- **Reduction of electrical I/O**
  Electrical bonding pads, responsible for electrical I/O occupy huge area of photonic chips, their size can not be decreased due to mechanical limits of wire bonding techniques [29]. This dictates complex assembly techniques for large PICs like flip chip [30] approaches which other than being expensive have their limitations. In this work, we suggest two approaches to reduce the electrical connection needed to operate and control PICs. Section 4.5 discuss implementing electronic multiplexer in optical chip to reduce needed electrical lanes as the first solution and grouping together optical waveguides and use common detector as the second one. In this approach the sum of optical power from monitor ports of PIC is measured and needed to be carried out of the chip. Labeled signals can be used to distinguish through a demodulation of the measured signal at the controller side out of the photonic chip.

- **FSR free and hitless-tunable Pol-Div filter**
  Chapter 5 introduce high order coupled MRR filter with exceptional features. Implemented in SiP platform, we recorded spurious free FSR on 100nm wavelength range centered in C band in both Drop and Through port. It can be reconfigured transparently (hitless tuning) on this wide operation band in nano-second time scale without introduction of any perturbation. This filter is implemented in polarization diversity scheme, demonstrating polarization transparency for the hole operation band. Its performance is evaluated in experimental trials specifically while adding and dropping two 100 or 200 Gbit/s double polarization channels with complex modulation scheme. Multiples of this filter can be implemented to operate on the same optical bus to add and drop channels from DWDM grid with operation range wider than extended C band. To the knowledge of the writer such a device with all these features does not exist in state of the art.

- **Free space beam manipulation**
  Chapter 6 discusses the integrated meshes based on MZIs. A standalone control technique capable of steering and maintain the performance of these meshes are introduced and examined through experimental trials. Consequence of control algorithms on the performance of optical antenna array connected to these meshes are studied and design solutions are offered to reduce residual perturbations. These meshed are adopted to modify and alter free space beams to establish free space links. Through experimental trials applications including beam steering, automatic free space coupling and source identification is demonstrated using these meshes. Using integrated meshes, free space beam is modified to compensate the effect of scattering mediums and masks in image plain or far field beam to reconstruct the free space link. To the knowledge of the writer this is the first time these devices are used for free space applications and results are appreciable comparing to optical phase array antennas. Comparing with phase array antennas with these meshes not only an straight forward power minimization automatic tuning is achievable, due to the access to array elements amplitude, these circuits can obtain more sophisticated free space beams and introduce vast level of correction.

1.4 Thesis overview

- **Chapter 2: Building Blocks**
  In this chapter building blocks and concepts required to implement a complex PIC are presented. Covering building blocks to implement a control layer to maintain and modify the frequency behavior of these devices including detectors and actuators as eyes and hands of control system, electronics as the control processor and signal carrier. At the end, brief discussion on some fundamental optical building blocks needed for following chapters.

- **Chapter 3: Thermal crosstalk free system**
  This chapter is devoted to discuss and analyze unavoidable mutual coupling between the effect of actuators presence in PIC. It includes introduction of the coupled system specifically for thermo-optic actuators and offer a solution (introduced as TED) to cancel the effect of this coupling in control techniques. Efficiency of this technique is studied through numerical simulations and experimental trials. This chapter is concluded in solutions to measure and estimate the coupled system to be adopted in TED based algorithms to obtain most optimum cancellation of cross-talk effects.

- **Chapter 4: Techniques and recipes**
  This chapter introduce some techniques and modifications applicable in design and control phase of PIC implementation to guarantee a re-configurable and robust device. Techniques to distinguish an optical channel in presence of WDM grid by using only optical power or recognizing the slope side of a frequency symmetric device. In this chapter we suggest using the optical power of the channel as merit in tuning algorithm which allows us to tailor the frequency responce of the device to PSD of the channel. This concept is developed to introduce dynamic LUTs which can update themselves upon variation of the operation needs or requirements. Filter replication, as a solution to improve the calibration performance, is introduced based on this concept. This chapter is concluded by two design tricks to increase the resilience of the PIC against fabrication tolerances and reduce the footprint of electrical I/O on the optical chip area.

Last two chapters include approaches following the recipes introduced in previous ones to cook two complex family of PICs and demonstrating interesting applications through re-configuration of them.

- **Chapter 5: FSR free and hitless-tuneable filter**
  This chapter introduce a FSR free, hitless tune-able and polarization insensitive filter capable of adding and dropping channels from DWDM grid. We introduce design steps to obtain a tune-able and resilient device for 100nm of wavelength operation. An interesting design approach to obtain n-sec time scale and perturbation free hitless disconnection and a polarization diversity scheme to operate double polarization channels. Performance of this device is examined in experimental trials, specifically through BER measurements of added and dropped 100 and 200 Gbit/s Pol-Div channels with complex modulation schemes.
- **Chapter 6: Free space beam manipulation**
  Device of this chapter is an integrated mesh of MZIs capable of manipulating and modifying free space beams to either satisfy the new requirements of free space communication or compensate for the presence of random perturbing mediums in the path. After studying different mesh structures, we suggested design techniques and control approaches for these devices to satisfy desired requirements and demonstrated these results through experimental trials. Applications including free space beam coupling and source identification, compensation of scattering mediums and perturbation masks in image plain and far field beam.

CHAPTER 2

Building blocks

2.1 Introduction

In this section fundamental building blocks and concepts required to implement the complex PIC discussed in the next chapters are presented. Including building blocks to implement a control layer to maintain and modify the frequency behavior of these devices. These concepts are general and needed to be adopted to implement arbitrary PIC along their control layer. We start by the sensors to measure and evaluate the condition of the PIC including photo diode and transparent detectors for integrated circuits and camera for free space beams in Sec. 2.2. Actuators to force the corrections dictated by control system are discussed in Sec. 2.3 in particular based on thermo-optic and plasma dispersion effects. In Sec. 2.4 we discuss electronic circuitry needed to carry electrical signals and process the information as the last ring in the control chain. This chapter is finished by introducing and evaluation of particular photonic circuitry components needed to realize complex PIC that are discussed in the following chapters. These elements include Optical I/Os, waveguide crossings to realize junctions in planner photonic platform and integrated polarization management components. Section 2.5 is dedicated to introduce and eval-

uate the performance of these building blocks.

2.2 Detectors

A key element of the photonic circuits control chain is the detector. They are responsible for converting information that lies in the optical domain to the electronic signals meaningful for controller. The ability to monitor not only how much, but also which light is propagating in the waveguides is crucial.

Optical detectors can either be fabricated in wave guiding or non-wave guiding form and in either case, the most common type of semiconductor optical detector is the depletion layer photo-diode [31]. The main figures of merit for such devices are sensitivity, response time, quantum efficiency and power consumption [31].

For the control and operation of complex photonic integrated circuits, on-chip and waveguide-based optical power monitors are essential components. These integrated detectors allow for diverse functions on a chip including, but not limited to, routing and switching of optical channels [32, 33], self-configuring PICs [20], thermal tuning and wavelength locking of filters and modulators [34, 35].

In the following we discuss three families of detectors each (or together) suitable for different optical functions. Integrated circuits can use integrated photo detectors or transparent detectors while free space optical beam can be detected and characterized by camera.

2.2.1 Photo detector

Waveguide integrated photodetectors are already commercially available in both Silicon (Si) [36] and Indium Phosphide (InP) [37] foundries. The photodetectors used in conjunction with directional couplers or filters allow for the monitoring of signals by tapping some of the photons of the signal and using them to measure channel power. The overall dimension of a monitor based on intrusive monitoring depends on the technology, but the designer always has to consider both the space required by the photodetector and the directional coupler required to tap some of the photons of the signal to be measured. The addition of active layers in a fabrication process always involves the use of additional lithography masks and process steps, which in turn increases the cost and the required process time of a wafer run.

In SiP fabrication processes Germanium (Ge) is a typical material that is used as absorbing material. Typically a Ge layer is epitaxially grown on

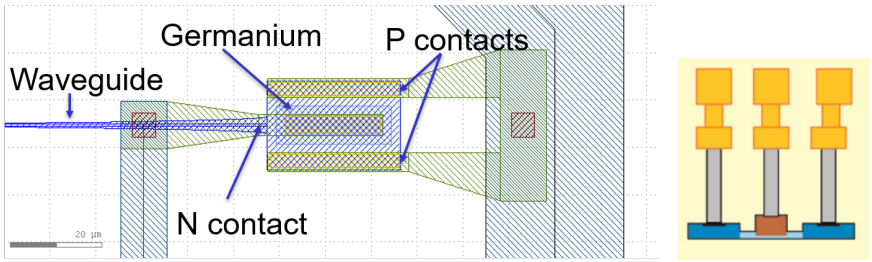

(a) *GDSII* **(b)** *Cross section*

Figure 2.1: *Waveguide Germanium photodiode integrated in SiP platform*

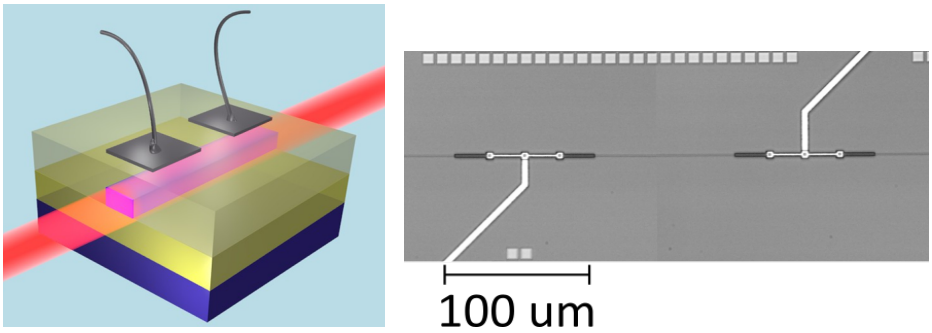

(a) *Schematic diagram of the CLIPP* **(b)** *Microscopic image of the CLIPP*

Figure 2.2: *CLIPP schematic and photo*

top of the waveguide layer. The Graphic Database System (GDSII) layout of a germanium photodiode for the 1550 nm wavelength range is shown in Fig. 2.1(a), and its cross sectional view shown in Fig. 2.1(b).

2.2.2 Non-invasive detection

One alternative to the use of intrusive channel monitoring is the use of monitoring techniques that take profit of the effects that are already experienced by the propagating field. The ContactLess Integrated Photonic Probe (CLIPP) [38] is an example of such a device. The CLIPP makes use of the free carrier generation induced by photon absorption occurring in the surface of the semiconductor waveguide core, such as Si or InP [39] [40]. A diagram of such detector is shown in Fig. 2.2a.

A great advantage of such technique is that it allows for an optical measurement that does not need an active material to be deposited or grown on the waveguide layer. This reduces substantially the manufacturing costs of the run since only a standard metal pad is required to be placed on top

of the waveguide.

While the CLIPP is completely non-invasive, in the sense that capacitive access to the waveguide is used, other devices make use of the same free carrier generation but measure light intensity with direct electrical contact to the waveguide [41]. This approach allows for the measurement of lower optical powers, and faster time responses, however, it requires the use of a rib waveguide and if multiple probes are required to operate in the same waveguide, a proper electrical design should be done in order to avoid electrical crosstalk between the measurements.

2.2.3 Camera

Camera in principle is a planar array of photo detectors tightly placed while being at the focus point of an adequate imaging system. Camera, depending on the frequency band of operation, consists of a sensor fabricated in different technologies. Near IR cameras are often equipped with InGaAs or phosphor sensors technology while visible cameras are commercially build in Complementary Metal Oxide Semiconductor (CMOS) technology in Si. These sensors are kept in Constance temperature via Thermo Electric Cooler (TEC) to stabilize the detection noise.
In this thesis and more specifically in Chp. 6, we use NIR camera Bobcat-640-GigE from Xenics. It has Focal Plain Array (FPA) of 640 X 512 pixels with 20 μm pitch in InGaAs technology. With 14bit of pixel depth and wide range of exposure time (1μs - 40ms) it can cover appropriate dynamic range suitable for free space measurements. It's equipped with a 1" 35mm focal distance objective lens. Using the proprietary software we have access to individual pixel readout with 100 Hz speed allowing to use camera for tuning and calibration of PIC radiating optical beams. Tuning can be done to maximize the optical power at a specific spatial point for example at the place of a receiver. More complex functions can be introduced in control algorithms using camera for example obtaining an specific beam shape like maximizing a main lobe and minimization of the side lobes.

2.3 Actuators

Control algorithms need to alter the performance of the PIC to steer its functionality toward the optimum direction. This modification is done through command signals generated by the controller and applied to the actuators. Actuators depending on the effect they are based on use the current or voltage of the command and change the material properties to

alter the device functionality. They change locally the effective refractive index (n_{eff}) and, consequently, the phase constant (β). Thermo-optic phase actuators are the most common technique in use for slow tuning and calibration. They use the temperature dependence of the refractive index of the waveguide materials to change the phase of the propagating field. Its power consumption and tuning efficiency are highly related to the platform and in SiP is typically below the level of 1 mW/nm [42, 43]. Another option to tune the phase of the propagating field is the use of electro-optical effects in which an electric field applied along a particular crystal axis will affect the refractive index along one or more of the three principal crystal axes. This can be achieved with materials that do not have inversion symmetry and in EO polymers. This includes Lithium Niobate ($LiNbO_3$), III-V semiconductors many optical polymers, but not silicon.

The effectiveness of many other actuators has been demonstrated such as MEMS based switches [44], plasmonic memristor [45], graphene modulators [46], phase change materials [47]. In this thesis we concentrate and use two commonly used techniques based on thermo optic effects (Sec. 2.3.1) and based on plasma dispersion effect (Sec. 2.3.2). Control techniques and recepies in this thesis are demonstrated using one or both of these actuators depending on the technology of the circuit.

2.3.1 Thermo-optic effect

The thermo-optic effect is the capability of the material to change its refraction index as response to a temperature variation. In fact it can be written

$$\Delta n = K_{th}\,\Delta T \tag{2.1}$$

where K_{th} is thermo-optic coefficient and in silicon is equal to $1.86e-4$. Actuator based on this phenomenon is commonly known as Heater. To allow for a large tuning range, the heater design should be carefully considered. The heater temperature is the tuning limiting parameter. Heaters cannot be made arbitrarily thick because of fabrication constraints that limit the layers thicknesses at the order of 200 nm in standard Si foundry platform. Hence, the current density cannot be increased arbitrarily and then electro-migration sets a limit on the operating temperature and current density of the heater.

The design parameters of the heater to be determined are its width, maximum current, and maximum voltage. These parameters are subjected to the limits on the technological platform used. For Titanium Nitride

(TiN), the failure mechanisms are both related to electro-migration and mass transport induced by thermo-migration [48]. This way the designer should consider as constraints both a maximum current density and a maximum temperature during the design process.

To maximize simultaneously the CLIPP (see Sec. 2.2.2) and heater performance in SiP one can use the same layer for both devices and place this layer at 1 µm of the waveguide layer. This distance allows for good heater efficiency without much optical loss, and also allows the CLIPP device to work with a higher access capacitance. In addition, to optimize even further the heater efficiency, the use of deep trenches can be considered since it aids the heating of the waveguide by confining the thermal field around the waveguide. The suggested heater cross section is shown in Fig. 2.3.

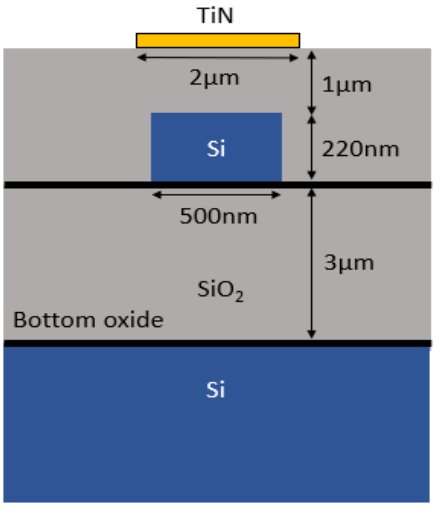

Figure 2.3: *Micro-heater integrated over a waveguide.*

Applying a voltage difference along the heater leads to flow of the current generating power, thus a temperature variation is actuated from this dissipated power. Variation of the temperature changes the material and as consequence a phase shift happens as described by

$$\Delta\phi = \frac{2\,\pi}{\lambda}\,\Delta n\,L_r \;\longrightarrow\; \frac{\Delta\lambda}{\lambda} = \frac{\Delta n}{n}. \tag{2.2}$$

In this thesis, we use this actuator in SiP and Silicon Oxynitride (SiON) technology to modify and correct the frequency behavior of the PIC.

An unavoidable problem in PIC is the mutual coupling between the effect of actuators. It can be inter device coupling (between actuators of a device) or between different devices on a same chip. This phenomenon is described as cross-talk which reduces the overall efficiency of the control algorithms not to mention instability of tuning process. Considering the case of heaters, modifying one heater with the hope of only altering the material beneath that heater cause also modification on the surrounding medium due to the thermal field propagation. In other words, changing heater A affects the working point of heater B (to correct for perturbations caused by A under the heater B), and fixing back the working point of B affects the A. We discuss this problem in details in chapter 3 since it's a limiting factor in integration level of PIC and offer a reliable solution to cancel the cross talk effect. We suggest a general solution applicable for arbitrary PIC or control algorithms.

2.3.2 Plasma dispersion effect

An alternative to thermo-optic effect is the use of plasma dispersion effect to tune the waveguide refractive index. Such change in the refractive index is due to the variation of the free carriers concentration in the waveguide. This is done through a p-i-n junction which is made of an undoped semiconductor (intrinsic) layer between a p and an n-type doped semiconductor. As the two layers are put in contact, fixed charge zone is created (zone with high electric field called "depletion layer") where thermodynamic equilibrium is reached (there is a balance between drift and diffusion processes of the particles/carriers inside the junction).

By applying a forward bias, carriers are injected in the intrinsic layer, thus in the light path. Both the real and the imaginary part of the silicon refraction index change simultaneously, so amplitude and phase modulation of light occur. This effect is called *plasma dispersion effect*. Changes in the real index Δn and the absorption $\Delta\alpha$ in silicon due to free-carriers can be approximated using the Drude model [49] such that

$$\begin{aligned} \Delta n &= -\left(\frac{e^2\,\lambda^2}{8\,\pi^2\,c^2\,\varepsilon_0\,n}\right)\left[\frac{\Delta N_e}{m_{ce}^{*2}} + \frac{\Delta N_h}{m_{ch}^{*2}}\right] \\ \Delta n &= +\left(\frac{e^3\,\lambda^2}{4\,\pi^2\,c^3\,\varepsilon_0\,n}\right)\left[\frac{\Delta N_e}{m_{ce}^{*2}} + \frac{\Delta N_h}{m_{ch}^{*2}}\right] \end{aligned} \tag{2.3}$$

where e is the charge of an electron, λ is the wavelength, c is the speed

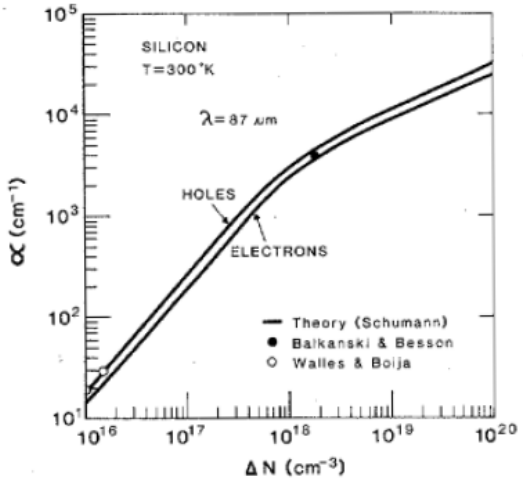

Figure 2.4: *Absorption of Si at 87μm wavelength as function of carrier density [49].*

of light, ε_0 is the permittivity of free space, n is the unperturbed refractive index of silicon, ΔN_e and ΔN_h are the changes in electron and hole concentrations in silicon, m^*_{ce} and m^*_{ce} are the conductivity effective masses of electrons and holes.
This formula can give an estimation (see Figure 2.4) of the change in optical absorption and in refraction index of the waveguide, but the experimental results slightly differ from the model [49]. A rigorous analysis can be done supporting this model with an empirical one. The latter [50] employ a Kramers-Kronig analysis of experimentally measured absorption spectra to estimate free-carrier refraction and absorption for wavelengths from 1.31 to 14 μm in silicon. Experimental data [51] updated in 2011 can be found for Δn and $\Delta\alpha$. In particular for C-band interest

$$\begin{aligned} \Delta n\,(1550nm) &= -5.4 \cdot 10^{-22}\,\Delta N_e^{1.011} - 1.53 \cdot 10^{-18}\,\Delta N_h^{0.838} \\ \Delta\alpha\,(1550nm) &= 8.88 \cdot 10^{-21}\,\Delta N_e^{1.167} + 5.84 \cdot 10^{-20}\,\Delta N_h^{0.838} \end{aligned} \tag{2.4}$$

A change in carrier density affects absorption, which in turn causes an index change through the Kramers-Kroenig relations. Carrier effects are primarily of interest in silicon, where the faster electro-optic effects are absent or very weak. Devices that make use of such effects are usually high-speed ones such as traveling wave Mach-Zehnder (MZ) modulators and microring modulators. These devices are built by constructing a PN junction around the waveguide, in a way that the junction is responsi-

ble for the carrier injection/depletion. The main advantage of this approach is the speed with which the field can be modulated. Fast modulator in [52] demonstrate a 56 Gbps Non Return to Zero (NRZ) system. Similarly, in [53] a 128 Gbps 4-Level Pulse Amplitude Modulation (PAM-4) system was demonstrated by using microring modulator with 10 µm radius.

The device can be easily modeled when operates at constant current. Assuming that every injected electron and hole recombine in the intrinsic region, and the dominant mechanism is non-radiative recombination with a time constant τ_n, a simple model [54] for the carrier density in the device can be provided

$$N = \frac{I\,\tau_n}{q\,V} \tag{2.5}$$

where I is the current, q is the electric charge and V is the volume. This device can be used as Variable Optical Attenuator (VOA) to introduce controllable optical loss. It can be used for power equalization in network nodes between different channels or polarization due to Polarization Dependent Loss (PDL) of the system. In this thesis, we use this actuator to equalize power between two polarization in Sec.5.4 and to attenuate the light inside device to kill it frequency footprint obtaining transparent tuning in Sec.5.3.

2.4 Electronics

In order to successfully operate a complex optical circuit, it is necessary to continuously monitor and tune the working point of each device to counterbalance thermal drifts, aging and to compensate fabrication tolerances and technological non-uniformities. To this aim, sensitive probes of optical power and compact actuators are essential components for the development of an effective photonic chip which are discussed and described in previous sections. An abstract layer that sits on top of the photonic circuit, which we call it the Control Plane, is in charge of using this information and suggest appropriate correction signals. Based on this information and the desired functional requirements, the control unit, both electronics and software, provide to the actuators the signals to steer the PIC towards the correct state.

Appropriate electronics circuitry are needed to connect the inputs and outputs to control layer and to execute the control logic. Input/output

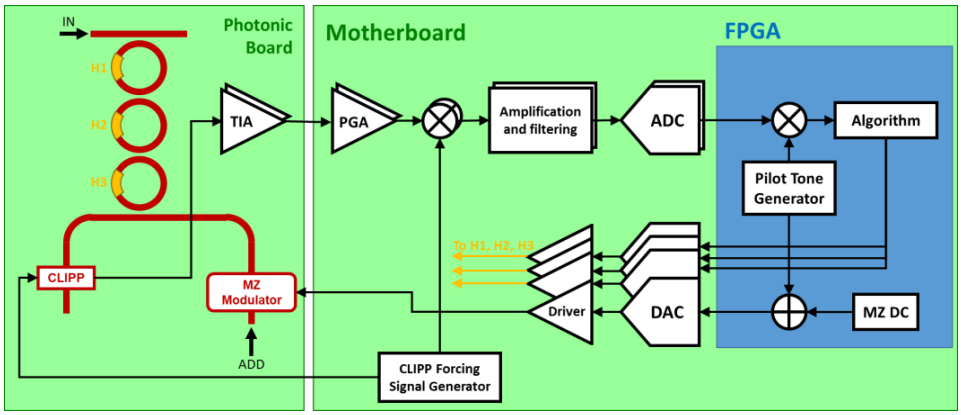

Figure 2.5: *Schematic diagram depicting the control electronics around the photonic circuit.*

signals need to be amplified or buffered to have robust readout or strong command signals. Appropriate low noise amplifier or Trans-Impedance Amplifier (TIA) at the read out of photo diode or CLIPP is critical to maintain the Signal to Noise Ratio (SNR) by not adding electronic noise.

This control loop is complete with a processing and decision making unit which take into account the signals from detectors and apply its decision through forced electrical signals to the actuators. The central processing unit can be implemented a simple PID controller or more complex multi variable optimization approaches like Nelder-Mead simplex optimization technique [55]. This unit can be implemented by DSPs or Field Programmable Gate Array (FPGA) depending on the speed or load of the processing needed.

Control layer can be distributed in different sections of the system. Figure 2.5 presents an example of this layer. Read out circuitry for detectors need to be placed as close as possible to the photonic chip (to maintain SNR) for this aim TIA should be placed by the PIC on the photonic board hosting the chip. Rest of the control layer, including the processing unit and actuators buffers can be placed on a larger and further away board called mother board in this example.

Electrical signals needed to be routed out (or in) of photonic chip to the photonic board through electrical pads. This is a space hungry part of the PIC design. Considering the high cost of PIC fabrication, any attempt to save this space is highly encouraged. In this thesis we suggest some tricks in control algorithm to reduce the needed electrical I/O (Sec. 6.2) and some design solutions to reduce these input/output ports (Sec. 4.5).

2.5 Optical functions for circuit routing

In this section we discuss couple of optical components and functions essential for implementing and managing integrated optical circuits. We start by devices allowing to couple in and out the optical mode from a fiber to the circuit in the integrated chip. We discuss the optical crossings as the routing solution to over populated planner PIC. We briefly discuss variable optical attenuator and relevant components needed to handle and manage polarization.

2.5.1 Optical I/O

In the last few years, a significant amount of work has been done to solve the issue of fiber to silicon waveguide coupling. Broadly speaking the problem can be solved in two ways: horizontal or vertical coupling. The horizontal coupling approach implies the use of a spot size converter to transform the size of the mode of the nanophotonic waveguide to that of the optical fiber by using inverted tapers and Lensed or High Numerical Aperture fibers.

In the vertical coupling approach, the interfacing with the optical fiber is done by redirecting the light exiting the photonic integrated circuit out of the plane of the photonic integrated circuit using a diffraction grating. In this way, the optical fiber interfaces with the silicon photonic integrated circuit from the top, no longer requiring an individuated chip for coupling and testing.

Edge coupling

The key aspect to be addressed when coupling light from a fiber to any waveguide is the overlap integral between the modes. Specifically, in SiP waveguides the large difference in the Mode Field Diameter (MFD) of both modes makes it difficult to create a low loss coupling between both propagating modes. As mentioned, one typical strategy to cope with MFD mismatch is the use of inverted tapers and lensed fibers as depicted in Fig. 2.6(a).

However, some other problems as the one depicted in Fig. 2.6(b) are still faced when using a horizontal coupling. After the dicing of the silicon chips, the silicon substrate may not exhibit a perfectly flat vertical interface at the cross-sectional plane of the waveguides. This is mainly due to the different strategies that are used for dicing and digging the deep trenches. While the dicing is usually done from the backside of the wafer,

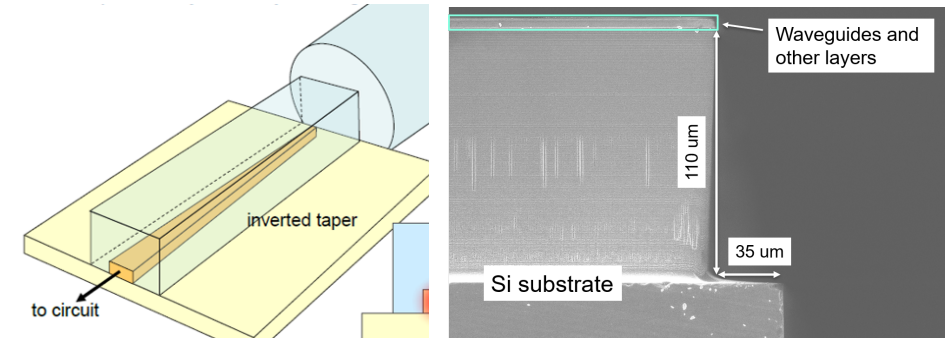

Figure 2.6: *a) Horizontal coupling using tapered waveguides and High Numerical Aperture Fibers. b) Scanning Electron Microscope (SEM) image from the facet of a SiP chip showing the gap that is formed due to misalignment between dicing and deep trench*

the deep trenches are dug from the top, given the need of more precise alignment to the photonic structures in the chip. The result is that the dice lines and the deep trenches are not aligned and that pose mechanical problems to the packaging process since the fibers cannot be placed close to the waveguides. Thus, given the beam divergence along these 35 µm of gap (as in the example of Fig. 2.6(b)) between the Si waveguide and optical fiber, the coupling losses increase even when the mode sizes are matched.

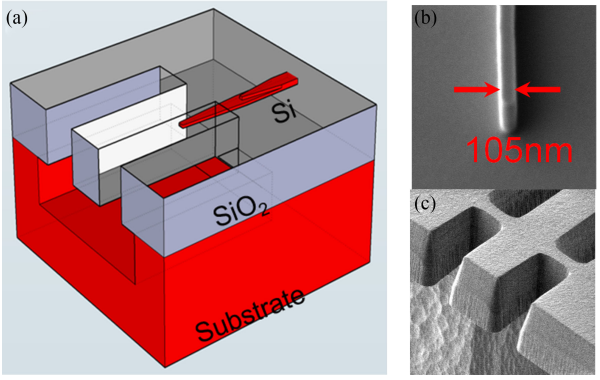

Figure 2.7: *(a) Schematic of the design. (b) The SEM image of the fabricated silicon tip with width of 105 nm. (c) The SEM image of the fabricated suspended oxide waveguide.*

Suspended Couplers

An alternative solution to the integrated tapers is the use of external mode converters fabricated in another technology, such as Silicon Dioxide (SiO_2). The concept includes use of inverse tapered Si waveguide being coupled to a SiO_2 waveguide which is tapered out to expand further the MFD. To provide appropriate guiding medium this waveguide needs to be surrounded with air leading to suspended structures. Figure 2.7 extracted form [56] demonstrates this idea in schematic of (a), SEM picture of the tapered down Si wire in (b) and the facet SEM picture of the suspended structure in (c). Benefit of this structure is coupling loss less than -1.3 dB/-facet with cleaved single mode fiber (SMF) for both Transverse Electric (TE) and Transverse Magnetic (TM) polarization state with a remarkable polarization-dependent loss less than 0.5 dB. Since being suspended structure they are more fragile as presented in Fig. 2.8 SEM picture of broken coupler due to shock induced by chip handling.

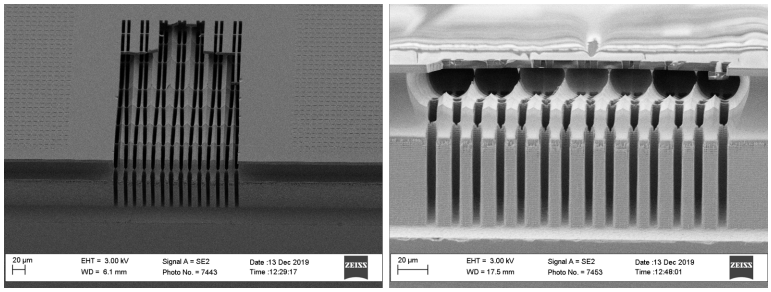

Figure 2.8: *SEM picture of Suspended edge couplers broken due to shock induced by handling the chip.*

Grating couplers

For the single polarization with vertical coupling strategy, curved gratings are the most used technology today. This is an alternative to the straight grating shown in Fig. 2.9(a), which requires a relatively long taper, around 100 µm, after the grating.

Another key advantage of grating couplers is that they are very suitable for wafer level probing since do not require the wafer to be diced to perform optical characterization. The waveguides are optically accessible from the top, eliminating the mechanical issues from the edge coupling strategy as the one shown in Fig. 2.6(b). This way, the alignment of arrays of fibers is facilitated and one can easily use multifiber interposers to access multiple waveguides with a single alignment process. To provide

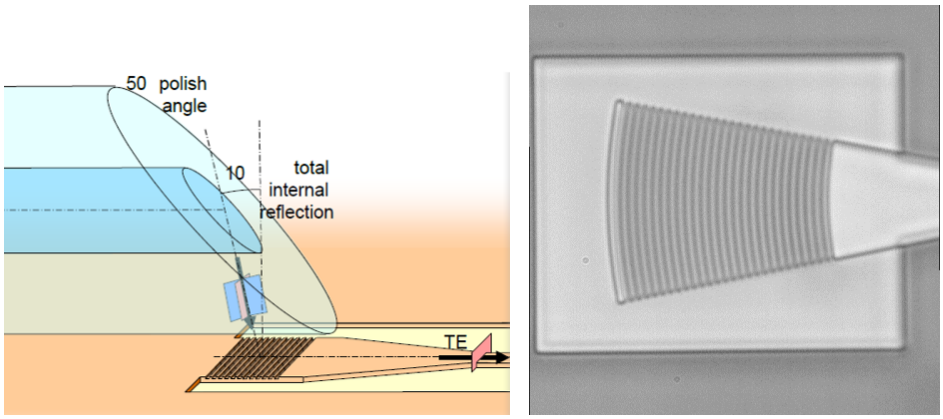

(a) (b)

Figure 2.9: *a) Coupling to SiP waveguide with grating coupler by using quasi planar approach. b) Microscopic image of grating coupler in SiP platform*

a better packaging quality and reliability, an in-plane coupling of fiber to grating couplers can be used, as shown schematically in Fig. 2.9(a). This strategy allows for a compact packaging since the gluing process can be done directly on top of the chip, and the overall dimensions of the packaged device are smaller. An example of such assembly process making use of an array of optical fibers is shown in Fig. 2.10b. In such case, the optical fiber array is glued to the optical chip, assuring a good and reliable mechanical connection between the optical chip and fiber transposer. An alternative is a package as shown in Fig. 2.10(b), in which the fibers are in direct contact with the grating couplers. The main disadvantage of such solution is the relatively high height that is required to accommodate such an assembly. On the other hand, the optical coupling becomes very efficient in terms of optical loss, since no reflection losses are experienced by the optical signal.

Currently all major SiP foundries provide either single polarization or dual polarization grating couplers as part of their Photonic Design Kit (PDK). For operation at 1550 nm typical specifications are a input beam angle of 10°, a grating period of 630 nm, a duty cycle of 50% and an etch depth of 70 nm, from the top of the 220 nm Silicon On Insulator (SOI). Being by design wavelength selective devices, grating couplers have typically a 3 dB bandwidth less than 30 nm.

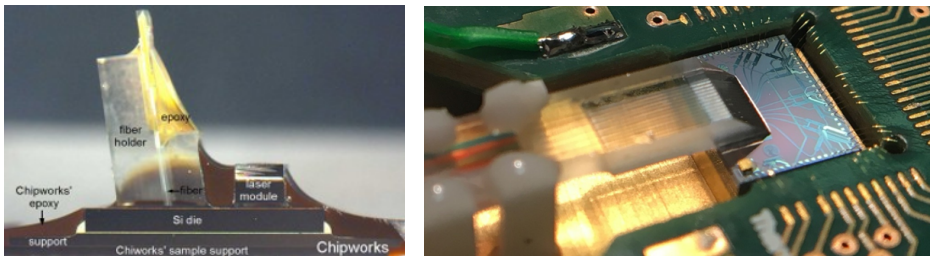

(a) (b)

Figure 2.10: *Use of grating arrays with a) vertical and b) horizontal fiber block coupling*

2.5.2 Crossings

In dense SiP circuits since being limited by planar implementation of the technology, waveguide crossing is an unavoidable building block. These crossings allow for additional degrees of freedom in waveguide routing and are needed in complex PIC for example integrated mesh circuits based on MZI with high numbers of input modes (Chp. 6). Crossings are expected to offer loss less transition for the waveguides with negligible cross talk between crossing waveguides. In particular loss is rising from coupling of the waveguide mode to radiative mode due to the discontinuity (change in dimension of the guide) and cross talk is due to coupling between the modes of the main waveguide and the ones of the crossing waveguide. Here we examine some crossing structures through experimental measurements which are used in design process of complex PIC implemented in Chp. 5 and Chp. 6.

The excess loss and the optical cross-talk introduced by waveguide crossings are experimentally investigated by measuring several different crossing geometries from a test structure, their layout is presented in Figure 2.11. From the bottom to the top of the figure, the test devices include rib waveguides with transitions to channel waveguides (referred to as "tapers"), crossing between channel waveguides, crossing between rib waveguides and crossing between channel waveguides with tapers to rib waveguides. In all the structures, the angle between the crossing waveguides is 90°. Figure 2.12 shows in each panel the total insertion loss of waveguide structures with 20 (orange) and 30 (green) identical crossings in a 70 nm wavelength range around the extended C-band. To set a reference, the insertion loss of a bare waveguide (with neither tapers nor crossings) is considered in blue curve. The reference waveguide is a channel waveguide for channel crossing, while for all the other structures the reference

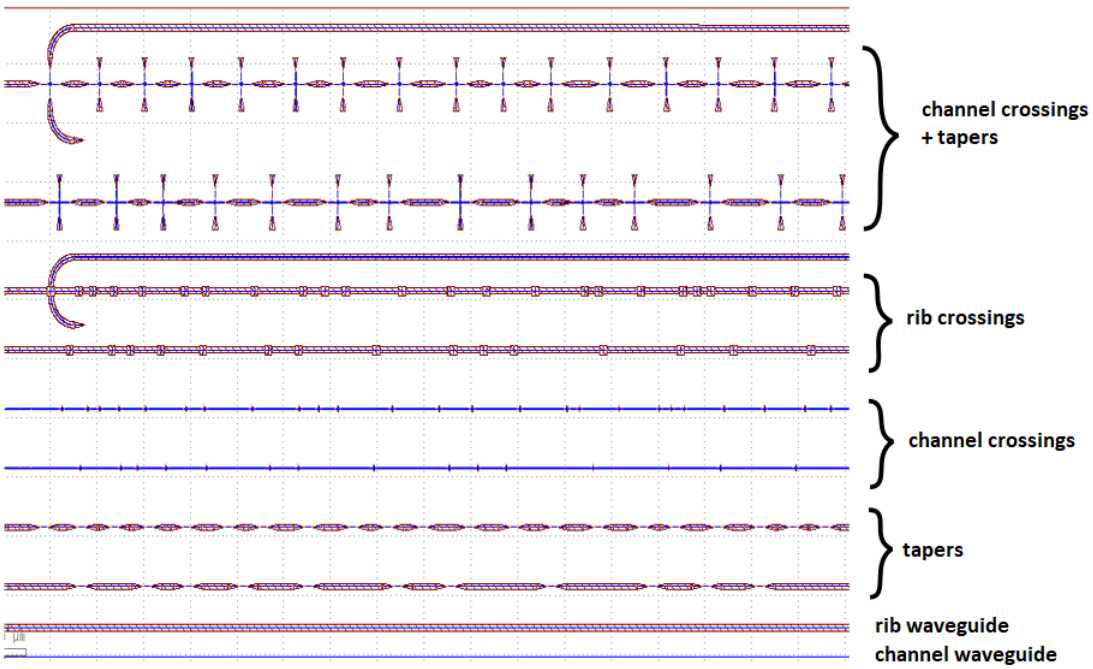

Figure 2.11: *Mask layout of different design of waveguide crossings to evaluate and compare the insertion/cross-talk loss.*

waveguide is a rib waveguide. In all the reported measurements TE polarized light is coupled to the waveguides through suspended tapers and small core fibers. The individual loss of each kind of crossing is reported in Figure 2.13 . The best performance is achieved with channel crossing (red curve), which introduces 0.1 dB (+/- 0.05 dB) loss in the extended C-band. However, the need for tapering the rib waveguide (rib-channel-rib transition) employed for the optical routing of the TOADM architecture in Chp. 5, introduces an additional 0.05 dB loss (blue curve). As a result, the overall loss given by channel crossing + tapers (0.15 dB +/- 0.05 dB) is comparable to the loss of the rib crossing (yellow curve).

The optical cross-talk introduced by waveguide crossing was evaluated using the test structures (see Figure 2.14). For both channel crossing with tapers (red curve) and rib crossing (green curve), the cross-talk power measured at the output port of the crossing waveguide is 35 dB lower than the optical power transmitted in the reference rib waveguide (blue curve) across the entire extended C band.

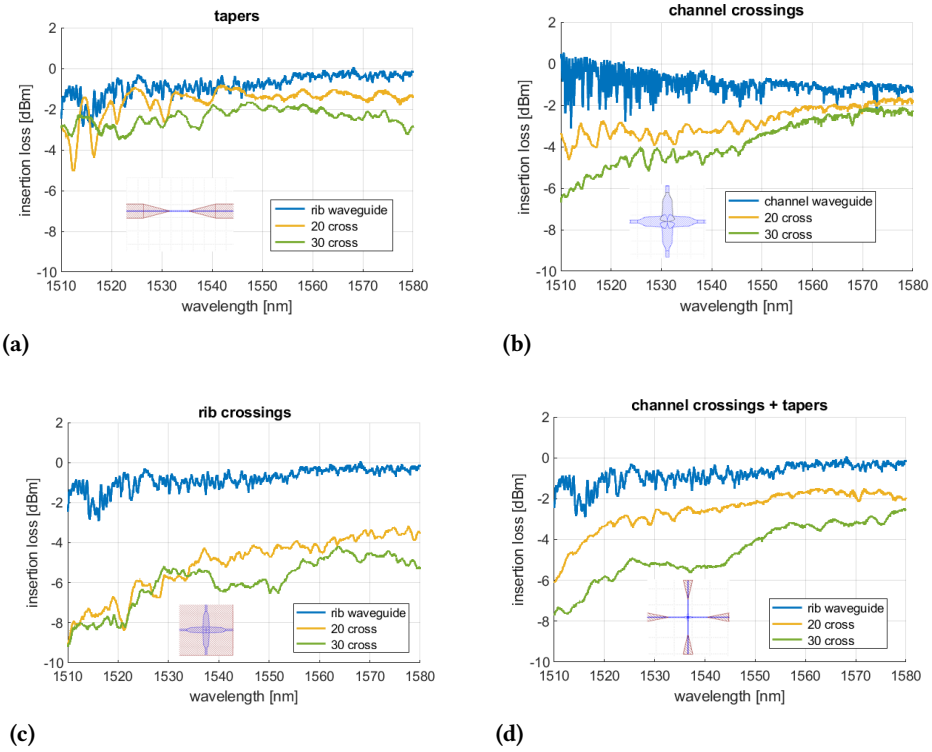

Figure 2.12: *Transmission through waveguides integrating an increasing number of waveguide tapers and/or crossings with a different design: (a) only tapers from rib to channel waveguide; (b) crossing between channel waveguides; (c) crossing between rib waveguides; (d) crossing between channel waveguide + tapers. In each panel, the blue line indicates the reference waveguide (with no tapers/crossing), the orange and the green curves are the structures with 20 and 30 discontinuities (tapers and/or crossings), respectively.*

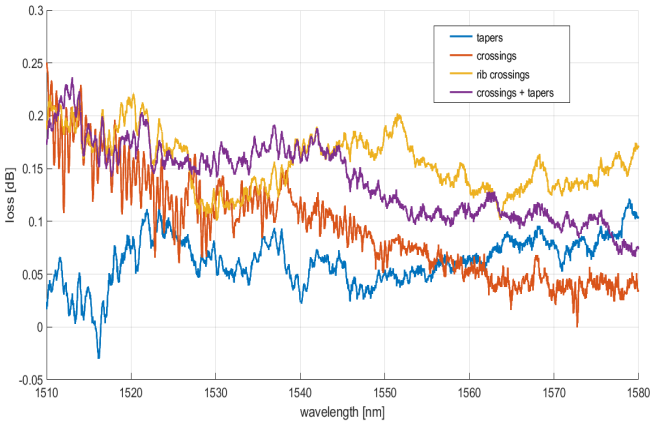

Figure 2.13: *Excess loss of a single taper (blue), rib crossing (yellow), channel crossing (red), taper + channel crossing (purple).*

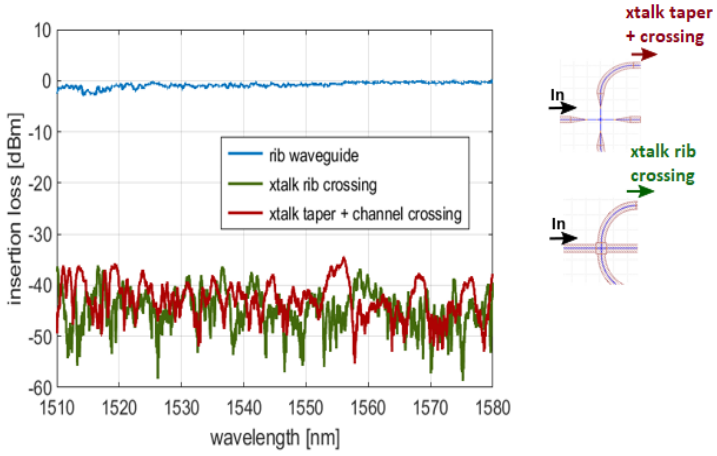

Figure 2.14: *Optical cross-talk of a 90° crossing between two channel waveguides with tapers (red curve) and between two rib waveguides (green curve). Measurements are normalized to the transmission of a reference rib waveguide (blue curve).*

2.5.3 Polarization management

Typical single mode SiP waveguides are 220 nm × 480 nm, and thus, a highly birefringent and very low coupling between the polarization modes is observed. This means that photonic circuits in such platform are typically designed to operate on a single polarization state. For applications which require both polarization states to be processed, *e.g.* WDM filters, receivers, and equalizers, the common approach is depicted in the schematic of Fig. 2.15. The strategy is to split the TE and TM polarized light into two separate waveguides, rotate the originally TM mode into TE and allow them both to propagate in the TE polarization in spatially diverse waveguides while both experience the same propagation environments. Then, two identical circuits are implemented and later both circuits are combined in a polarization combiner.

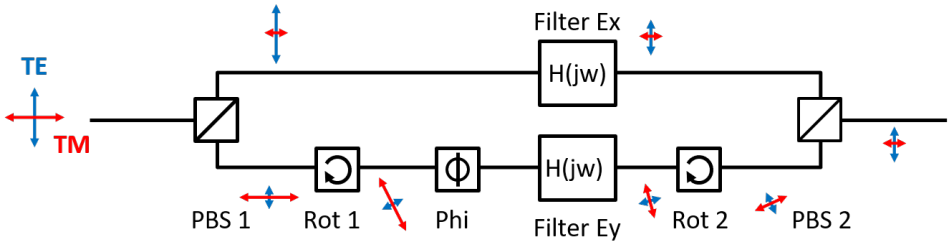

Figure 2.15: *Typical polarization diversity scheme that makes use of a polarization spliter, two identical circuits and a polarization combiner*

The key enabler of this scheme is the polarization splitter and combiners known as Polarization Splitter and Rotator (PSR) and Polarization Rotator and Combiner (PRC). The performance of these devices are evaluated in test structures as presented in Fig. 2.16. Each structure consists of a PSR that is directly connected to a PRC by two straight waveguides. Both devices are standard building blocks provided by AMF foundry [57]. According to the port numbering of these devices, three different port connections were considered, corresponding to the three structures, named "top", "mid" and "bottom", according to their position in the chip.

The main difference among these structures is due to the fact that, according to the information provided by the foundry, polarization rotation occurs for the field at port 2 of the PSR and for the field at port 1 of the PSR. The "bottom" structure where a single rotation occurs at each arm of the polarization diversity scheme is suggested to be the preferred one. Experi-

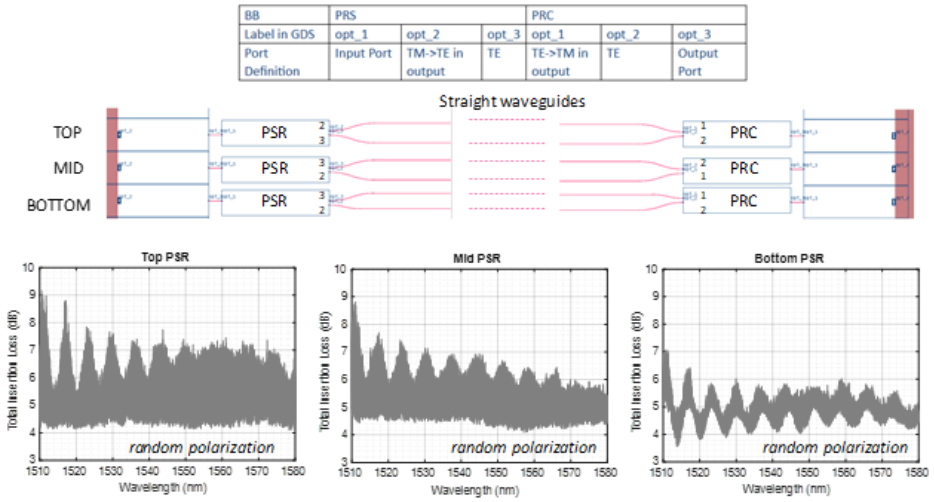

Figure 2.16: *(a) Schematic of the test vehicles employed for the performance assessment of the polarization diversity scheme, consisting of a PSR directly connected to a PRC by two straight waveguides. Different port connections are considered according to the port numbering shown in the figure. (b)-(d)Total insertion loss of the polarization diversity test structure, when the polarization state of the input light is randomly scrambled during the wavelength span.*

mental results shown in Fig. 2.16 confirm the expected performance. Panels (b)-(d) show the total insertion loss of the three structures, measured across a 70 nm wavelength range around the extended C band, when the polarization of the light coupled at the input of the PSR (placed just after a suspended couplers 2.5.1) is randomly scrambled. For the "bottom" PSR (d) a PDL of less than +/- 0.6 dB is observed, where the PDL is defined as the spread of the loss curve around is average value at a given wavelength. For the "top" (b) and "mid" (c) structures the measured PDL increases to more than +/- 1.5 dB.
In Chapter 5 this polarization diversity scheme is combined with a complex filter to realize a broadband polarization insensitive add/drop filter. Details of the scheme along the performance of the system is reported in that chapter more specificatally in Sec. 5.4.

CHAPTER 3

Thermal crosstalk free system

PICs are evolving towards on-chip reconfigurable architectures and general purpose programmable photonic processors, enabling the implementation of many different functionalities on-demand [21–24]. These schemes rely on the use of a large number of optical interferometers, such as MZI and MRRs, whose individual working point is inherently related to the phase delay between the interfering optical beams. Therefore, any kind of phase perturbation may substantially affect the overall behavior of the PIC. Phase perturbations are naturally originated by tolerances of the fabrication process, owing to the sensitivity of the effective index of the optical waveguides to nanometer-scale dimensional variations [26, 58]. Moreover, time-varying phase drifts may also be caused [58] by temperature changes induced by environmental thermal fluctuations or by heat sources integrated onto the same photonic chip [30, 35, 59].

To compensate against phase errors as well as to reconfigure and stabilize the working point of a PIC, actuators capable of controlling actively the phase in optical waveguides are required [60–63]. Thermal actuators are a well-established approach [64, 65] however, thermal actuators can induce mutual thermal crosstalk between neighbor actuated waveguides and thus can impair the efficiency of control procedures employed for PIC

tuning and stabilization.

Several solutions have been proposed to mitigate thermal cross-talk on a photonic chip. Thermal isolation trenches allow the localization of the heat around the actuated waveguide and can also improve the heater efficiency [22] [28]. However, this approach puts some constraints on the layout and footprint of the PIC and is not exploitable for closely spaced devices, as in the case of coupled MRRs. Athermal optical waveguides have been demonstrated by coating the waveguide core with a material with a negative thermo-optic coefficient (TOC) [66, 67] yet, reducing the temperature sensitivity of the waveguide prevents from the possibility to perform active thermal tuning. Thermally self-compensating MZI were fabricated by adopting different geometries for the two arms of the interferometer [68] or operating on orthogonal polarization states [69]. While being effective, this approach is circuit-specific, and hence hardly scalable to generic PIC architectures.

In this chapter we present a novel method, that we named TED, which is not a control algorithm but a technique that can be adopted in control algorithms to cancel out the effects of thermal crosstalk in arbitrary PICs where thermal crosstalk is indeed physically present. In other words, the TED concept is neither circuit-specific, nor algorithm specific. In Sec. 3.1 we introduce the main concepts and the theory of the TED method, together with an example of tuning algorithm where it can be used. To demonstrate the effectiveness of the TED method on generic PICs, numerical simulations are presented in Sec 3.1.1 on two well-known architectures, namely a coupled MRR filter and an MZI switch fabric. Experimental results on a coupled MRR filter are reported in Sec. 3.1.2, providing a clear evidence of the benefits of the TED method, with respect to conventional control strategies used for the tuning and wavelength. At the end, in Sec. 3.2 we present some insight in to the thermal cross-talk system and practical techniques to evaluate the system describing matrix leading to the optimum thermal cross-talk cancellation using TED.

3.1 Thermal eigenmode decomposition

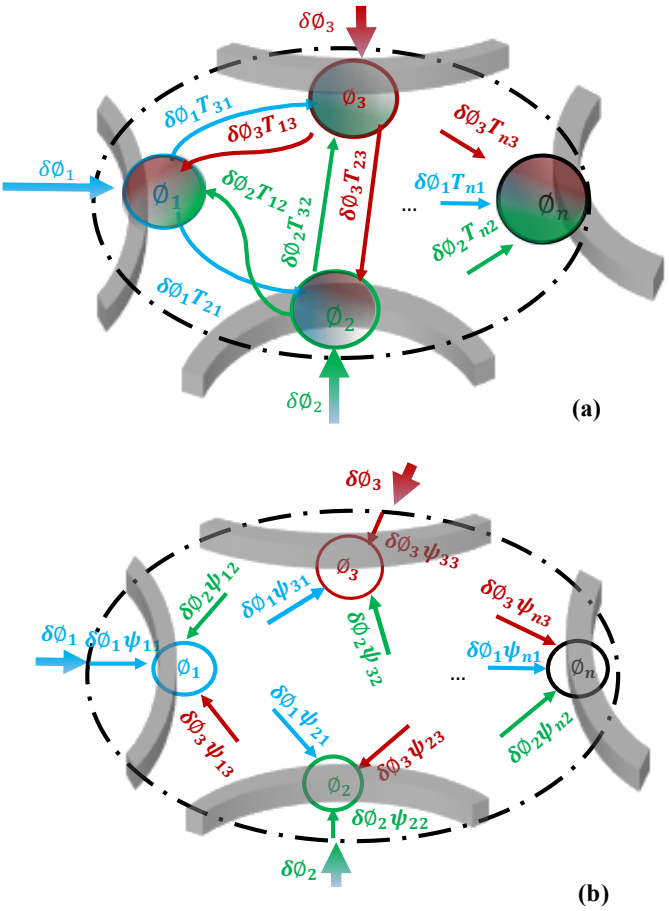

Figure 3.1: *(a) Schematic representation of a PIC integrating N phase actuators in the presence of phase coupling induced by thermal cross-talk. (b) TED concept: the effects of thermal cross-talk are canceled by simultaneously driving all the coupled actuators according to the eigenmodes of the thermally coupled system.*

To illustrate the concept of the TED method, let us consider the schematic of Fig.3.1(a) showing an arbitrary PIC consisting of N optical waveguides with a thermal actuator integrated in each of them. The status of the circuit is identified by the phase vector $\Phi = [\Phi_1 ... \Phi_N]^T$, where ϕ_n is the current phase in the n-th waveguide. When an electrical power is applied to the n-th actuator, it is expected to introduce a desired phase change $\delta\Phi_n$ to the n-th waveguide where the actuator is integrated, with no effects on the surrounding waveguides. However, due to thermal cross-talk, some

phase perturbations are also introduced in the other waveguides. Considering Fig.3.1(a) the actual phase shifts $\delta\tilde{\Phi} = [\delta\tilde{\Phi}_1 \cdots \delta\tilde{\Phi}_N]^T$ induced in each waveguide is given by

$$\delta\tilde{\Phi} = \begin{pmatrix} T_{11} & T_{12} & T_{13} & \cdots & T_{1n} \\ T_{21} & T_{22} & T_{23} & \cdots & T_{2n} \\ T_{31} & T_{32} & T_{33} & \cdots & T_{3n} \\ \vdots & \vdots & \vdots & \ddots & \vdots \\ T_{n1} & T_{n2} & T_{n3} & \cdots & T_{nn} \end{pmatrix} \delta\Phi = \mathbf{T}\delta\Phi \tag{3.1}$$

where $\delta\Phi = [\delta\Phi_1 \cdots \delta\Phi_N]^T$ is the desired phase shift and $\mathbf{T}$ is the phase coupling matrix taking into account all the self (diagonal) and cross (off-diagonal) phase shift contributions.

Without loss of generality, all the diagonal terms can be assumed unitary, that is $\mathbf{T}_{nn} = 1$. The phase coupling coefficient $\mathbf{T}_{nm}$ between the $n-th$ actuator and the $m-th$ waveguide depends on the PIC topology, photonic platform and not on the status of the circuit. When applying control algorithms for the automatic tuning of the PIC, mutual phase perturbation among thermal actuators must be compensated. However, individual corrections of each phase change $\delta\tilde{\Phi}_n$ is not an effective method for controlling the system. First, this would require for each actuator the need for post-compensating the thermal crosstalk that has been introduced by other actuators at previous steps, thus leading to a substantial increase of the number of iterations required to steer the PIC to the desired working point. Second, as shown in the following of this thesis, the convergence of the algorithm itself could be severely impaired.

To circumvent this issue, the proposed TED method provides a strategy to cancel out the unwanted effects of thermal crosstalk on the actual phase shift applied to the optical waveguides. Mathematically, the concept is extremely simple because it is essentially a coordinate transformation, mapping the phase variables Φ, which are (thermally) coupled by the $\mathbf{T}$ matrix, into a suitable set of uncoupled phase variables $\delta\Psi = [\delta\Psi_1 ... \delta\Psi_N]^T$, for which the phase coupled matrix $\mathbf{T}_D$ becomes diagonal. Assuming $\mathbf{T}$ to be diagonalizable, we can write

$$\delta\tilde{\Phi}_n = \mathbf{P}\mathbf{T}_D\mathbf{P}^{-1}\delta\Phi \tag{3.2}$$

where $\mathbf{P}$ is a matrix whose columns are linearly independent eigen-vectors of $\mathbf{T}$, $\mathbf{T}_D$ is the diagonal matrix containing the corresponding eigen-values, and $\mathbf{P}^{-1}$ is the inverse matrix of $\mathbf{P}$. Multiplying both sides by $\mathbf{P}^{-1}$ we obtain

$$\delta\tilde{\mathbf{\Psi}}_{\mathbf{n}} = \mathbf{T}_D \delta\Psi \tag{3.3}$$

where

$$\delta\mathbf{\Psi} = \mathbf{P}^{-1}\delta\Phi \tag{3.4}$$

is the phase shift imparted to the transformed phase variables Ψ. Since $\mathbf{T}_D$ is diagonal, any change in each element of vector Ψ does not affect the other elements. In other words, the elements $\Psi_n = \mathbf{P}_n^{-1}\delta\Phi$, where $\mathbf{P}_n^{-1}$ is the $n-th$ row of the $\mathbf{P}^{-1}$ matrix, identify orthogonal directions in a transformed phase space, enabling to apply uncoupled, and hence well controllable, phase modifications to the system.

From a physical stand point, the TED method implies that all the actuators, that are thermally coupled, need to be simultaneously modified to apply the desired change (see Fig.3.1(b)). The weights are defined by the eigenmodes of the thermally coupled system, that is by the rows of the **P** matrix.

As expected and shown by simulations reported in this thesis, the best performance of the TED method is achieved when the phase coupling matrix **T** is precisely known. However, accurate information on thermal crosstalk is hardly available in practical cases. Noteworthy, our results show that the TED provides significant performance improvement with respect to individual tuning of thermal actuators, even when partial knowledge of the **T** matrix is available, for instance from empirical models, numerical thermal simulations, and experimental data. In Sec.3.2 we further comment this point and introduce practical techniques to evaluate **T** matrix.

Once phase mapping through TED is performed, any tuning and locking algorithm can be implemented by using the transformed coordinates $\mathbf{\Psi}$ as phase state variables of the system. Including feedback iterative approaches (like [61,62]), multi degree of freedom (DOF) stabilization methods [70], linear state-space control systems [71], dithering technique locking approaches [34, 72]. These concepts have been employed in the numerical and experimental examples reported in the following sections.

3.1.1 Numerical Simulation

To show the effectiveness of the TED method on generic photonic architectures, in this section we present the results of numerical simulations carried out on two different PICs, namely a coupled MRR filter and an MZI based switch fabric. Coupled MRR filters are widely used because

of their highly-selective frequency response, which also makes their performance very sensitive to fabrication tolerances, temperature drifts and laser wavelength fluctuations. MZI fabrics find applications for the realization of compact, broadband, high-port-count optical switches. In both cases, thermal actuation is one of the mostly used approach for active tuning and configuration, and thermal crosstalk effects must be counteracted to guarantee reliable control and high performance.

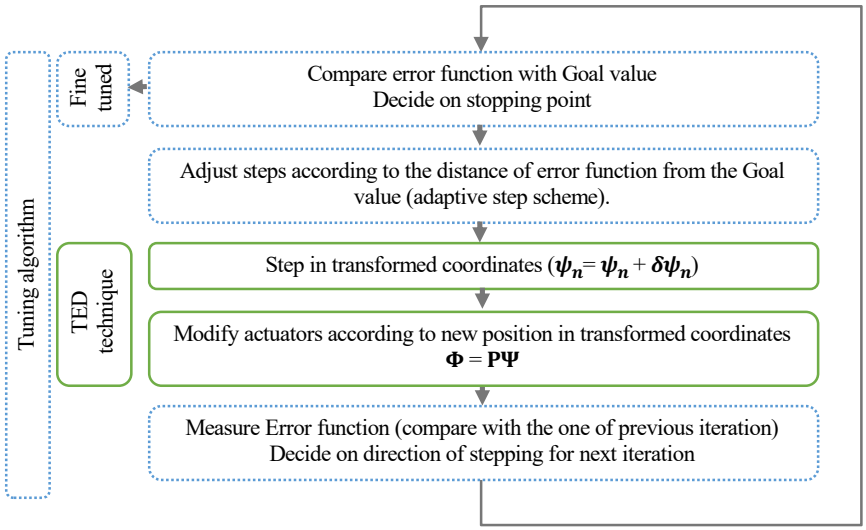

Figure 3.2: *(a) Block diagram of an example tuning algorithm using TED technique to modify actuators. At each iteration a step taken in transformed coordinate Ψ_n is translated to variation of actuators by $\Phi = \mathbf{P\Psi}$. Error function is evaluated and compared with the one of previous iteration to track the progress. If progress is not along the desired path, direction of movement is reversed simply by inverting the sign of $\delta\Psi_n$ .At the end of each cycle error function is compared with the goal to define the stopping point.*

Here we describe a simple closed-loop algorithm (which uses TED technique to modify the actuators) that can be applied to generic PIC architecture, as confirmed by numerical and experimental results reported in the following of this paper. Referring to the flow diagram of Fig.3.2, phase modifications $\delta\Psi_n$ are applied to match a target goal function, which can be for instance the minimization (or maximization) of the output optical power at certain optical ports. At each iteration, a step along $\mathbf{\Psi}_n$ is followed by calculating the corresponding phase vector $\mathbf{\Phi}$, providing the phase shift to be simultaneously given by each of the actuators which is obtained as $\mathbf{\Phi} = \mathbf{P\Psi}$. After each step $\delta\Psi_n$ is performed, the error function is evaluated. At this point, if progress is along the desired path (minimizing or maximizing the reading point value in this example), following steps

are repeated in the same direction, otherwise direction is reversed by inverting the sign of $\delta\Psi_n$. Once the PIC has reached the target configuration, the algorithm can be let to operate realizing a locking scheme, capable of maintaining the tuned condition in the event of unwanted perturbation, such as temperature fluctuations as well as drifts of the laser wavelength. Adaptive phase steps can also be used to find the best trade off between the converge speed of the tuning process and the residual oscillation introduced in system during the locking phase.

Optical power at a specific port is defined as the cost function for these analyses. This means algorithm is evaluated based on the convolution of modulated signal with transfer function of the filter. It allows the algorithm to push the filter matching the spectrum of the signal to obtain the best isolation (or negligible perturbation) for a specific channel. Other metrics like BER, eye diagram opening, amplitude of channels labels [40] or any other relevant parameter can be used as cost function depending on the application.

Coupled MRR filter

Figure 3.3(a) shows the schematic of a coupled MRR filter. A thermal actuator (in red) is integrated inside each resonator to modify the round-trip phase ϕ_i. Here we consider a 3rd order MRR architecture, but the proposed approach can be generalized to structures made of an arbitrary number of resonators. Conventional tuning methods for this kind of filters (hereinafter referred to as "individual tuning") exploit sequential sweeping of the individual resonance of each MRR for aligning it to the desired wavelength [60, 62]. However, we show that in the presence of thermal crosstalk, not only these approaches typically require a higher number of iterations, but they can also suffer from instability issues and may not even converge. In contrast, our results show that in all the considered cases convergence is always obtained when TED is applied.

For simplicity, we make the assumption that thermal cross-talk induces equal phase coupling μ between neighbor MRRs, while there is no phase coupling between the first and the third MRR. In this case, the phase coupling matrix is

$$\mathbf{T} = \begin{pmatrix} 1 & \mu & 0 \\ \mu & 1 & \mu \\ 0 & \mu & 1 \end{pmatrix} \tag{3.5}$$

whose eigenvectors

$$\mathbf{P}_1 = \begin{pmatrix} -1 \\ 0 \\ 1 \end{pmatrix}, \mathbf{P}_2 = \begin{pmatrix} 1 \\ \sqrt{2} \\ 1 \end{pmatrix}, \mathbf{P}_3 = \begin{pmatrix} 1 \\ -\sqrt{2} \\ 1 \end{pmatrix}, \tag{3.6}$$

are the columns of matrix $\mathbf{P}$. By inverting the $\mathbf{P}$ matrix, the orthogonal phase coordinates are calculated as given in Equ.3.4, that are

$$\begin{aligned} \delta\Psi_1 &= \mathbf{P}_1^{-1}\delta\Phi = \begin{pmatrix} -\frac{1}{2} & 0 & \frac{1}{2} \end{pmatrix} \delta\Phi, \\ \delta\Psi_2 &= \mathbf{P}_2^{-1}\delta\Phi = \begin{pmatrix} \frac{1}{4} & \frac{\sqrt{2}}{4} & \frac{1}{4} \end{pmatrix} \delta\Phi, \\ \delta\Psi_3 &= \mathbf{P}_3^{-1}\delta\Phi = \begin{pmatrix} \frac{1}{4} & -\frac{\sqrt{2}}{4} & \frac{1}{4} \end{pmatrix} \delta\Phi. \end{aligned} \tag{3.7}$$

at each iteration, a step is taken along these new coordinates and the related phase changes $\delta\Phi$ of each MRR are calculated as $\delta\Phi = \mathbf{P}\delta\Psi$.

As a case study, we consider a 3rd order MRR filter with a FSR of 50 GHz and bandwidth equal to 6.5 GHz. Random phase errors as large as $\pm\,\pi/4$ ($\pm$ 6.25 GHz) are intentionally introduced among the resonances of the MRRs, resulting in the 100 random initial configurations shown in Fig.3.3(b). At the Input port, an optical signal modulated according to a 5 Gbit/s On-Off Keying (OOK) intensity modulation is used. To model thermal crosstalk, a phase coupling coefficient μ= 0.15 is assumed between actuators. To point out the benefit of our approach, the filter was tuned by using the algorithm of Fig.3.2 to minimize the optical power at the Through port, using as phase variables the transformed coordinated $\mathbf{\Psi}$ by the TED method and the round-trip phases $\mathbf{\Phi}$ for the individual tuning method, respectively. In both cases, we assumed the same initial conditions of Fig. 3.3(b) for the perturbed filter and the same phase step-size of 0.015 rad.

Figure 3.3(c) shows the frequency domain response of the filter for all the considered cases after the implementation of TED-based algorithm. Convergence to almost overlapping spectra at the Through (blue curves) and Drop (red curves) is achieved regardless of the initial perturbed state of the filter. The convergence curves in Fig. 3.3(d), providing the optical power at the Through port, show that less than 50 iterations are required to tune filter to the desired state, where the isolation at the Through port is about 18 dB. In contrast, when individual tuning is used (see Fig. 3.3(e)), convergence is not guaranteed and, depending on the initial state of the filter, residual oscillations may appear that prevent the algorithm to bring the filter to the target state. In the considered example, 10% of trails did not

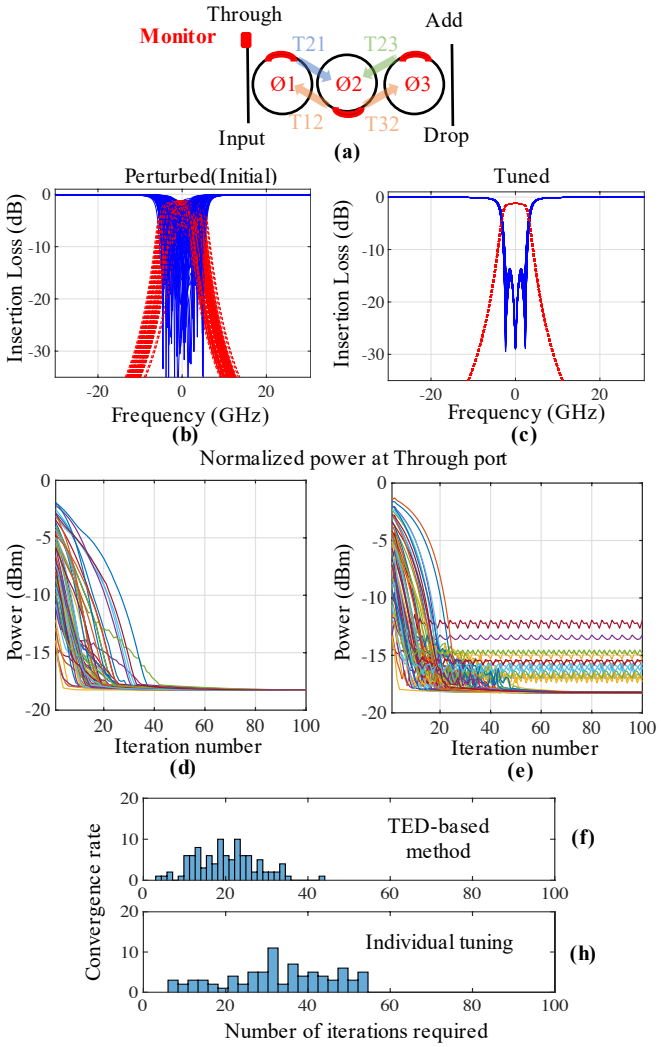

Figure 3.3: *Numerical simulations of the tuning of a 3rd order coupled MRR filter in the presence of thermal crosstalk (μ= 0.15). (a) Schematic of the filter presenting assumed phase coupling between resonators. (b) Spectral response in the initial state of the filter (100 configurations, up to ± π/4 random phase perturbations). (c) Through (blue-solid) and Drop (red-dashed) port transmission after the convergence of the TED-based tuning algorithm. Convergence curves showing the normalized power at Through port of the filter during (d) the TED-based tuning and (e) individual tuning of each MRR. Histogram showing the required number of iterations to reach the goal point using (f) the TED-based tuning or (h) individual tuning of each MRR for converged cases.*

converge to the maximum isolation. Restricting the analysis to the cases where convergence is achieved, the average number of required iterations in individual tuning is higher than the ones in the TED-based method. Histogram in Fig. 3.3(f) shows the required number of iterations to reach goal point using the TED-based tuning while Fig.3.3(h) presents results for individual tuning of each MRR. This increment in average and standard deviation indicates the dependence of convergence on the starting points because of thermal cross-talk.

MZI switch fabric

The second architecture that we considered is the 4x4 MZI arrangement depicted in Fig.3.4(a). It consists of four balanced 2x2 MZIs, each including a thermal actuator to control the switching state. To simplify the analytical description, let us assume that all the actuators introduce equal thermal cross-talk on surrounding MZIs, so that the phase coupling matrix is

$$\mathbf{T} = \begin{pmatrix} 1 & \mu & \mu & \mu \\ \mu & 1 & \mu & \mu \\ \mu & \mu & 1 & \mu \\ \mu & \mu & \mu & 1 \end{pmatrix}, \tag{3.8}$$

Assuming a phase coupling ratio μ= 0.18, the eigensolutions of the phase coupling matrix $\mathbf{T}$ are

$$\mathbf{P}_1 = [-0.44 \quad -0.44 \quad 0.76 \quad 0.13], \mathbf{P}_2 = [0.7 \quad -0.7 \quad 0 \quad 0],$$
$$\mathbf{P}_3 = [0.22 \quad 0.22 \quad 0.40 \quad -0.85], \mathbf{P}_4 = [0.5 \quad 0.5 \quad 0.5 \quad 0.5],$$

phase change along the orthogonal transformed coordinates can be calculated by $\delta\mathbf{\Psi} = \mathbf{P}^{-1}\delta\mathbf{\Phi}$.

To show a numerical example, let us consider the reconfiguration of the 4x4 switch fabric to route an input optical signal (5 Gbit/s OOK), provided at port In1, to output port Out3. This path requires MZI1 to be set to "cross" state and MZI4 to be set to "bar" state. Random phase errors as large as $\pm\pi/2$ are intentionally introduced in the unbalance of all the four MZIs of the PIC, leading to the 50 initial configurations shown in Fig.3.4(b), which show the frequency domain transmission from In1 to Out3 (blue curves) and the optical crosstalk due to the path from In2 to Out3 (red curves). As in the simulation example of MRR (Sec. 3.1.1), we assume the same initial conditions and phase step-size (0.05 rad) for both TED-based tuning and individual tuning while maximizing the optical power at port Out_3. Numerical results show that, by using the TED-based algorithm, the

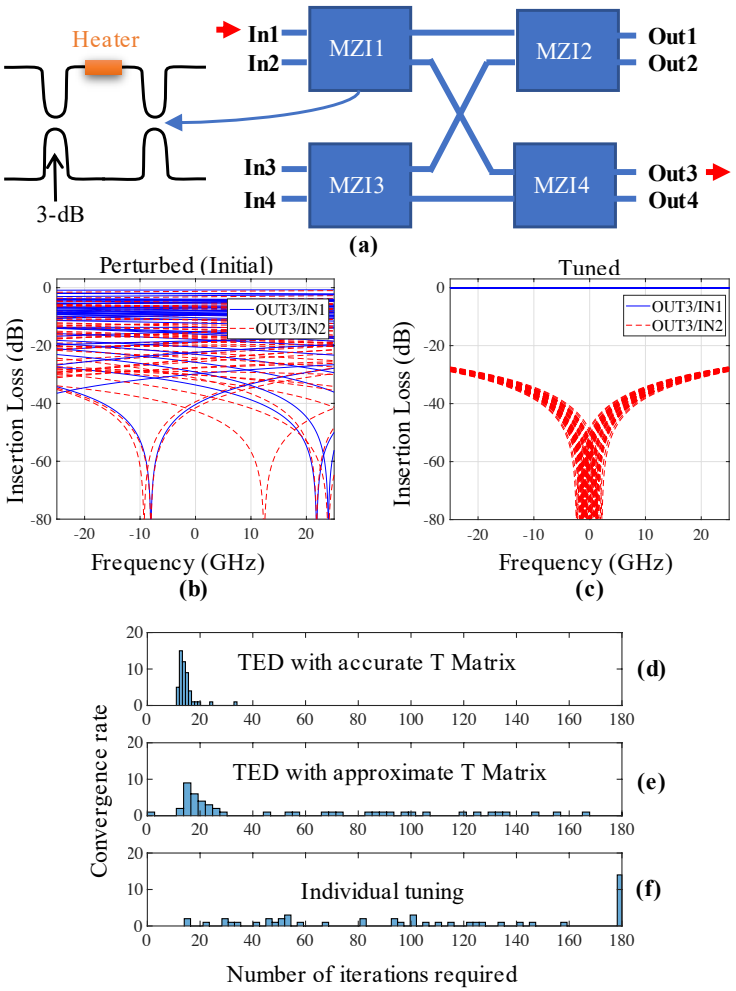

Figure 3.4: *Numerical simulation of the tuning of a 4x4 MZI switch fabric in the presence of thermal crosstalk (μ= 0.18). (a) Schematic of circuit. (b) Initial state of the switch (50 configurations, up to $\pm\,\pi/4$ random phase perturbations); (c) Frequency domain transmission Out3/In1 (blue-solid) and Out3/In2 (red-dashed) after the convergence of the TED-based tuning algorithm. Histogram showing the required number of iterations to set the routed path of the switch fabric by using (d) the TED-based tuning using accurate phase coupling matrix (T), (e) TED-based tuning using approximate phase coupling matrix and (f) individual tuning of each MZI.*

switch fabric can be effectively steered to the desired configuration (see Fig. 3.4(c)), achieving less than -25 dB optical crosstalk (red curves) for any initial conditions. It should be noted that convergence to almost identical transmission spectra is achieved even in cases where the initial switch

state routes the signal almost entirely to other output ports. Histograms in Fig. 3.4(d) show that on average the TED-based algorithm requires less than 20 iterations to achieve convergence. In addition, the small standard deviation indicates that the number of required iterations is almost independent of the initial state of the switch. In contrast, if the MZIs are individually actuated (see Fig. 3.4(f)), the average number of iterations increases significantly and distributes randomly. This exhibits dependence on the initial state due to existence of thermal cross-talk. These results confirm the benefits of the TED method to ease the configuration of PICs in the presence of thermal crosstalk.

To assess the performance of the TED-based algorithm when the **T** matrix is not accurately known, the method was applied by intentionally underestimating the mutual phase perturbation (which is μ= 0.18) by 40%, that is by considering μ= 0.072. While starting from the same initial points, non-efficient cancellation of thermal cross-talk is comprehensible by comparison between Figure 3.4(d) and (e). While comparing Figure 3.4(e) and (e) one can obviously assume that even TED-based method with non-accurate phase coupling matrix is presenting more efficient convergence rates comparing to individual tuning.

3.1.2 Experimental Results

The effectiveness of the TED-based method has been experimentally validated on a 3rd order coupled MRR filter. Figure 3.5(a) shows a top view microphotograph of the device, which was fabricated in a high-index-contrast SiON photonic platform. The 4.4% refractive index contrast enables the realization of MRRs with a FSR of up to 100 GHz with negligible bending loss. The SiON core channel waveguide has a square shape (2.2 X 2.2 μm) and is buried in a silica cladding. More details on the waveguide design and fabrication process can be found in [73]. The round trip phase of each MRR of the filter can be individually controlled by means of metallic heater deposited on top of the waveguide uppercladding. The optical power is measured via an external photodiode and transmitted to a Personal Computer (PC) by ADC on USB interface. The control algorithm is implemented via software (Matlab [74]) and the phase steps to be applied at each iteration (voltage change on each heater integrated in the PIC) are applied through a DAC on a USB interface.

In the following sections, the TED method is used to implement automatic tuning and wavelength locking of this device.

Automatic tuning

Phase perturbations were intentionally introduced in every MRR of the SiON filter by applying random errors in the voltages driving the heaters around their optimum tuning point. Figure 3.5(b) shows the measured Through and Drop port transmission of the perturbed filter when the induced frequency spread of the MRR resonances is as large as 100 pm (12.5 GHz versus 6.5 GHz BW of the filter). In line with the conditions considered in the numerical simulations of Sec. 3.1.1, at the input port of the filter a 5 Gbit/s OOK modulated signal (with carrier wavelength of 1565.470 nm) was used and the tuning algorithm was targeted to minimize the output power at the Through port. Assuming thermal crosstalk between the neighbor MRRs as the main contribution to the phase coupling (that is neglecting the phase coupling between the first and the third MRR), TED was implemented by using relations given in Sec. 3.1. In the experiments reported in this section, the temperature of the sample was kept constant at 25°C by using a TEC underneath the photonic sample. Figure 3.5(c) shows that, regardless of the initial perturbation, the filter was effectively tuned to the same shape, with a Through port isolation of 15 dB at convergence, corresponding to an estimated residual phase error of $\pi/50$.

The TED method was then compared to the individual tuning in terms of convergence ratio and speed. For a fair comparison, we assumed the same perturbed configurations of Fig. 3.5(b) as the initial state of the filter and we applied both schemes with the same phase step-size for the heaters. As predicted by numerical simulations reported in Fig. 3.3(e), in many cases sequential tuning of individual resonators did not converge to the target filter shape and a poor Through port isolation with deep oscillations in the steady state was obtained. In contrast, the TED-based tuning did converge for all the considered initial cases in less than 40 iterations (see Fig. 3.5(e)). Since the TED method can be applied to generic algorithms, we also implemented an adaptive phase step-size technique to increase the convergence speed, while keeping the steady-state error unaffected. As an example, results in Fig. 3.5(f) show that convergence is accelerated by at least a factor 2 adapting the phase step-size of the heater according to the distance from the target point. A step size selection strategy that adaptively reduces the step size while progressing towards the target point allows for a faster convergence while reduces the perturbations and steady state error.

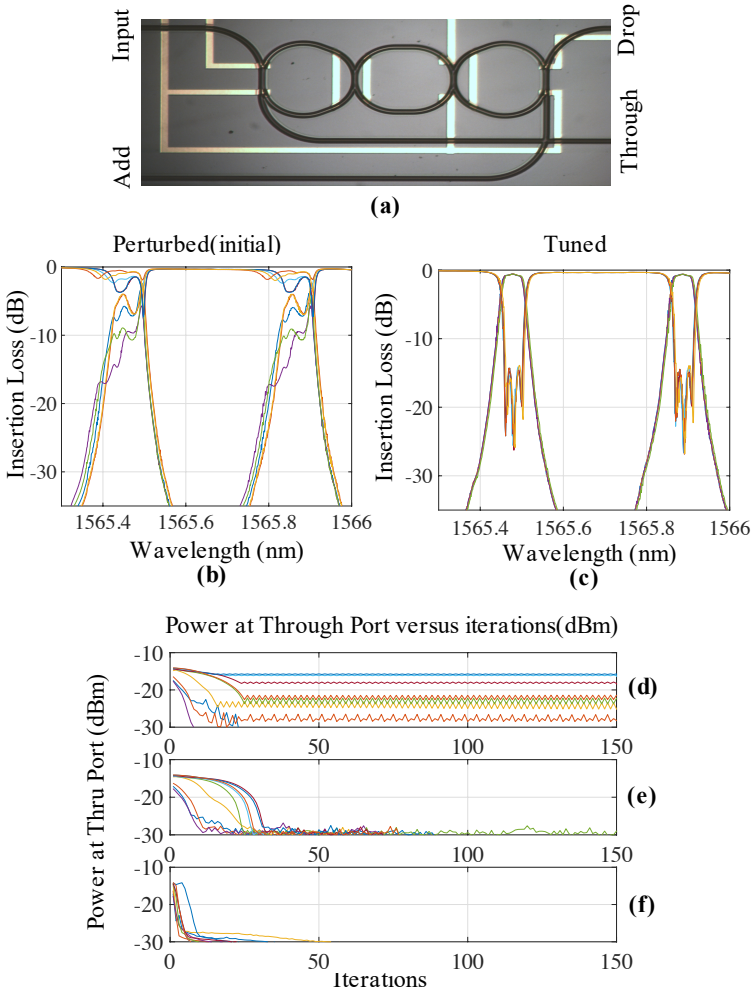

Figure 3.5: *Experimental validation of automatic tuning based on TED method. (a) Top view photograph of a 3rd order coupled MRR filter fabricated in SiON technology. Measured transmission of the Through and Drop port of the filter (b) for five randomly perturbed configuration (+/- 100 pm) induced by using thermal phase shifters and (c) after automated tuning performed by using TED method. Convergence curves showing the measured optical power at Through port of the filter during the implementation of the following automatic tuning schemes: (d) individual tuning of MRRs, (e) TED-based tuning with fixed phase step and (f) TED-based tuning with adaptive phase step.*

Wavelength Locking

We also investigated the possibility to exploit the TED-method with a wavelength locking algorithm to maintain the fine-tuned status of the fil-

ter (achieved though the automatic tuning procedure, see Fig. 3.5(c)) versus time varying perturbations of the system. These perturbations could be temperature fluctuations of the entire photonic chip as well as wavelength drifts of the input signal.

In a first experiment, we demonstrate that TED-based tuning can efficiently work even though the temperature of the whole photonic sample is not stabilized. To this aim, we intentionally introduced a controlled temperature shift (linearly decreasing by 3°C) by acting on the TEC underneath the sample, resulting in a wavelength shift of the transfer function of the filter by about 35 pm (about 70% of the filter bandwidth). Figure 3.6(a) shows the evolution of heater voltages and Through port power during the automatic tuning of the filter, starting from a random initial condition of the MRR filter. From the comparison with the result of Fig. 3.5(f), where the temperature of the sample was kept constant by the TEC, we can conclude that: (i) temperature fluctuations do not significantly increase the number of iterations required to achieve convergence; (ii) once convergence to the target state of the filter is achieved (after about 10 iterations) the TED-method can be used to compensate against temperature fluctuations of the photonic sample (note that the voltages of the heaters increase, while the Through port power is almost unchanged). Depending on the control algorithm adopted for the locking scheme, different values of wavelength drifts can be compensated. In the considered example of Fig. 3.6(b), we assumed a sudden drift in the wavelength of the input signal, as large as 30 pm (equivalent to 3.75 GHz, that is about 60% of the filter bandwidth) which can be the result of using a look up table. This perturbation, which is responsible for the sharp increase (about 15 dB) of the measured power at Through port, is completely recovered in less than 10 iterations. Finally, we performed eye-diagram measurements to evaluate the performance of the TED-based schemes on the quality of transmitted signals. Figure 3.6(c) shows the reference eye diagram of the 5 Gbit/s OOK signal transmitted at the Drop port of the filter when the transfer function is tuned as in Fig. 3.5(c) and the carrier wavelength of the signal (1565.470 nm) is aligned with the center of the filter passband. When the signal carrier wavelength is shifted by 10 pm (20% of the filter bandwidth) and no wavelength locking scheme is employed, the eye diagram is distorted as shown in Fig. 3.6(d). In contrast, if the wavelength shift is applied when the wavelength locking algorithm is active (see Fig. 3.6(e)), no significant deterioration of the eye diagram is observed with respect to the reference signal.

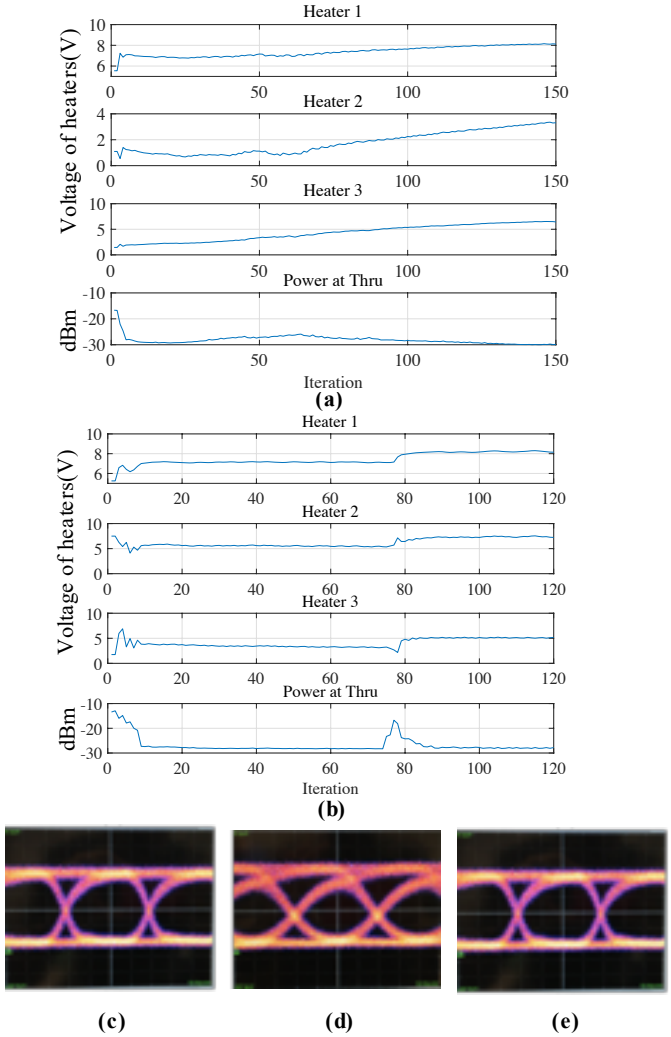

Figure 3.6: *Experimental validation of wavelength locking schemes based on TED method. Panels (a) and (b) show the voltages of heaters and the optical power measured at Through port of the filter when (a) automatic tuning and wavelength locking is performed while the temperature of the chip is changing by 3°C (35 pm shift) and (b) a sudden 30 pm change in the wavelength of the input signal is introduced after iteration 75. (c) Reference eye diagram of the 5 Gbit/s OOK signal at the Drop port of the tuned filter. Panels (d) and (e) show the eye diagram after the introduction of 10 pm shift of the channel wavelength when the wavelength locking algorithm is (d) off and (e) on.*

3.2 Thermal crosstalk evaluation

A key point of the TED method is the knowledge of the **T** matrix. In principle it could be inferred from thermal simulations. However, this approach is hardly practical for large scale PICs accounting for many heat sources, especially because the overall assembly of the PIC should be considered, including on-chip metal lines, wire bonding, chip submount and ultimately the package itself. Therefore, for an accurate estimation of the **T** matrix, alternative strategies should be adopted, which should be preferably applicable to arbitrary PIC architectures.

In the following, we consider three different solutions to evaluate the thermal crosstalk with different accuracy:

1. Heuristic (lowest accuracy): an estimation of thermal cross talk is inferred by simply considering the topology of the circuit;
2. Optical measurement (highest accuracy, not always practicable): thermal crosstalk is directly estimated by measuring the unwanted wavelength shift of neighbor devices;
3. Electrical measurement (good accuracy, always practicable): thermal crosstalk is indirectly estimated by measuring the change of the electric resistance of neighbor heaters used as temperature probes;

It is worth to mention that **T** depends only on the device architecture and not on the specific operation and, as any transfer function, must be evaluated once, independently on the circuit working point.

We try to evaluate the thermal crosstalk **T** matrix and its impact on the effectiveness of TED based technique is investigated. The analysis is performed on the MRR based cross-bar router presented in Fig.3.7. Starting with heuristic approach, we assume that all the actuators to introduce equal thermal crosstalk on surrounding MRRs. The corresponding phase coupling matrix **T** is hence

$$\mathbf{T} = \begin{pmatrix} 1 & \mu & \mu & \mu \\ \mu & 1 & \mu & \mu \\ \mu & \mu & 1 & \mu \\ \mu & \mu & \mu & 1 \end{pmatrix} \tag{3.9}$$

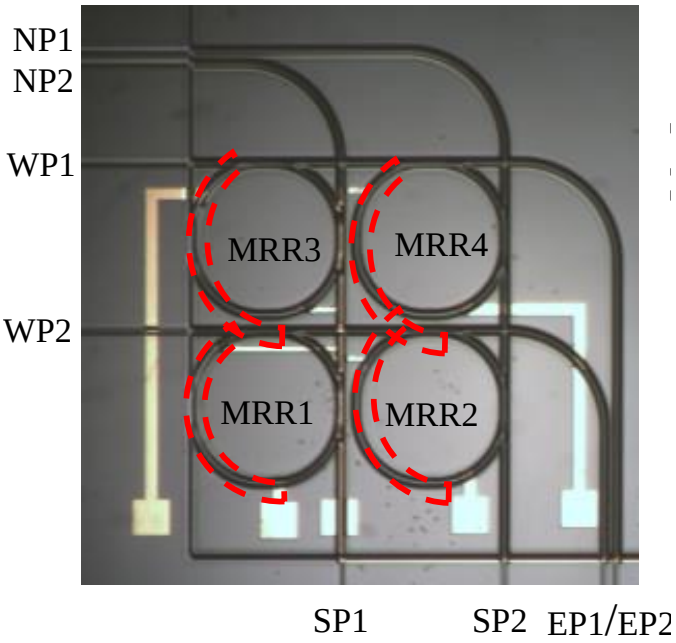

Figure 3.7: *Top view photograph of a 2x2 MRR cross-bar interconnect fabricated in SiON technology. The red dashed lines indicate the position of the heaters integrated on the MRRs.*

where $\mu = 0.1$ is a good estimation, done experimentally of the average thermal crosstalk. Each column of the $\mathbf{P}$ matrix is an eigenvector of the matrix $\mathbf{T}$ in Equ.3.9. The matrices $\mathbf{P}^{-1}$ and $\mathbf{T}_D$ are reported in the end of this section (3.2). The phase change along the orthogonal transformed coordinates can be calculated as $\delta\mathbf{\Psi} = \mathbf{P}^{-1}\delta\Phi$. Using these orthogonal vectors, uncoupled modifications can be applied by tuning algorithm (Fig.3.2).

To provide a metric for evaluating the effectiveness of thermal crosstalk compensation, Fig.3.8(a) shows the convergence curve of the TED-based gradient descent algorithm, that is the optical power at the output port SP2 versus the number of iterations. Assuming a heuristic $\mathbf{T}$ matrix, the average number of iterations that are required to set the optical path is about 40, as shown by the green-dashed curve in Fig.3.8(a). As a benchmark (black diamonds), we consider the case where TED is not used, that is the MRRs are individually controlled by applying phase shifts $\delta\mathbf{\Phi}$. Because of thermal crosstalk, we observe an extremely slow convergence and, depending on the initial perturbed state of the PIC, the algorithm may even not converge to the target response.

Faster convergence is achieved when the off-diagonal (crosstalk) terms of the phase coupling matrix **T** are closer to the actual values. An exact evaluation is achievable in the considered PIC because the coefficients of the **T** matrix can be directly estimated through optical measurements. In fact, since all the output ports of all the MRRs are accessible, we measured the cross-induced shift of each MRRs resonances when the different heaters are sequentially switched on. Figure 3.8(b) shows the optically-measured off-diagonal terms of the phase coupling matrix **T**. More specifically each pillar provides the induced crosstalk by each heater on the surrounding MRRs as the wavelength shift of that MRR to the source MRR (heater) wavelength shift (normalized to the maximum crosstalk). It should be noted that not only the off-diagonal terms are not equal [this being rather expected and in contrast with the heuristic assumption made in Equ.3.9], but they are also not symmetric. This asymmetry is justified by considering that the heaters are not as long as the MRR circumference, but they only cover a portion of each MRR (see Fig. 3.7). As a result, the distance of heater1 (integrated in MRR1) from the waveguide of MRR2 is larger than the distance of heater2 (integrated on MRR2) from the waveguide of MRR1. As shown by the solid blue line in Fig.3.8(a), by using the optically measured value of the thermal crosstalk the **T** matrix, the average number of iterations that are required to set the optical path is about 25, thus proving faster convergence.

However, a direct optical measurement of thermal crosstalk is not possible in most cases, because it requires the possibility to optically access the output ports of each tunable element. A good estimation of the **T** matrix can be achieved electrically, by measuring the temperature-induced change of the resistance of metallic probes located in suitable spots of the PICs. To this aim, we can advantageously use the heater structures themselves, which can be used also as temperature sensors to map thermal crosstalk across the photonic chip. Fig. 3.8(c) shows the electrically-estimated off-diagonal terms of the phase coupling matrix **T**. In this case, each pillar provides the resistance change of each heater to the resistance change of the perturbing heater (normalized to the maximum crosstalk). In the considered case the heaters are realized as a thin layer of Nickel-Chromium with a nominal resistance of 562Ω and a temperature dependence of α = 0.00034 1/°C in ΔR/R= α*ΔT. We use lock-in detection scheme with resolution of 30 ppm which for our heaters meant variation of 17 $m\Omega$. With this setup we can measure 0.1 degree of change in our sensors. It should be noted that the electrically measured T matrix differs from the

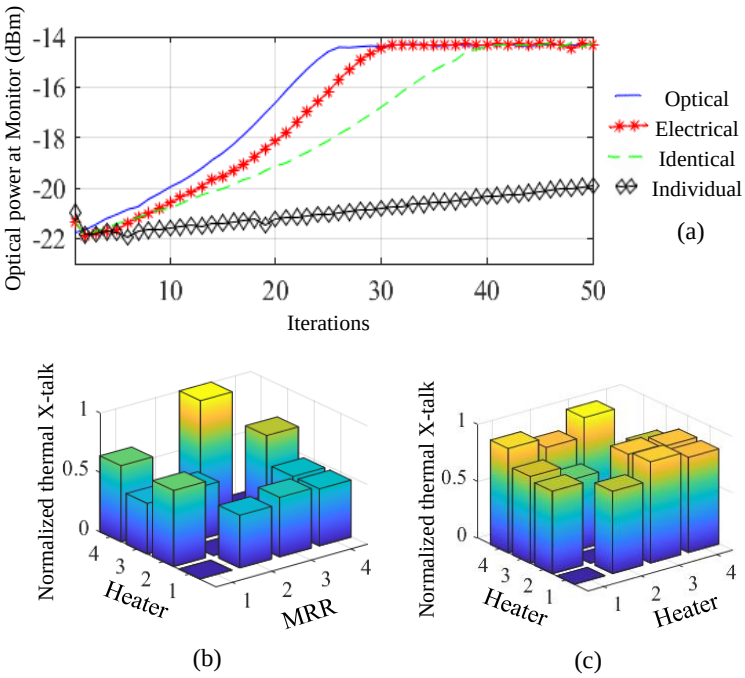

Figure 3.8: *(a) Convergence rate of TED-based tuning of the 2x2 MRR cross-bar interconnect of Fig. 2a when the off-diagonal terms of the phase coupling matrix T are assumed to be identical (green dashed), when they are estimated from electrical measurements (red asterisks), from optical measurements (blue solid). Black diamonds show the converge rate when MRRs are individually tuned (no-TED). (b) Optically and (c) electrically measured off-diagonal terms of the phase coupling matrix T normalized to the maximum value.*

optically estimated one of Fig. 3.8(b). This difference can be justified by considering that the electrically measured **T** matrix provides the thermal crosstalk at specific points where probe heaters are placed (heater-to-heater), while the optically measured **T** matrix provides the exact value of thermal crosstalk integrated over the optical ring path (heater-to-ring). As shown by the red asterisks in Fig.3.8(a), by using the electrically-estimated **T** matrix in the TED method, convergence is achieved with a number of iterations comprised between the optimum (optically-estimated **T** matrix) and the heuristic **T** matrix. As a main advantage, an electrical measurement of thermal crosstalk can be performed in arbitrary PIC architectures, by using already existing metal structures (e.g. heaters) and/or by adding metal probes in specific points of the PIC to get a detailed mapping of the

temperature gradient across the photonic chip.

Eigenvectors of thermally coupled system

As supplementary information, in this section we provide the numerical values of the phase coupling matrix **T** of the 2x2 MRR cross-bar interconnect of Fig. 3.7, as evaluated with the three different approaches presented in previouce section (Sec. 3.2). To better highlight the mutual crosstalk level, we focus on the relative values of the off-diagonal terms of the **T** matrix, which are collected in a modified matrix $\mathbf{T}_{mm}$, which is achieved by zeroing the main diagonal of the **T** matrix and normalizing to the maximum off-diagonal term. The elements of the optically and electrically measured $\mathbf{T}_m$ matrix are indeed shown in Fig. 3.8(b)-(c). Further, we also provide here the numerical values of the eigenvectors matrix **P** (associated with the optically measured, electrically measured and heuristic **T** matrix), which were used in the experiment of Fig. 3.8(a) to define new coordinates $\delta\mathbf{\Psi} = \mathbf{P}^{-1}\delta\mathbf{\Phi}$. From the optical measurement of the mutually induced wavelength shift of the MRR resonances, we obtain

$$\mathbf{T}_{Opt} = \begin{pmatrix} 0 & 0.64 & 0.42 & 0.64 \\ 0.44 & 0 & 0.44 & 0.2 \\ 0.5 & 0.25 & 0 & 1 \\ 0.48 & 0.48 & 0.72 & 0 \end{pmatrix} \tag{3.10}$$

whose off-diagonal elements [see Fig.3.8(b)] are normalized to the max value of 0.173, and its eigen vectors are calculated as

$$\mathbf{P}_{Opt} = \begin{pmatrix} 0.46 & 0.28 & -0.36 & -0.12 \\ 0.44 & 0.74 & 0.61 & 0.39 \\ 0.51 & -0.23 & 0.44 & 0.54 \\ 0.57 & -0.55 & -0.54 & -0.73 \end{pmatrix}. \tag{3.11}$$

By electrically measuring the variation of heater resistance induced by mutual thermal crosstalk, we obtain

$$\mathbf{T}_{Elec} = \begin{pmatrix} 0 & 0.72 & 0.76 & 0.9 \\ 0.72 & 0 & 0.63 & 0.83 \\ 0.88 & 0.86 & 0 & 1 \\ 0.83 & 0.83 & 0.74 & 0 \end{pmatrix} \tag{3.12}$$

whose off-diagonal elements [see Fig.3.8(c)] are normalized to the max value of 0.01, and relavant eigen vectors are

$$\mathbf{P}_{Elec} = \begin{pmatrix} 0.5 & 0.22 & -0.54 & -0.32 \\ 0.49 & -0.85 & -0.3 & -0.38 \\ 0.45 & 0.47 & 0.78 & -0.16 \\ 0.54 & 0.04 & -0.04 & 0.85 \end{pmatrix}. \tag{3.13}$$

In the heuristic approximation of the **T** matrix we considered off-diagonal elements equal to $\mu = 0.1$, which is close to the average value of the off-diagonal terms of the optically measured **T** matrix, we get

$$\mathbf{P}_{heur} = \begin{pmatrix} 0.05 & 0.83 & -0.21 & 0.5 \\ 0.75 & -0.25 & 0.34 & 0.5 \\ -0.64 & -0.11 & 0.57 & 0.5 \\ -0.14 & -0.46 & -0.71 & 0.5 \end{pmatrix}. \tag{3.14}$$

These matrices are different from each other and exhibits different level of **T** matrix estimation. In Sec.3.2 and more specifically Fig.3.8(a) we evaluated the performance of TED-based control utilizing these matrices to compare the results.

3.3 Summary

In this chapter, we theoretically introduced and experimentally demonstrated a technique capable of canceling the phase coupling due to thermal cross-talk in photonic integrated circuits [75]. Instead of individually controlling actuators separately, in the TED technique all the actuators are controlled simultaneously according to appropriate weights, which are based on eigensolution of the thermally coupled system. Mathematically this implies a deterministic coordinate transformation, which can be applied to any kind of tuning and locking algorithm, based for instance on look-up tables [76], gradient-based [77, 78] and dithering-based techniques [34, 72], as well as multi degree of freedom (DOF) stabilization methods [70]. The use of the TED technique is not limited to specific circuit topologies but can be extended to generic PIC architectures. Through numerical simulations we proved its effectiveness in coupled MRR filters and in MZI switch fabrics. While in the individual control of phase actuators the thermal crosstalk can inhibits convergence, adopting the TED method convergence is always achieved in our simulations and experiments. Furthermore, the TED-based method allows to reduce the average number of required iterations while this number is also less sensitive to the

initial perturbed state of the PIC. Even though complete thermal crosstalk cancelation would require precise knowledge of phase coupling matrix **T**, we also demonstrated that the benefits of the TED method are mostly preserved when **T** is only partially known. This matrix can be approximated heuristically or obtained by thermal simulations, optical measurements or using data from implemented temperature sensors on the chip. Experimental results performed on MRR-based filters confirm the faster and more robust convergence of the TED-based tuning and locking algorithms, with respect to conventional approaches, to counteract temperature drifts or to track random fluctuations of the wavelength of the input signal. Regarding the scalability of the proposed method, the complexity of any TED-based control algorithm scales linearly with the number of thermally coupled phase actuators. In contrast, if thermal crosstalk is not mitigated (e.g. techniques where heaters are individually controlled), complexity is expected to grow more than linearly, since additional steps are required to compensate for thermal cross-talk effects. Finally, it should be noted that, although the TED method has been introduced here to cope with the specific problem of thermal crosstalk, its validity can be extended to other crosstalk effects, such as mechanical stress coupling in piezo actuators and Radio Frequency (RF) coupling in transmission lines for instance in high-speed integrated optical modulators.

CHAPTER 4

Techniques and recipes

A significant challenge for complex PICs comes from the realization of a robust control algorithm maintaining the optimum response of the function while allowing for reconfiguration and adaptation to new requirements. These algorithms are required to update the actuators of the photonic functions to tailor their response to maintain an specific functionality like rejection of a signal, transparent add/droping a channels from WDM grid or presenting suitable filtering performance. During operation, the characteristic of the signal in terms of its modulation scheme or central wavelength can change and the control algorithm is required to automatically update the PIC for these changes. The control algorithm should identify the desired channel placed between WDM grid in presence of the other channels and act on it without introducing perturbation on the grid. Automatic control algorithm can save time and resources in characterization phase of PICs offering a robust calibration compensating for fabrication tolerances and providing reliable and dynamic LUT to maintain the optimum operation point of PICs [79] [80]. In this chapter we discuss some techniques and trick which can be adopted both in the design and application phase of the PIC help solving some of these problems. We examine them on various PICs to evaluate the performance improve-

ments. In next two chapters (Chp.5 and Chp.6) we adopt these approaches to design and control two complex PICs and demonstrate interesting applications.

4.1 Removing ambiguities in control merit function

PICs being tuned to a specific channel in presence of WDM grid should act on that specific channel only. Since intensity of the light (via PD or CLIPP) is being used as the merit in control algorithms, possibility of distinguishing the channels apart is a necessity. This should allow the control system to act on the desired channel without perturbing the others. A piece of overhead information associated with the optical channel or data packet , known as an "optical label", can help overcoming this ambiguity. For this aim, to measure channel powers independently of either multiple optical signals or optical noise propagating simultaneously in a waveguide, one can make use of channel labeling strategies. One way of providing an optical label to a signal is to intensity modulate the optical channel on the transmitter side with a frequency f_q. To not degrade the performance of the transmitted channel, a low modulation index μ (< 8%) can be used [40]. This can be achieved with a MZ modulator driven with an amplitude much smaller than its V_π or with a bias signal on the laser itself. The signal labeling can be performed either directly on-chip, by using thermally tuned MZ modulators [33] or with external modulators close to the transmitter. In sec 4.1.1 we further discuss this concept.

PICs that work based on interferometry have periodic frequency response known as FSR. This means we can almost observe the same frequency features if the device is shifted an FSR away. To prevent reaching other FSRs of the optical function in control algorithms we can set limits in range of voltages/currents applied to the actuators. Another useful technique is to understand direction of deviation in the PIC frequency response from its optimum point and apply the appropriate actuation to compensate for it. Ambiguity rise using optical power as merit in control algorithm since it only gives us information of the deviation value not the direction. Considering the frequency response of MZI if the device is deviated from its optimum point (max or minimum of transmission), channel dropped into the Cross port only lose its optical intensity which is not informative enough to understand if this deviation is in red or blue direction. Symmetrical response of this device is the source of this ambiguity. In Sec. 4.1.2 we discuss slope tracking approach to resolve this problem known as "dithering technique".

4.1.1 Signal labeling

The best practice to identify channels from each other in DWDM grid is the labeling of the signals to be processed with weak pilot tones [33]. One way of providing an optical label to a signal is to intensity modulate the optical channel on the transmitter side with a frequency f_q. To avoid degrading the performance of transmitted channel, a low modulation index μ (< 8%) can be used [40]. This can be achieved with a MZ modulator driven with an amplitude much smaller than its V_π or with a bias signal on the laser itself. The signal labeling can be performed either directly on-chip, by using thermally tuned MZ modulators [80] or with external modulators close to the transmitter. To obtain the label power measurement one needs to add a label demodulation stage. This can be done anywhere in the optical network and can be performed with a simple 1% optical tap or inline via transparent detectors (CLIPP). Following the detection by the photodiode and amplification by the TIA the signal can be digitized and processed in a digital signal processor or even directly used in understand the presence of the channel.

As an example, if two channels (Ch1 and Ch2) are labeled by modulations with frequencies f_i and f_e respectively, at the detector they can be distinguished by lock-in demodulation of the corresponding frequency without affecting the quality of the signal [40]. The key advantage of the labeling method is its simplicity and low cost of associated hardware. An illustrative schematic of this strategy is shown in Fig. 4.1.

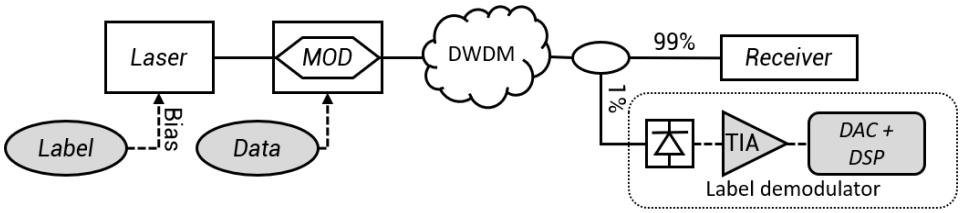

Figure 4.1: *Schematic diagram depicting the channel labeling strategy.*

As a case analysis, we consider a 2x2 cross-bar interconnect of MRR. This device is used to route the inputs signals, either a single channel or a comb of WDM channels. Figure 4.2(a) shows a top view microphotograph of the device, which was fabricated in a high-index-contrast SiON photonic platform [73]. The SiON channel waveguide (2.2 μm x 2.2 μm) has a refractive index contrast of 4.4% and the MRR resonators have a free spectral range of 50 GHz. The round-trip phase of each MRR of the filter

can be individually controlled by means of metallic heater deposited on top of the waveguide uppercladding. Phase perturbations were intentionally introduced in every MRR of the PIC by applying random errors in the voltages driving the heaters around their optimum tuning point simulating the circuit variability. The measured transmission from WP2 port to SP2 port of the filter is shown in Fig.4.2(b).

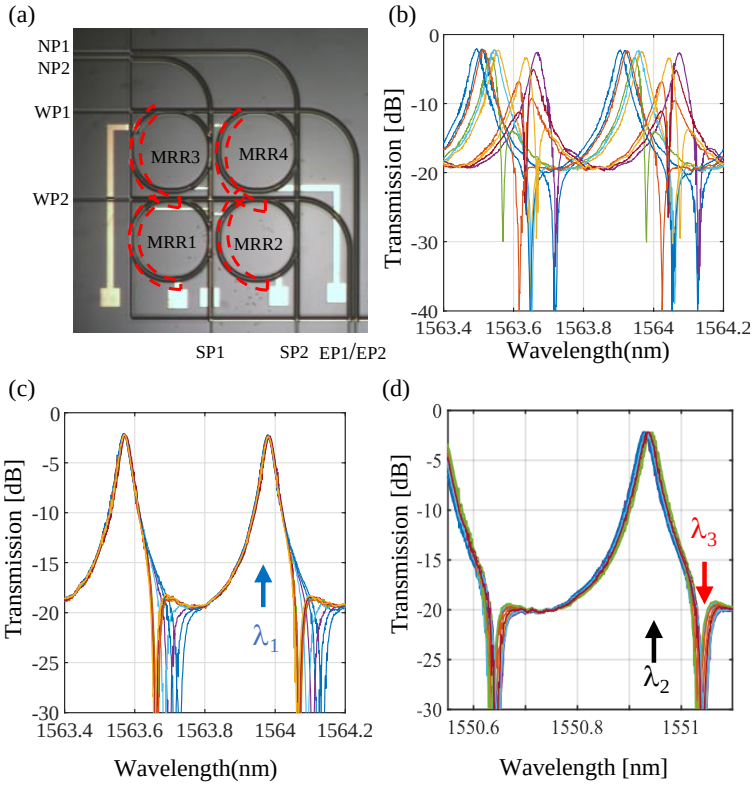

Figure 4.2: *Top view photograph of a 2x2 MRR cross-bar interconnect fabricated in SiON technology. The red dashed lines indicate the position of the heaters integrated on the MRRs. Measured transmission from WP2 port to SP2 port (b) for 10 randomly perturbed configurations induced by using thermal phase shifters, and after automated tuning (c) to a signal at λ_1 = 1563.98 nm, and (d) to signals at λ_2 = 1550.93 and λ_3 = 1551.03 nm.*

A TED-based gradient descent algorithm employing the transformed coordinates $\delta\Psi$ was used to automatically configure the circuit in order to set an optical path from input WP2 to output SP2 at a single CW signal at wavelength $\lambda 1$ = 1563.98 nm. Results in Fig.4.2(c) show that regardless of

the initial perturbation, the filter was effectively tuned to maximum transmission at the desired wavelength, which is achieved by correctly setting the resonant frequency of MRR2. It should be noted that the final transfer functions of the circuit overlaps only around the target wavelength λ_1, and periodically every FSR, but are not exactly the same. This effect is expected to happen at wavelengths where no cost function is defined and, depending on the degrees of freedom of the system, the frequency response of the PIC may converge to random solutions (in this specific case the variability of the frequency response is related to the unconstrained position of the resonance of MRR1 that generates a notch adjacent to MRR2 resonance). To manage this problem, the same algorithm was then used to route two channels, namely λ_2 = 1550.93 nm and λ_3 = 1551.03 nm, which were simultaneously injected at input port WP2, to output ports SP2 and SP1, respectively. To this aim, the two signals were labeled each via a shallow modulation tone, with a modulation depth of <8 % and a frequency f_1 = 11 kHz and f_2 = 17 kHz. The tuning algorithm was targeted to maximize the ratio between the amplitude of tones at the port SP2, that is to maximize the isolation between the two signals. Figure 4.2(d) shows that the frequency responses of the MRR router, which is constrained both at the peak of the transmission curve (λ_2) and at the notch (λ_3), nicely overlap across the entire wavelength range.

4.1.2 Dithering

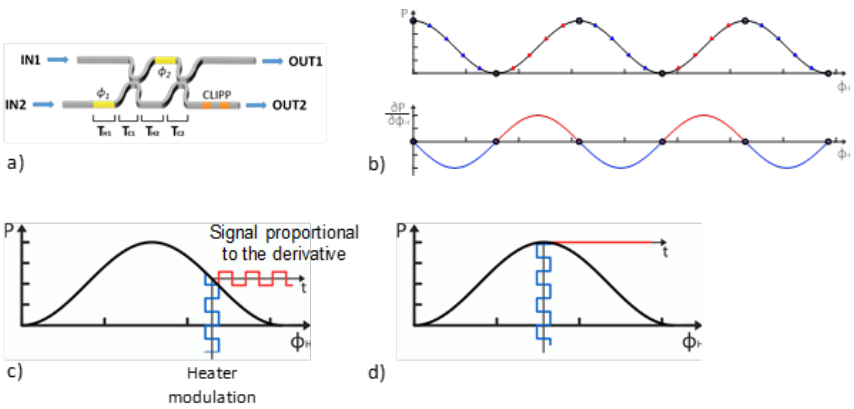

Figure 4.3: *Working principle of the dithering technique for a single Mach-Zehnder Interferometer. a) MZI structure with two phase shifters (ϕ_1 and ϕ_2) and a single CLIPP sensor; b) output optical power as a function of the phase and its first derivative; c) and d) show the MZI response to a dithering signal at different working points.*

The dithering technique is a powerful strategy to maximize (or minimize) the output of an interferometer. Fig.4.3 shows the working principle in the case of a single MZI.

A phase shifter (e.g. a heater) is modulated using a small-amplitude signal (sinusoidal or square wave) producing a small oscillation of the output optical power proportional to the derivative of the MZI response. The control system changes the working point of the phase shifter in order to set to zero the amplitude of the output oscillation that corresponds to a condition of zero derivative, i.e. a maximum or minimum point. The dithering technique has several advantages from the practical point of view:

(i) The control system operates to set to zero the output modulation irrespective of the total optical power and of the sensitivity and offset of the sensor, thus no specific calibrations are required;

(ii) The controller can be based on a simple integral action, easily implemented using an analog circuit or a low-complexity digital system;

(iii) The sign of the control law defines the stable equilibrium condition, i.e. if a maximum or a minimum is reached;

(iv) A single sensor can be used to control multiple heaters by using orthogonal modulating signals;

The latter point is particularly important in view of a reduction of the number of sensors in large MZI meshes. As an example, Fig. 4.4 shows a full control of a MZI using a single sensor and jointly driving both heaters.

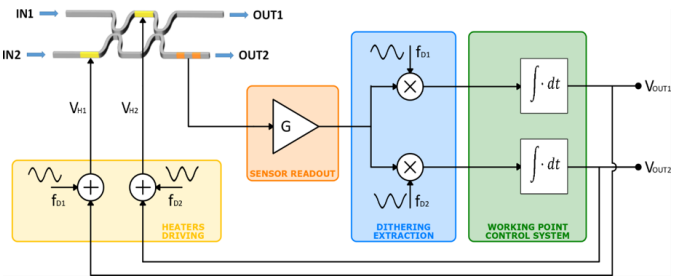

Figure 4.4: *Integral control of a MZI using a single sensor and two orthogonal dithering signals.*

A dithering signal is added at each heater. By choosing two orthogonal signals, as sinusoidal waves at different frequency or in quadrature, it is possible to simultaneously extract the partial derivatives of the MZI

response using two synchronous demodulators (and a proper low pass filter to remove the high frequency components) operating in parallel on the output of the sensor readout circuit. The output of the demodulators is integrated and fed back to the heaters for setting their working point. Each integral controller independently achieves a condition of equilibrium characterized by a demodulated signal at zero mean value, jointly defining a relative maximum (or minimum) of the output optical power.

4.2 Tuning to signal spectrum

Traditionally, PIC tuning is implemented targeting a specific frequency response. This approach can be valuable for testing, and pre-calibration procedures, but it is not practical for automated tuning of the PIC during its operation because it is resource and time consuming. For instance, it may require a tunable source and/or a spectrum analyzer to monitor the response at wavelengths of interest. Likewise, time domain approaches, based on the measurement of the BER or eye diagram distortion, require considerable load of DSP as well as electrical power consumption. In any case both approaches are hardly practical when the device is in use.
Here we discuss the automated tuning of the PIC response according to the PSD of the optical signal provided at the input. Basically, we define a simple cost function, which could essentially be the maximization (minimization) of the signal power transmitted though the PIC, from a specific input port to a specific output port. This power can be simply measured either at an end port of a device or through the integrated monitors (tap detectors [81] or transparent detectors CLIPP [40]). If multiple signals (channels) coexist in the same optical waveguide of the chip, labeling strategies (tones) can be used to discriminate the power of a given channel regardless from the presence of other channels [33] (further explained in Sec.4.1.1). We can anticipate that, since the filter is tuned looking at a specific channel, by changing the central wavelength, the bandwidth or the modulation format of the channel, that is its PSD, the PIC frequency response will be automatically tailored to optimize the filter metric on that channel. Therefore, even though the circuit architecture is not supposed to have a pronounced reconfigurability (e.g. bandwidth tunability), some frequency reshaping effect will be dictated depending on the input signal.

4.2.1 Adaptive tuning of re-configurable filters

The automatic adaptation of the filter shape to the PSD of the input signal is a general concept that can be exploited in arbitrary PICs, especially in the ones with a reconfigurable frequency response. As an example, let us consider the PIC of Fig.4.5(a), consisting of unbalanced MZI loaded with two MRR all-pass filters. This architecture implements a tunable bandwidth filter, since the bandwidth can be controlled by tuning the relative positions of the MRR resonances and the phase unbalance between the two arms of the MZI [82]. The MZI has 3 dB couplers, while the power coupling between the MRRs and the bus waveguide is 0.66. With these parameters the bandwidth of the filter, whose FSR is 25 GHz, can be tuned from 0.25*FSR (7 GHz) to 0.7*FSR (17 GHz).

Different initial perturbations were intentionally introduced as random errors in the voltages driving the three heaters (2 MRRs and MZI) around their optimum tuning point. Figure4.5(b) shows the frequency response of bar and cross port of perturbed filters when up to 20% phase errors are introduces. The PIC was automatically tuned by using a TED-based gradient-descent tuning algorithm to minimize the optical power at cross port of filter. As input signal we used a channel with 10 Gbit/s OOK modulation at the wavelength of 1563.87 nm. Since in this device a direct optical measurement of the phase coupling matrix **T** is not possible, due to the lack of accessible monitor ports at the output of each tunable device, we performed electrical measurement of thermal crosstalk, as shown in Sec. 3.2.

The frequency response of the tuned filters at convergence is shown in Fig.4.5(c) for cross port (red lines) and bar port (blue lines). Results demonstrate that independently of the initial perturbed state of the filter, a very good overlap of the filter shapes at convergence is achieved. Since the algorithm aims at minimizing the signal transmission at the cross port, at this port the isolation averaged across the bandwidth B_s =10 GHz of the signal is the maximum the filter can provide, that is higher than 27 dB. In contrast, the isolation at the bar port is lower (< 20 dB), not because of some filter imperfection, but because this parameter is not considered in the cost function of the algorithm. Therefore, the passbands of the filter at the two ports are different, the bar port one (14.5 GHz) being wider than the passband one (9.5 GHz). To achieve a symmetric shape at the two ports, two channels spaced by FSR/2 and labelled with different tones should be simultaneously transmitted through the filter and a suitable cost

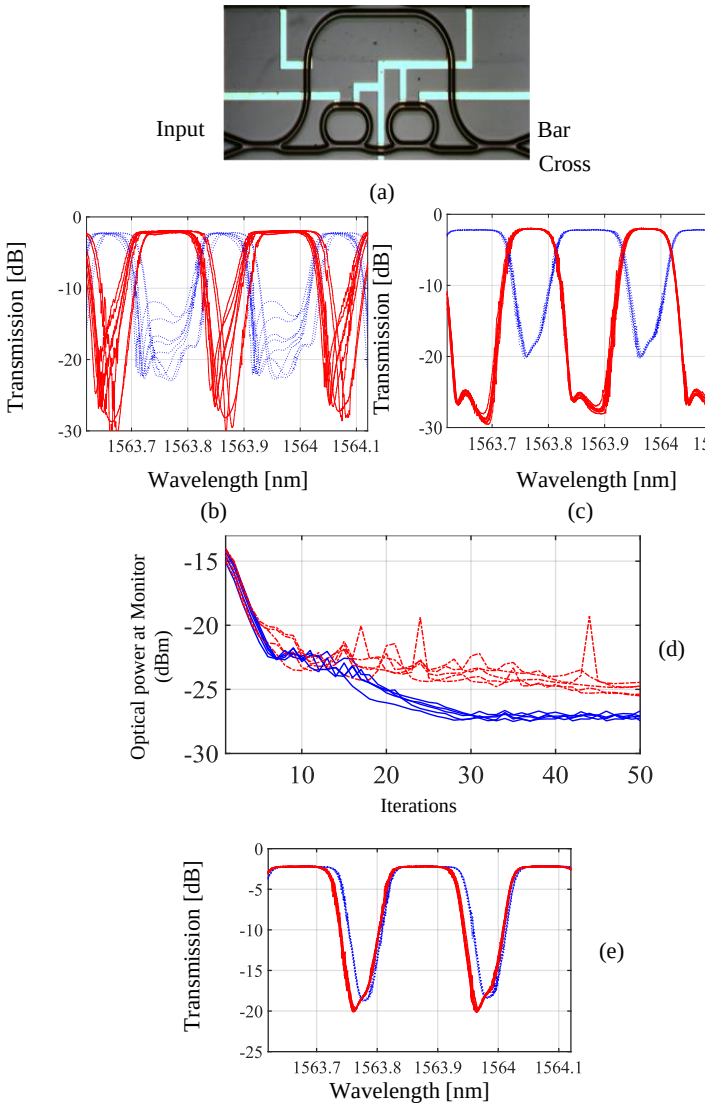

Figure 4.5: *(a) Top view photograph of a SiON MZI loaded with 2 MRRs implementing a tunable bandwidth filter. Measured transmission at bar and cross port in (b) intentionally perturbed states and (c) after automated tuning to a 10 Gbit/s signal at 1563.87 nm. (d) Comparison of convergence performance of the TED-based tuning algorithm using electrically measured (blue) and heuristic (red) T matrix (e) Automated adaptation of the filter spectral response (bar port) when the signal bandwidth is B_s =10 GHz (red) and B_s=28 GHz (blue).*

function should be defined for the tuning algorithm.
The convergence of the tuning is shown in Figure4.5(d) where the optical power at the monitored cross-port versus the number of iterations is shown. Starting from the same perturbed state of the filter, solid blue lines represent the convergence curves when the electrically measured **T** matrix is used in the TED method, while dashed red lines refer to the case of the heuristic **T** matrix of Equ. 3.9 with dimension of 3X3 and identical off-diagonal terms μ = 0.02. In both cases convergence is achieved, but fine optimization at high isolation degree is faster and more robust when thermal crosstalk is better compensated.
Exploiting the tuning on the signal as explained in Section 4.2, the filter adapts to the signal bandwidth. In Figure4.5(e) frequency response of ten tuned filters are presented for the case of Double Polarization - Quadrature Phase Shift Keying (DP-QPSK) modulated channel with B_s =28 GHz in blue and channel with B_s =10 GHz in red in their bar port. Filters tuned to wider channel have broader notches in their cross port frequency response to minimize better the signal (which is not shown in figures), therefore their bar port frequency response demonstrate wider pass bandwidth which is easier to observe (compared) and is presented in Fig4.5(e).

4.2.2 Tailoring filter response to signal spectrum

Frequency response of PIC architectures that are not supposed to have a pronounced reconfigurability (e.g. bandwidth tunability), can be tailored to match to the signal PSD as much as allowed by the design of the function. To demonstrate this concept, we consider the third order coupled resonator MRR filter of Fig. 4.6(a), which was fabricated in the same SiON photonic platform as the device of Fig. 4.5. This index contrast enables the realization of MRRs with an FSR of up to 100 GHz with negligible bending loss. Initial phase perturbations were intentionally introduced in every MRR of the filter by applying random deviations in the voltages driving the heaters around their optimum tuning point. Figure 4.6(b) shows the measured Through and Drop port transmission of the perturbed filter when the frequency spread of the MRR resonances is as large as 100 pm (12.5 GHz).

As a first example, we used an intensity modulated 5 Gbit/s OOK input signal with a carrier wavelength λ_1 = 1565.470 nm, whose bandwidth $B_s = 5GHz$ well matches the nominal filter bandwidth $B_f = 6.5GHz$. The optical power is measured through an external photodiode and transmitted to a PC where a TED-based gradient-descent tuning algorithm (details

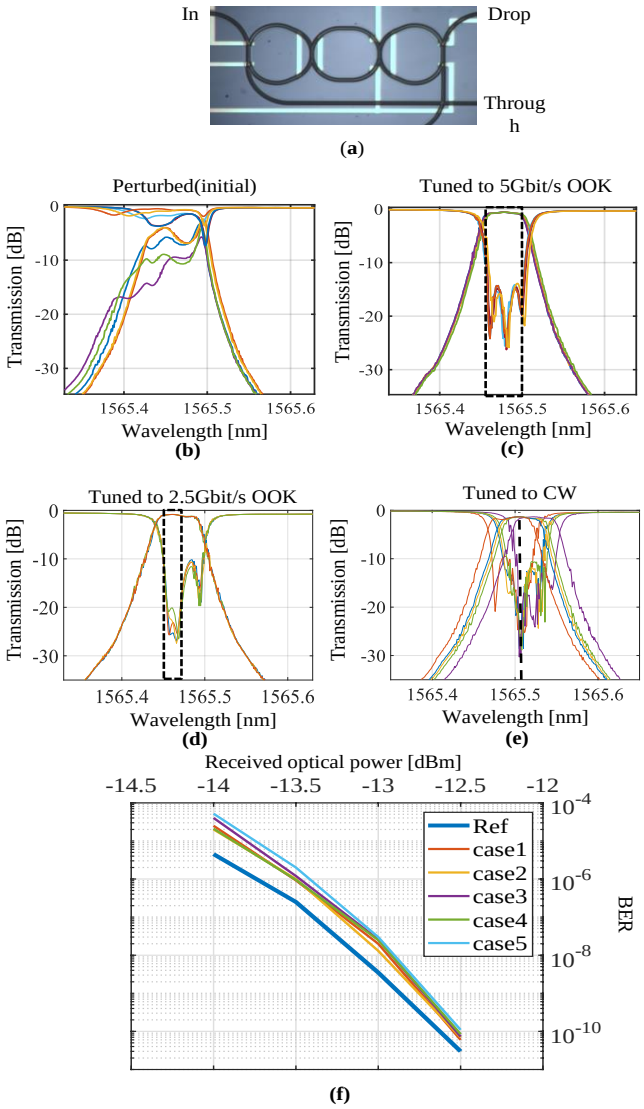

Figure 4.6: *Tuning to optical signals: (a) top view photograph of the 3rd order MRR SiON filter. Measured frequency response at Drop and Through ports for (b) intentionally random initial states and after automated tuning using as an input signal (placed at position of dashed box): (c) a 5 Gbit/s OOK channel, (d) a 2.5Gbit/s OOK channel, and (e) a CW laser source (no modulation). (f) BER measurements of a 2.5 Gbit/s OOK channel transmitted at the drop port of the automatically tuned filter. The blue curve is the reference BER obtained at Through port when the filter is detuned from the signal.*

in [75] and chapter 3) was employed to minimize the output power transmitted at the Through port. As a metric for the performance of the automated tuning we assume the Through port isolation I_B averaged across the bandwidth B_s of the signal (centered around λ_1). The transfer functions of the tuned configurations of filter for Through and Drop port are shown in Fig. 4.6(c). The dashed box indicates the wavelength range B_s occupied by the signal. The overlap among all the measured curves, regardless of the initial perturbed state, demonstrates the accuracy of the tuning procedure, guaranteeing an isolation I_{5GHz} = 15 dB. It should be noted that in this condition ($B_s \neq B_f$), the frequency response of the filter is the nominal one, that is achieved when the three MRRs resonances are aligned. Starting from the same random filter configurations as in Fig. 4.6(b), we reduced the data rate of the signal to 2.5 Gbit/s, thus having the bandwidth B_s smaller than 5GHz. As shown in Fig. 4.6(d), the filter is now automatically tuned to a shape that is much different from the one shown in Fig. 4.6(c). In this case, where $B_s < B_f$, the three MRRs are not resonating at the same wavelength, but this filter shape provides higher isolation ($I_{2.5GHz}$ > 20 dB) across the signal bandwidth (dashed box).

The automatic tailoring of the frequency response of the filter according to the PSD of the input signal is even more pronounced if the data modulation is switched off. As shown in Fig.4.6(f), the frequency responses achieved using a CW source at a wavelength of 1565.5 nm overlap well only at the wavelength of the optical signal, where an isolation I_{CW} = 30 dB is achieved. Yet, the automated tuning does not bring the filter to a unique filter shape. This is strongly related to the fact that $B_s \ll B_f$. In fact, at wavelengths where the signal PSD vanishes the tuning algorithm is unconstrained and may converges to random filter shapes. To demonstrate that the automatically tuned frequency responses of the filters are equivalent for the considered input channel, we measured the BER of the 2.5 Gbit/s OOK signal used in Fig. 4.6(d) when it is transmitted to the Drop port of the filter. BER curves in Fig. 4.6(f) were achieved from 5 different drop-port filter configurations, after convergence of the tuning algorithm from different initial states of the filter. All the considered cases share the same BER performance, with less than a half dB power penalty with respect to the reference BER obtained by off-band transmission at the Through port.

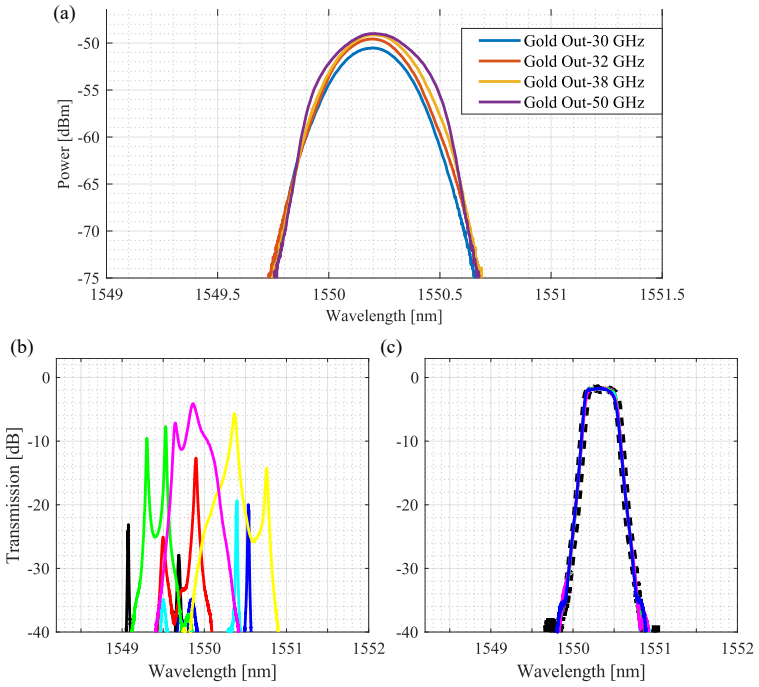

Figure 4.7: *(a) Optical signals dropped by the Golden filter set for its different configurations, these configurations are extracted from stored values of tuning for different signals PSDs. (b) Random initial cases of filter.B representing effects of fabrication tolerances on neighboring filters on a wafer. (c) Frequency response of cloned filters (solid curves other than black) to the frequency response of Golden filter in dashed-black curve.*

4.2.3 Filter replication

Using the signal spectrum to tune the PIC allows matching , as close as possible by the design of the filters, frequency response of the optical function to the PSD of the signal. The signal PSD at output port of a PIC has specific information about the status of that device which can be used to tune similar devices to replicate these features. For example, if the signal that is used to tune the PIC.**B** is from the output of the PIC.**A** with a flat signal (in frequency domain) as its input, the optical function **B** is tuned to match to the frequency response of the optical function **A**. In other words, optical function **A** is the "Golden" reference to be used in calibration and tuning of the similar family of filters. This concept can dramatically change the time and resources needed in device qualification and calibration process. Input to the Golden filter should be an appropriate signal to be curved with frequency features of the Golden filter. Wide span sources or even noise

out of optical amplifier can be suitable candidates. Choice of output port of the Golden filter should be done based on the features that are needed to be replicated. For example in coupled MRR filter bandwidth information can be found on Dropped signal or depth of channel rejection in Through port.

To demonstrate this idea, we use two 4th order coupled MRR filter fabricated in SOI technology. These filters present 40GHz of 3dB bandwidth with more than 90nm of FSR while having less than a dB of insertion loss. Further details of the filter design and control strategies are presented in Sec. 5. Lets consider connecting these two filters with Drop port of Filter.A being connected to the Input port of Filter.B. Filter A is automatically tuned using TED-based algorithms and its actuators set points are stored in LUT.A. Flat spectrum signal filtered with a 2nm filter is launched at input port of filter A. Figure 4.7(a) presents measured optical power at filter.A Drop port when the filter configuration is changed from its LUT for different channels bandwidths. PSD of these signals have traces of the frequency features of filter.A which can be used as a valuable information to tune others filters to replicate these features. In this experiments, we used the Dropped optical signal from filter.A as input signals for filter.B and used TED-based algorithms to tune them from random initial conditions presented in Fig. 4.7(b). These initial conditions can be due to fabrication tolerances for multiple filters on the same wafer. Bandwidth information inside the dropped signal from the Golden filter (filter.A) is enough to create a clone of the Golden filter on the filter.B. Figure 4.7(c) shows the tuned frequency response of filter.B (solid lines with colors other than black) starting from random initial cases overlapping closely on the frequency response of the Golden filter (filter.A) in dashed-black curve. Using other configurations of the Golden filter in Fig. 4.7(a) allows us to clone these configurations on filter.B regardless of their initial conditions (see Sec. 4.2.2 for details). This concept can be adopted in calibration phase of PICs to automatically create LUTs and in Sec. 4.3 an example is demonstrated and discussed.

4.3 Automatic calibration and dynamic Look Up Tables

The control and calibration techniques described in the previous sections enable the automatic tuning and locking of a device to the desired working point, even in an adaptive way. However, when the device is far away from the target functional state because it is in the initial state or a consistent variation of the working point is required, the device usually needs to be led to work in the desired condition using pre-determined values for its control parameters which are stored in a LUT. Building up a LUT is usually very time consuming, because the device is in an unknown state and specific procedures need to be followed which are heavily dependent on the circuit architecture, on the working conditions, and on the initial state of the circuit.

An efficient process to generate the LUT can exploit the automatic tuning process using the thermal crosstalk free tuning algorithms, the modulated channel as feedback signal and possibly the pilot tones to discriminate the desired signal. Once the tuning reaches the convergence, the final currents/voltages of the actuators are stored in the LUT. These LUTs can be even dynamically updated during the operation of PIC to match the new requirements of the system, for example when the channel modulation format or the thermal crosstalk form neighboring devices changes.
We applied these concepts to the automated generation of a LUT for an add/drop filter operating on a DWDM grid. The block diagram of the considered device along with the control loop scheme is shown in Fig.4.8(a). The filter unit is a 3rd order coupled MRR filter, which is designed to have 1 THz (8 nm) FSR, 40 GHz 3dB bandwidth, and 20 dB in-band isolation. A thermally tunable unbalanced MZI is employed as a tunable switch to provide a hitless functionality [80]. A second balanced MZI is integrated at the Add port and it is used as a channel labeler to carve the added channel with a weak pilot tone in order to make it distinguishable from the other DWDM channels incoming form the Input port. A transparent detector (CLIPP) [40] is integrated at the Drop port in order to read the residual power of the added labeled signal, thus providing an error signal to the controller without affecting the dropped signal. More specifically, the CLIPP reads the label amplitude through a lock-in detection scheme [33]. An FPGA reads the CLIPP measurements while controlling the heaters alongside the filter. A microscopic picture of the photonic chip fabricated on a Si photonic platform is shown in Fig.4.8(b). More details on the filter architecture can be found in [80].

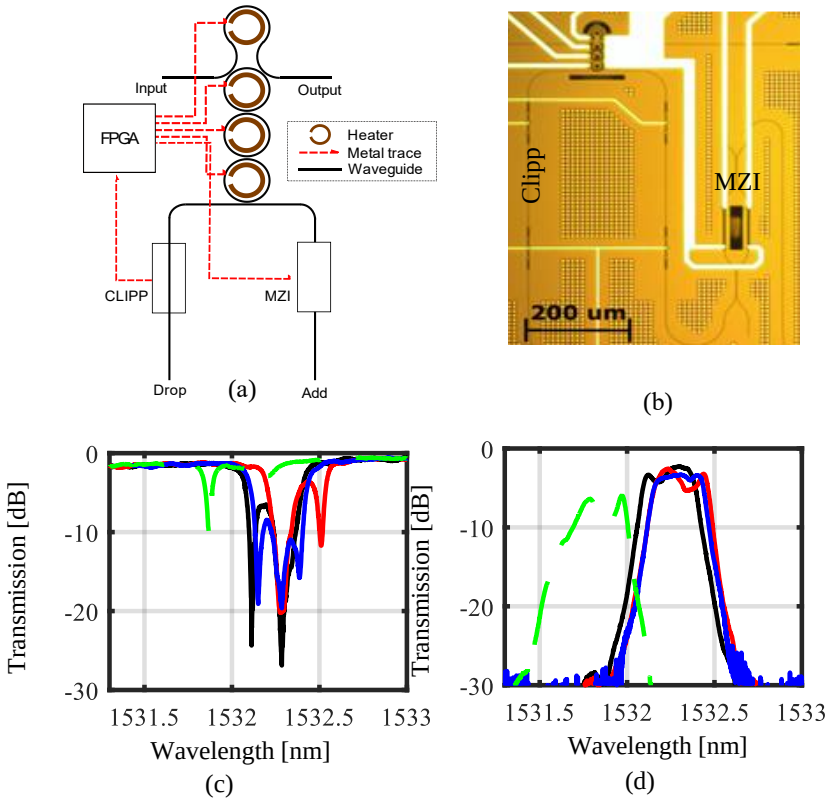

Figure 4.8: *(a) Functional block diagram of a reconfigurable hitless filter along with the relevant control elements adopted to demonstrate fine tuning and automatic look up table creation (b) Top-view photograph of overall filtering unit realized on a silicon chip, including monitoring CLIPP detector and on-chip MZI labeler to mark the added signal. Through (c) and Drop port (d) frequency response of filter starting from same initial conditions (natural response in green-dashed) and tuned by using a 100Gbit/s DP-QPSK signal (blue), a 10 Gbit/s OOK signal (red) and CW source (black).*

Starting from the natural frequency response of the filter (green-dashed curves in Fig.4.8(c) for Through port and in Fig.4.8(d) for Drop port response), a modulated channel at 1532.25 nm is launched in the Add port and is labeled by the integrated MZI (11 kHz, modulation depth <8%). Figures 4.8(c,d) present the frequency response of the tuned filter, when the input signal is modulated according to a 100 Gbit/s Quadrature Phase Shift Keying (QPSK) (blue curve), 10 Gbit/s OOK (red curve) and when no modulation is applied (black curve). The frequency response of filter is reshaped to match the PSD of the employed signal. The narrower filter bandwidth

obtained with the CW channel allows to achieve higher in-band isolation (I_{CW} = 27 dB) while for 100 Gbit/s QPSK channel, a larger bandwidth and a corresponding lower in-isolation across the 28 GHz signal bandwidth (I_{100Gb} = 18 dB) is achieved. Ripples of filter tuned to 10 Gbit/s OOK transmitter are out of the bandwidth of the signal therefore not perturbing the quality of the channel.

Once the filter has been tuned at the first channel of the DWDM grid, the procedure can be iterated to create the LUT over the entire operative wavelength range. We used a commercial 100 Gbit/s transmitter whose carrier wavelength, data rate and modulation format can be selected and a LUTs matching an arbitrary sequence of optical channels has been created. In our setup the FPGA selects the carrier wavelength of the modulated input signal fed to the Add port of the filter and execute automatically the tuning algorithm to find the tuned parameters of the filter for that channel. This is repeated till the table is filled up based on the performance requirements of the filter along the frequency band.

To illustrate this approach, let us consider an architecture including a pair of neighbor add-drop filters as in the scheme Fig.4.9(a). Figure 4.9(b) shows the tuning of filter I when eight different channels with 100 Gbit/s QPSK modulation and 50 GHz frequency spacing are sequentially provided at the input. The Drop and Through port transfer functions of the filter controlled by this automatically created lookup table are very well in line with the reference shape shown in Figs. 4.8(c)-(d). To check if the LUT can be created and dynamically updated in presence of perturbations, we used the neighbor filter II, which is connected to the same bus waveguide of filter I. The tuning of filter II is performed by using a 10 Gbit/s OOK modulated channel when filter I is operative (that is when it is tuned to one of the eight 100 Gbit/s channels). Figure 4.9(c) shows that the frequency response of filter II is automatically shaped to match the expected channel bandwidth [see 4.8(c)-(d)], regardless of the tuning state of the adjacent filter I. In other words, a LUT for filter II (and vice-versa) can be created and updated regardless of the thermal crosstalk from surrounding devices.

As a final demonstration let us consider the scenario of elastic networks [83], where optical channels can change their bandwidth (modulation format or bit rate) or even wavelength placement during operation. By using our tuning-to-signal approach, the LUT is automatically updated for this new status. For instance, starting from the configuration of Fig. 4.9(b) for filter I, let us assume that channels number 2, 5 and 7 change their modulation scheme from 100 Gbit/s QPSK to 10 Gbit/s OOK and channel

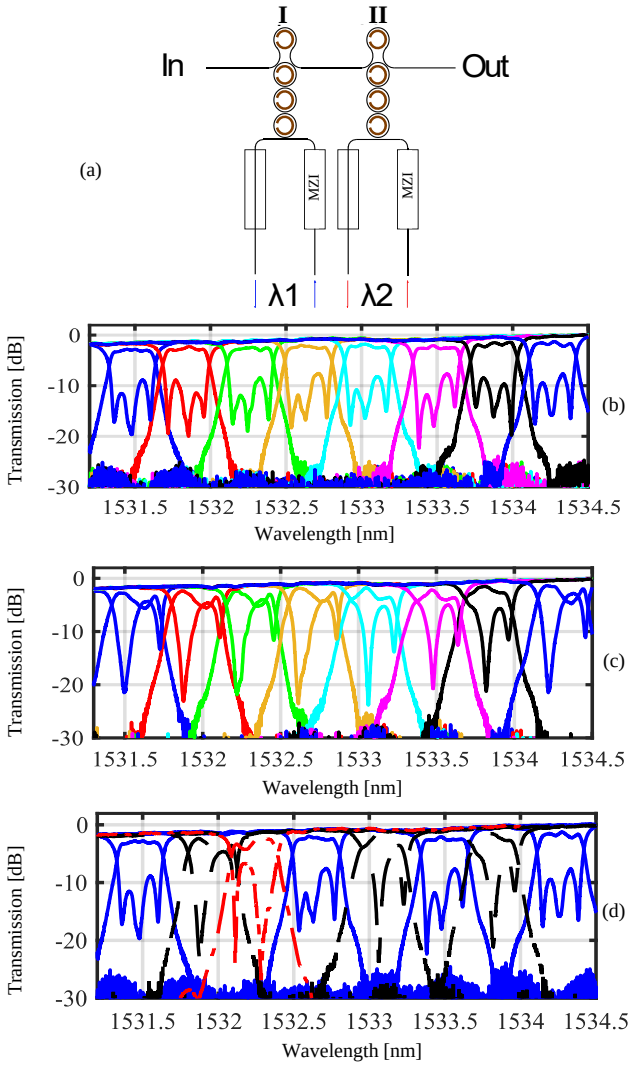

Figure 4.9: *(a) Functional block diagram of two reconfigurable add-drop filters sharing the same bus waveguide, demonstrating a bi-channel add/drop block (b) Through and Drop port frequency response of filter I with automatically created lookup table for ten 100 Gbit/s DP-QPSK channels spaced by 50 GHz. (c) Through and Drop port transfer function of filter II (while filter I is operative) from automatically generated lookup table for ten 10 Gbit/s OOK channels spaced 50GHz apart. (d) Drop and Through port transfer function of filter I according to a flexible channel grid with three 10 Gbit/s OOK channels (black dashed), one CW signal (red dash) and four 100 Gbit/s QPSK (blue solid).*

3 remove its modulation and transmit only the carrier [(channel numbering is here defined from left to right on Fig. 4.9(b)]. Figure 4.9(d) shows for Drop and Through ports transfer function according to the modified channel grid, where the black dashed line represent the three 10 Gbit/s OOK channels, the red line is the filter tuned to a CW signal, and the blue lines are the original four 100 Gbit/s QPSK of Fig. 4.9(c).

4.4 Topological redundancy in optical design

PIC design process can be tailored considering the control-ability of the function accounting from possible tolerances of fabrication to possible reconfiguration required along the operation. This can be done by simulating the designed optical function taking into account the imperfection of fabrication and evaluating its performance being tuned to desired conditions. In chapter 5 we further discuss and demonstrate this idea for a complex PIC presenting outstanding frequency response on wide band of operation. We suggest instead of synthesis design based on pure mathematical models, we take into account the realistic imperfections along the design process. Like variation of directional couplers along the wavelength range, dispersion of waveguides or tolerance of fabrication. A more realistic simulator implemented in an optimization algorithm can start from a pure mathematical design of a device and end to a model robust and resilience against mentioned variations and imperfections. This optimization step in design procedure can try and quantify the tunability of the device for different scenarios like various modulation scheme of the channel and optimize the design of the device to offer better tunability. Section 5.2 discuss and implement this concept for design of a complex PIC offering novel functionalities.

In this section, we suggest considering unpredictable malfunctions of PIC due to extreme fabrication tolerances or even max rating operation range leading to malfunction of the overall device. Usually in this cases there is no plan B and the PIC is unusable. In some scenarios careful design consideration can allow partial recovery of PIC functionality. Lets consider integrated mesh structures (see appendix B) as case of study operating on free space beams which are being coupled in to integrated mesh stricture by grating coupler (2.5.1).

Mesh partitioning and pixel subset grouping. The connection between the arrangement of grating couplers and the mesh architecture can be optimized in order to make the optical processing of the input beams

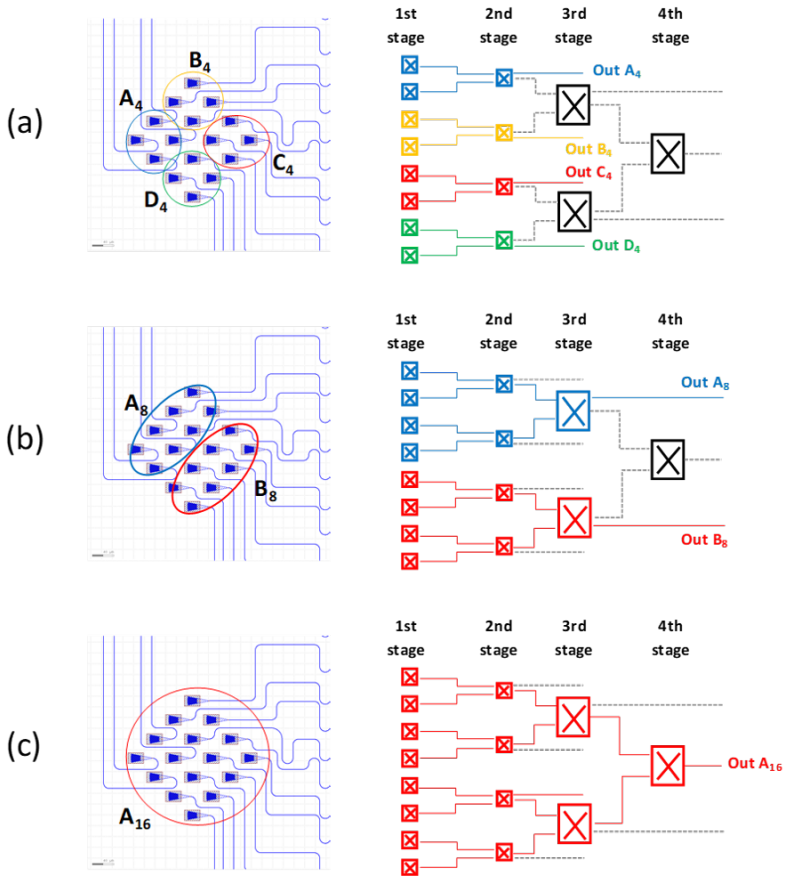

Figure 4.10: *Mesh partitioning and pixel subset grouping. A 16-elements super-pixel is suitably connected to a 4-stage MZI binary tree mesh in order to allow functional flexibility: (a) 4 subsets of 4 pixels independently processed by 4 parallel 4x1 meshes (different colours); (b) 2 subsets of 8 pixels independently processed by 2 parallel 8x1 meshes; (c) all the 16 pixels are processed by the full mesh operating on a single optical beam (highest resolution).*

more flexible and adjustable on demand. Figure 4.10 shows one of the designs conceived for this structures, consisting of a 16 element pixels connected to a 16x1 binary tree mesh of MZIs (see Sec. 6.1). With this architecture we can select how to process the 16 pixels by partitioning them into different subsets of pixels, such as for instance:

- (Fig. 4.10.a) 4 subsets of 4 pixels (namely A4, B4, C4 and D4) can be processed in parallel by four 4x1 sub-meshes (highlighted with different colours), comprising the first 2 MZI stages of the full mesh. In this way, 4 different beams, each impinging on a different 4-pixel

subset (light propagating rightwards), can be extracted from output port Out A4, Out B4, Out C4 and Out D4 , respectively. Reversing the direction of the light propagation, this structure can be operated as programmable beam sender for 4 different beams which can be independently managed.

- (Fig. 4.10.b) we can increase the resolution by increasing the number of pixels in each subset, for instance considering 2 superpixels made of 8 pixels each (namely A8, B8). In this case, the two sub-meshes comprising the first 3 MZI stages of the full mesh needs to be used.
- (Fig 4.10.c) the maximum resolution is achieved by collecting the light captured by all the pixels with the full 4-stage mesh.

This means that, given the number of pixels (16 in this example), we can dynamically select the better trade-off between the required resolution and the number of beams to be processed. Malfunction of different MZ units has different consequence on the performance of the overall PIC depending on its position in the chain but with this careful design there is chance of maintaining the operation of the PIC in these unfortunate scenarios, of course with lower functionalities.

4.5 Reduction of electrical I/Os

Size of dense PIC is usually limited by space needed for I/O specifically the electrical interfaces. Each electrical components (heater, PD or VOA) requires two electrical routing, multiples of components can share common ground line (subject to limitations of technology). The need for further reduction of electrical I/O can be more appreciated in a large circuits when comparing size of electrical pad arrays for I/O and size of the optical circuit itself. In addition to develop new control strategies to limit the number of sensors required to control the PIC (see Sec. 6.2 for case of MZI meshes), we explored new approaches to reduce the number of electrical I/O pads needed.

Working on a silicon platform, a viable strategy is to switch multiple electrical signals on a single pad by using an analog multiplexer embedded on the silicon photonic chip. A digital code of n bits controls the multiplexer and it allows to select between 2N on-chip electrical signals the one to be connected to the I/O pad. Therefore, it is possible the connection of up to 2N electrical signals using just N+1 pads. Figure 4.11(a) shows an example of this approach applied to a mesh of MZI. The cathode of the

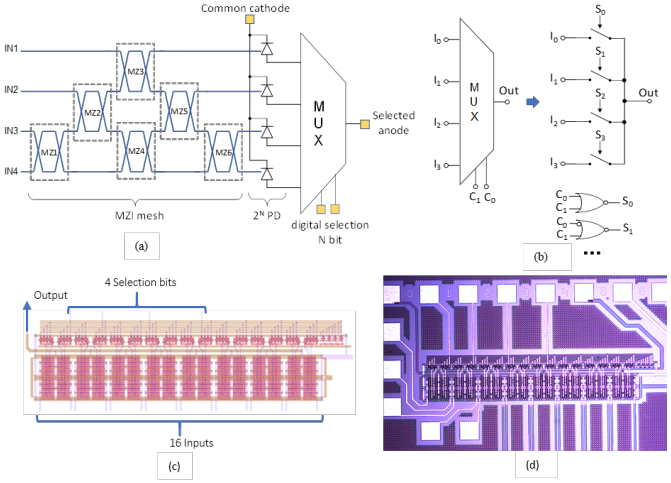

Figure 4.11: *(a) Reduction of the pads required by silicon MZI mesh through an on-chip analog multiplexer to digitally select the photodiode at the output node. (b) example of internal structure of a 4:1analog multiplexer. (c) chip layout and (d) microscopic picture of electronic multiplexer implemented in a silicon photonic chip.*

photodiodes at the end of the mesh share the same bias voltage. The anode of each diode is connected to an on-chip multiplexer whose output node can be connected to an external TIA for the readout of the optical power. Thanks to the use of the multiplexer is possible handle all the photodiodes using a time-division multiplexing technique on the single output node.

An example of analog multiplexer architecture is shown in Fig. 4.11(b). Each analog input is connected to the output node through a voltage-controlled switch. A digital circuit (decoder) closes the single switch matching the binary input. The key element to implement such structure is the MOS transistor: it can be operated as a voltage-controlled switch and allows the implementation of any logic gate. Figure 4.11(c) present the chip layout of implemented electronic multiplexer and (d) the microscopic picture of the fabricated chip.

Another strategy that we suggest to explore is to reduce the number of electrical I/Os by optically grouping the control ports of a mesh, according to device concept of Fig. 4.12. As discussed in Sec. 6.2 “Self-configuration of cascaded MZIs”, automatic configuration of MZI meshes relies on the coherent sum of the power at the selected output port, that is on the minimization of the output power at all the other optical ports, also referred to as “control” ports. When the size of the mesh scales up to a large number of MZIs, the number of monitor photodetectors to be used scales up

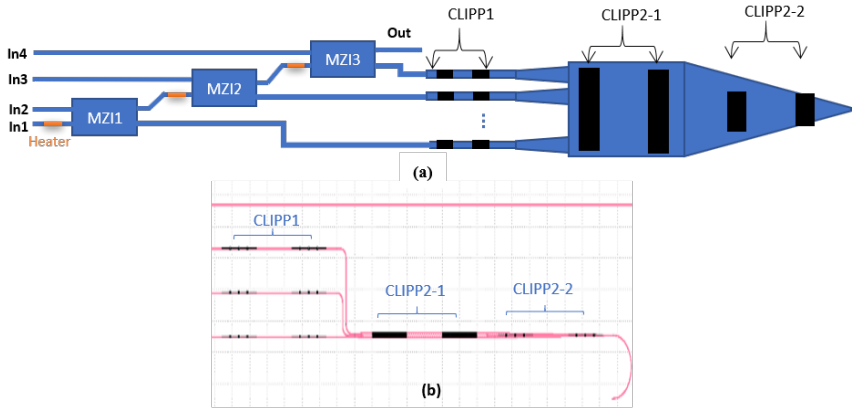

Figure 4.12: *(a) Schematic and (b) chip layout of suggested circuit to minimize the number of detectors in control of mesh. Grouping every n control port of MZIs into a multimode waveguide (MMW) and using a single detector (CLIPP) instead of n detectors. MMW is tapered in to dissipate the optical power (as termination). Two versions of CLIPP detector is used (CLIPP2-1 and CLIPP2-2) to compare performance.*

accordingly, together with the required number of electrical connections. However, since the power to be minimized is the overall power carried by the control ports, we can couple these waveguides to a common multimode waveguide (MMW) and monitor the overall optical power in that waveguide by using a single photodetector. In this way we can reduce the number of detectors and in return the number of electrical I/Os.

Based on this concept, A test structure is proposed in Fig. 4.12(a) and was designed which allows controlling a mesh with 3 monitoring waveguides. In order to assess the performance of the proposed solution we integrated different kind of detectors in the same structures:

- Three in line transparent detectors (indicated as CLIPP1 in Fig.4.12(b) chip layout) are integrated on the three single mode output waveguides of the mesh to measure the optical power in each waveguide individually and provide the reference value;
- A transparent detector (CLIPP2-1) integrated in the MMW to monitor the overall power.
- The MMW is tapered down to radiate out the optical power avoiding unwanted back reflections. In this tapered section a third transparent detector (CLIPP2-2) is integrated which is expected to exhibit a high

responsivity because of the higher interaction of the guide modes with the waveguide surface in the tapered region.

It should be noted that, even though a single photodetector is integrated in the multimode waveguide, in principle this could be used to identify also the power intensity individually carried by each input single mode waveguide, provided that the incoming beams are suitably labeled with pilot tones (Sec. 4.1.1).

4.6 Summary

In this chapter, we discussed some techniques and tricks which can be adopted both in the design and control phase of the PIC implementation help solving some fundamental problems. Problems rising from the nature of these devices like uncertainty in direction of the slope in frequency response or distinguishing a specific channel between the WDM grid using only optical power. We suggested using signal optical power at a specific port as the merit in tuning, we can optimize the frequency response of the device to match to the PSD of the channel. In other words, frequency characteristics of the device is tailored and adapted to the PSD of the channel. This idea gave birth to concepts like dynamic LUTs and filter replication [79]. Output optical signal from a tuned filter can be used to reshape the frequency response of other filters obtaining the same behavior. This concept can be used to replicated the frequency response of the well tuned filter to create appropriate LUTs to guarantee the performance of the device. These LUTs can dynamically update themselves form the converged values of control algorithm to maintained the top performance of the device in presence of aging or variation of operation conditions. This chapter is finished by two design suggestions to improve the resilience of the PICs against fabrication tolerances and reduce the electrical I/O footprint in photonic chips. We examined these concepts on various PICs to evaluate their effectiveness and application. In next two chapters (Chp.5 and Chp.6) we adopts these approaches to design and control two complex PICs and demonstrate interesting applications based on their reconfigurability.

CHAPTER 5

FSR free and hitless-tunable filter

Optical filters that can be tuned across a wide wavelength range are essential functional blocks of optical data communication systems. Flexible and dynamic bandwidth allocation of WDM channels among reconfigurable nodes is a key enabler for capacity growth and management of core networks, 5G back-haul networks, intra- and inter-datacenter interconnects. For more than two decades integrated photonics has been proposed as a promising technology for realization of compact, low cost, low-power consumption tuneable WDM filters. In particular, coupled MRR architectures fabricated on high-index-contrast platforms, such as SiP, can provide good spectral performances in terms of wide passbands (several tens of GHz), steep roll-offs, high extinction ratios (> 50 dB). On paper, these filters can also fulfill three main requirements which are fundamental to bring them from lab experiments to real applications: i) operation and tuneability across a wavelength range of several tens of nanometers, matching for instance the gain bandwidth of semiconductor and fiber amplifiers; ii) possibility of dynamically re-routing selected subsets of channels (i.e. wavelengths), while keeping full transparency for all the other channels transmitted though the device, this feature being typically referred to as "hitless" tuneability; iii) insensitivity to the polarization state of the input

light signals, that translates into a low PDL and low polarization dependent crosstalk.
Actually, we say "on paper" because these requirements have been achieved only individually by some device concepts reported in the literature, but no devices have been ever demonstrated satisfying them all. For instance, wide wavelength range operation (up to about 40 nm [84,85]) was reported in silicon MRR filters designed according to Vernier schemes [86], that is by cascading resonators with different FSRs. Polarization independence was demonstrated in silicon nitride MRR filters by using a polarization diversity scheme [87], but without hitless tuning functionality. Only a few filter architectures were proposed that successfully implement hitless tuneability: in [88,89] tuneable couplers are used as switches to disconnect the filter from the input bus waveguide, yet this approach does not apply to broadband Vernier schemes because of the appearance of off-band notches during tuning operations; in [90–92] a MZ bypass switch is exploited to transfer the entire input channel grid to an auxiliary filter bank, but this requires duplication of the entire filter architecture together with its control electronics.

In this thesis, we report on an ultra-wide-band polarization-insensitive hitless tunable filter providing a positive answer to all the above mentioned requirements. Noteworthy, the solution we propose does not come from a customized technology process, but it can be implemented on standard SiP platforms. Ultra-wide-band operation is achieved through a modified Vernier scheme based on non-integer ratios between the FSR of the MRRs, resulting a non-periodic, theoretically FSR-free, frequency response of the overall filter. Hitless tuning is operated by introducing controllable loss in the MRRs of the filter through the use of p-i-n junctions acting as fast (ns time-scale) variable optical attenuators (VOAs). Resonance-enhanced loss is exploited to intentionally cancel out the passband of the filter with negligible impact on the off-band response. The proposed filter concept is embedded in a polarization diversity scheme demonstrating polarization-insensitive single passband filter with hitless tunability across a wavelength range of 100 nm (1520 nm- 1620 nm, limited by experimental equipment).

5.1 FSR free filter

Silicon MRRs filters are good candidates for WDM filters operating on high data-rate channels because they can achieve wide bandwidth while keeping compact footprints. To increase the FSR of a coupled MRR filter with rings of the same size, the bending radius of the MRRs must be reduced. To cover a wavelength range as large as 40 nm, bending radii below 3 μm would be required, which result in high radiation loss and severe performance degradation [93]. Moreover, the minimum size of the MRRs is also limited by the maximum temperature achievable by the thermo-optic actuators employed for the tuning. To realize filters operating on a broad wavelength range, Vernier schemes can be used [86], where MRRs with different FSRs are employed. In this schemes, since the resonances of each MRR occur periodically forming a comb spectrum, they will overlap only at certain wavelengths, while suppressing all the resonances that lie in between. Typically the ratios between the FSRs of the various MRRs are selected according to integer numbers and with this strategy tuneable filters working across a wavelength range as large 32nm in [85] and 36.7nm in [84] were demonstrated.

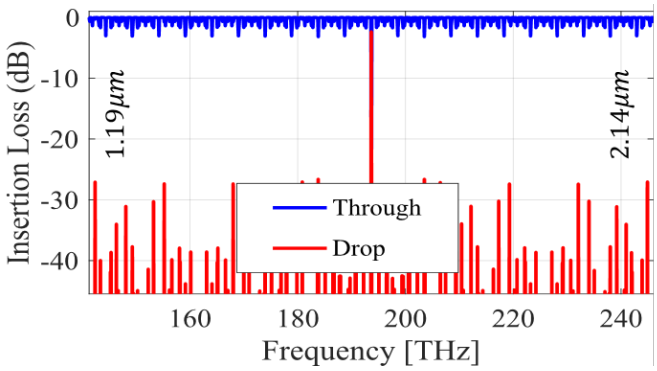

Figure 5.1: *Through (blue) and Drop (red) port simulation of the Vernier filter designed according to non-integer FSR ratios (no wavelength dependence of directional couplers) exhibiting FSR-free operation across more than 120 THz (1 µm wavelength range).*

In this thesis we propose a modified Vernier scheme, using non-integer ratio among MRR sizes, resulting to larger wavelength distances for alignment of all resonators leading to wider FSR of the device. Non-periodic frequency response with a single-pass-band characteristic spanning across more than 120 THz (1µm wavelength range) can be theoretically achieved (simulation results in Fig. 5.1 while intentionally neglecting the dependent

of couplers on wavelength), while keeping the MRR bending radius well above the lossless regime for silicon waveguides (Ri > 7 μm) [93].

5.1.1 Filter Structure

Figure 5.2 illustrates the concept of the filter architecture, which consists of a chain of directly-coupled MRRs connected to two bus waveguides via tuneable couplers implemented by means of MZIs. The MRRs have suitably different radii in order to realize a Vernier scheme [86], but, with respect to conventional Vernier-based filters, non-integer ratios between the FSR of the MRRs are used to cancel out the periodicity of the frequency response of the overall filter (FSR-free response). The design procedure starts from an integer-Vernier master filter [94] matching the pass-band frequency response specifications and a reasonable large FSRs.

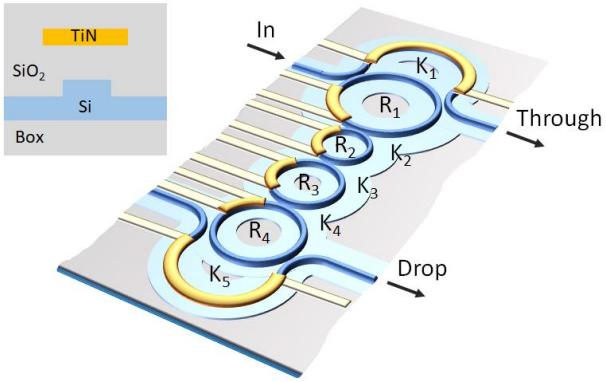

Figure 5.2: *Schematic of the 4th order MRR Vernier filter with Mach-Zehnder basesd bus tunable couplers. TiN heaters, controlled individually, are placed 700 nm above the waveguide core;*

Then, the radii R_i and the coupling coefficients K_i of the MRRs are optimized starting from the nominal design according to a numerical procedure described in Sec. 5.2.1 in order to achieve FSR-free frequency response, while keeping the spectral shape of the main passband over the broadest wavelength range. When the filter pass-band is tuned at different wavelengths, the power split ratio of the input/output MZIs is adapted in order to counteract the wavelength dependence of the inner directional couplers and guarantee the best impedance matching from the bus waveguides to the filter [94, 95].

5.2 Design parameter and Optimization algorithm

Here we explain the optimized design procedure based on non-integer Vernier scheme explain in Sec. 5.1 to design a non-periodic filter reconfigurable along the wide band delivering desired performance while being resilience against fabrication tolerances. Design parameters are reported alongside actuators implemented to tune the resonance point of MRR for reconfiguration.

5.2.1 Optimized design procedure tailored for controllable device

In our filter we employed a modified Vernier scheme based on non-integer ratios between the FSRs of the MRRs, demonstrating that this modification can bring to a frequency response that is theoretically aperiodic (FSR-free filter). The schematic of the filter architecture is shown in Fig. 5.2. The two tuneable couplers are connecting the filter to the bus input/output waveguide allows the compensation of the wavelength dependence of the couplers along the band. The procedure follows three main steps:

(i) **Identification of a 4-th order master filter.** This is the seed of our optimization procedure and consists of a Vernier filter with integer FSR ratios. The design of this filter can be performed by using conventional techniques for the synthesis of coupled resonator filters [94] (see Appendix. A.3). Here, we considered all the possible configurations for the FSR of the four MRRs, which were supposed to be an integer fraction of the targeted FSR (4.8 THz) of the whole filter. This means that the FSR of the MRRs can assume values of 4.8THz/q_i with the integer q_i being conveniently comprised between 3 and 6. Among these combinations, we selected the configuration with integer ratios q_i = [5 3 4 5] ($i = 1, 2, \cdots 4$) which guarantees the lowest off-band transmission peaks in the Drop port (< 30 dB) and the shallowest transmission notches in the Through port (< 1.5 dB). The coupling coefficient of the master filter K_i = [7%, 0.8%, 0.35%, 0.98%, 6%] provide a passband of 40 GHz.

(ii) **Generation of a non-periodic filter.** The integer ratios q_i of the master filter are modified around their nominal value in order to improve the off-band response of the filter. More specifically, a numerical optimization is performed targeting to cancel out the Drop port transmission at the passband replicas (4.8 THz from the nominal passband), while keeping low off-band transmission peaks in the

Drop port and the shallowest transmission notches in the Through port. As a result a Vernier filter is achieved with non-integer ratios q_i = [5.73 3.3 4 4.8] with a single transmission passband across a frequency range of more than 100 nm, as shown in Fig. 5.3. At this the stage the coupling coefficient K_i are not modified and are considered wavelength independent.

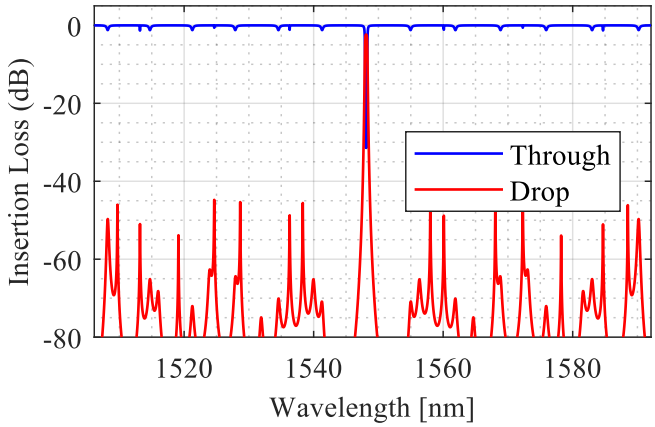

Figure 5.3: *Frequency response of 4th order coupled MRR filter with 40GHz bandwidth and more than 100nm of FSR*

(iii) **filter optimization** In the last step, the in-band response of the filter is optimized across the targeted wavelength range (1520nm-1600nm) by modifying the coupling coefficient K_i of the MRRs. To this aim the wavelength dispersion of the waveguide and of the directional couplers was taken into account. For the optimization procedure, we considered the passband of the filter tuned at three different wavelengths (namely 1520 nm, 1545 nm and 1570 nm) and a cost function was defined to minimizing the spread of the spectral response with respect to the target filter specification (3dB bandwidth of 40GHz, 18 dB of Through-port in-band isolation, 20dB Drop-port isolation at 50GHz distance from the centre of the filter details in Appendix A.1). The experimentally measured frequency response of the optimized filter with coupling coefficients K_i = [7%, 1%, 0.3%, 0.8%, 6%] ($i = 1, 2, \cdots 5$) is shown in Figure 5.4 and key metrics are given in Table 5.1. The off-band response of the optimized filter has Drop-port transmission peaks lower than -30 dB and Through-port notches of less than < 1.2 dB.

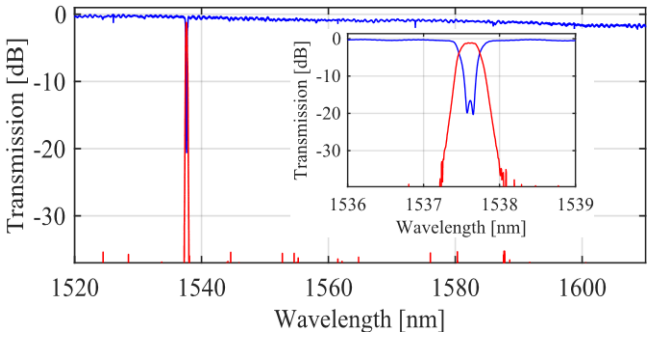

Figure 5.4: *Frequency response of the silicon filter with passband tuned around 1537.7 nm and FSR-free behavior across a 90 nm wide wavelength range (limited by experimental instrumentation). In the inset, zoomed view over a 3 nm range around the passband.*

Vernier Filter	3dB BW	50GHz Iso.	100GHz Iso.	Max Port Iso.	Max Notch Depth
@ 1545 nm	43.9 [GHz]	-22.5 [dB]	-51 [dB]	-28 [dB]	-1.2 [dB]
@ 1570 nm	47.9 [GHz]	-20.1 [dB]	-50 [dB]	-20.5 [dB]	-1.2 [dB]
@ 1520 nm	39.5 [GHz]	-25.2 [dB]	-53.2 [dB]	-25 [dB]	-1.2 [dB]
Specification	40 [GHz]	20 [dB]	30 [dB]	18 [dB]	-1.2 [dB]

Table 5.1: *Performance of 4th order filter based on non-interger Vernier scheme*

5.2.2 Filter design parameters

The filter is designed to have a 40 GHz passband at λ_0= 1538 nm. The radii of the four MRRs are R_i = [14.6 8.4 10.2 12.2] μm, resulting in a FSR of [0.837 1.454 1.2 1] THz, respectively. The power split ratios K_i = [7%, 1%, 0.3%, 0.8%, 6%] (i = 1, 2, … 5) of the directional couplers of the MRRs are optimized by changing the waveguide gap distance g from 200 nm to about 530 nm. The tuneability of the MZI couplers is used to counteract the K_i wavelength dependence of that increases versus g, with a 0.5%/nm slope for the outer directional couplers (g = 200 nm) and a 0.9%/nm slope for the inner couplers (g = 530 nm). The waveguide crossings of the polarization diversity scheme (discussed in Sec.5.4), introduce an excess loss < 0.05 dB and an optical crosstalk < -40 dB on the crossed waveguide, with no evidence of polarization rotation effects (data inferred from measurements on specific test structures).

5.2.3 Filter tuning

The MRR are thermally tuned by means of TiN resitive heaters (480 Ω) deposited on top of the waveguide surface at a distance of 700 nm (see Fig. 5.5.(a). Thermal phase shifters enable the tuning of each MRR over

more than one FSR so as to provide full filter reconfiguration as well as to compensate for native resonance spread induced by fabrication tolerances. The filter is tuned automatically by adapting its shape to match the spectrum of a 100 Gbit/s QPSK channel (28 GHz bandwidth), whose carrier frequency sets the center of the filter pass-band, according to the technique described in [96] and in Sec. 4.2. Mitigation of thermal crosstalk among thermal tuners is performed as described in [75] and in Chp.3 to improve the convergence time and accuracy of the automated tuning algorithm.

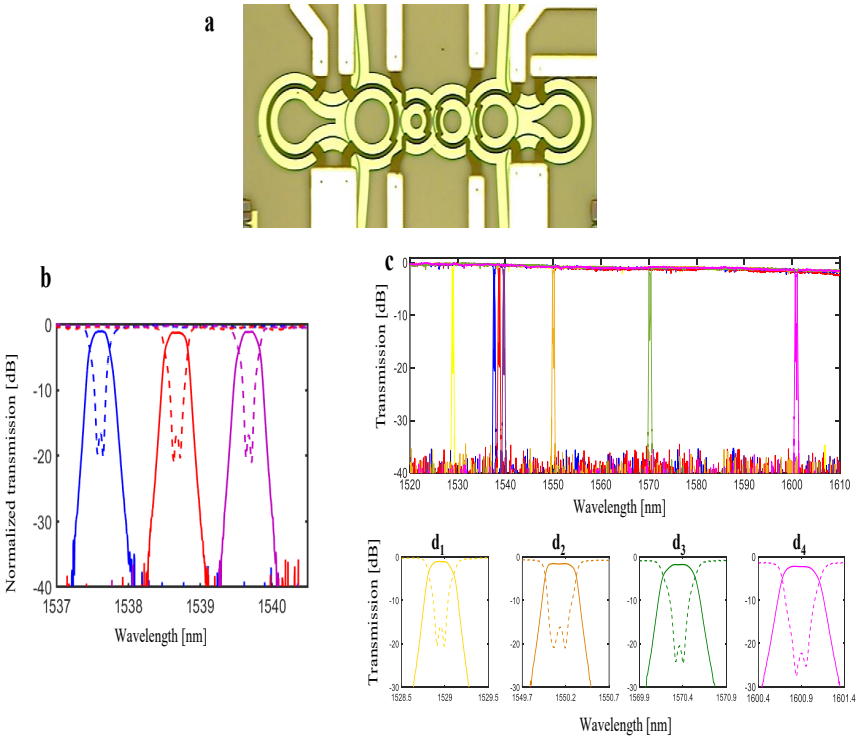

Figure 5.5: *(a) microscopic picture of fabricated device: optical waveguides, electrodes, heaters and vias are clearly visible; (b) Drop (solid) and Through (dashed) port transfer function of the filter tuned at 3 channels 100 GHz spaced, demonstrating more than 40 GHz of bandwidth with 20 dB of rejection at the 50 GHz spaced adjacent channel. (c) Frequency response of the filter tuned to 7 different channels across 90 nm wavelength range demonstrating FSR-free operation for all the channels.*

5.2.4 Experimental evaluation

Figure 5.5(a) shows a microphotograph of a 4 MRR filter fabricated on a 220-nm commercial silicon platform [57]. The rib-shaped waveguide has a width of 500 nm and a 90-nm thick lateral slab. Figure 5.5.(b) shows the measured frequency response of the filter at three wavelengths around 1538 nm. The Drop port response exhibits a 3 dB bandwidth of about 41 GHz, with less than 1 dB in-band loss and about 0.5 dB in-band ripple (evaluated across a 25 GHz pass-band). Off-band isolation is 22 dB at 30 GHz from the center of the passband and more than 40 dB at 50 GHz. At the Through port, in-band isolation averaged across 20 GHz around the center of the passband is 17.2dB.

Figure 5.5.(c) shows seven selected tuning states of the filter across the maximum wavelength range observable with our measurement equipment (90 nm). Results prove that the filter exhibits a FSR-free behavior with no evidence of periodicity. Details of the passband at selected wavelengths are shown in Figs. 5.5(d1-d4). Due to the wavelength dispersion of the coupling coefficients K, the filter bandwidth increases from 37 GHz @1528.9 nm (d1) to 53 GHz @ 1600.9 nm (d4), but maintains good performance in terms of in-band Drop-port insertion loss (< 1 dB) and Through port in band isolation (> 16 dB). Off-band transmission peaks at the Drop port are rejected by more than 33 dB over the entire span, while at the Through port only tiny notches (< 1.2 dB deep) sporadically appear that are originated by the cavity-enhanced round-trip loss of the first MRR of the filter (< 0.03 dB).

5.3 Loss-Mediated Hitless tuning

As explained in the introduction of this chapter, reconfiguration of PIC in presence of WDM grid should be done in transparent manner not to degrade the performance of other channels. In proposed techniques [88, 89, 97], Hitless operation is achieved by either using tunable coupler detuning approach or selective detuning which pushes one or more resonators in the coupled structure out of resonance condition. First approach requires addition of two MZ based tunable couplers at the input and output ports. Due to geometrical constraints, the two arms of the MZI implementing the tunable coupler cannot have the same length; the tunable coupler can be conveniently designed to have a FSR equal to the one of the MRR. Given this constraint, the tuning of the tunable coupler during the tuning

of the filter must be done simultaneously with the tuning of the MRRs. The hitless operation consists of inducing an unbalance in the two MZI that realize the tunable couplers to isolate the ring flter. In this way, all the light entering in the In port is directed to the Out port. Also, the other ports (Add and Drop) are disconnected and the hitless tuning is achieved. Selective detuning, as the second option, suggests making selective changes in each one of the resonances of the rings. If one can tune first the middle rings in the MRR structure, it is expected that the frequency shift will not affect the neighbor channels.

Unfortunately, both of these techniques introduce spurious notches and peaks along the hitless process for the Vernier based filters. Here we suggest to implement hitless tuning by literally killing the optical power inside the resonators and we believe this can be done through implementation of VOAs inside resonators. in this section we exploit this idea and analyze its performance for Vernier based filter.

5.3.1 Variable optical attenuator inside the resonators

Hitless tuning of the filter exploits controllable loss induced through VOAs integrated in the waveguide of the MRRs in addition to the thermal tuner, as shown Figure 5.6.(a). The VOA waveguide section is realized by p-doping ($10^{20} cm^{-3}$) and n-doping ($10^{20} cm^{-3}$) the lateral slab at a distance of 900 nm from the waveguide core in order to introduce negligible additional round-trip loss when no voltage is applied to the p-i-n junction. By forward biasing the VOA, free carriers are injected in the waveguide core and the associated cavity-enhanced loss is exploited to inhibit transmission up to complete disconnection of the filter. Injection of free carriers in silicon MRR filters, driven by either optical [98] and electrical [99] control, was successfully exploited to realize fast optical switches, but it has never applied to hitless tuning of a filter. It is worth pointing out that hitless filter disconnection cannot be operated by increasing the loss of the first MRR of the filter, because this will make the resonator pass through the critical coupling condition, resulting in apearance of deep off-band notches in the Through port along the hitless operation. Quantitatively, for the architecture reported in Fig. 5.2 numerical simulations indicate that a round-loss increase by only 1.2 dB in the two inner MRRs is sufficient to introduce more than 20 dB of transmission suppression, achievable with a very low current injection.

Figure 5.2.(b) shows a top-view photograph of a FSR-free filter with integrated VOAs. All the design parameters of the filter (K_i, R_i) are the

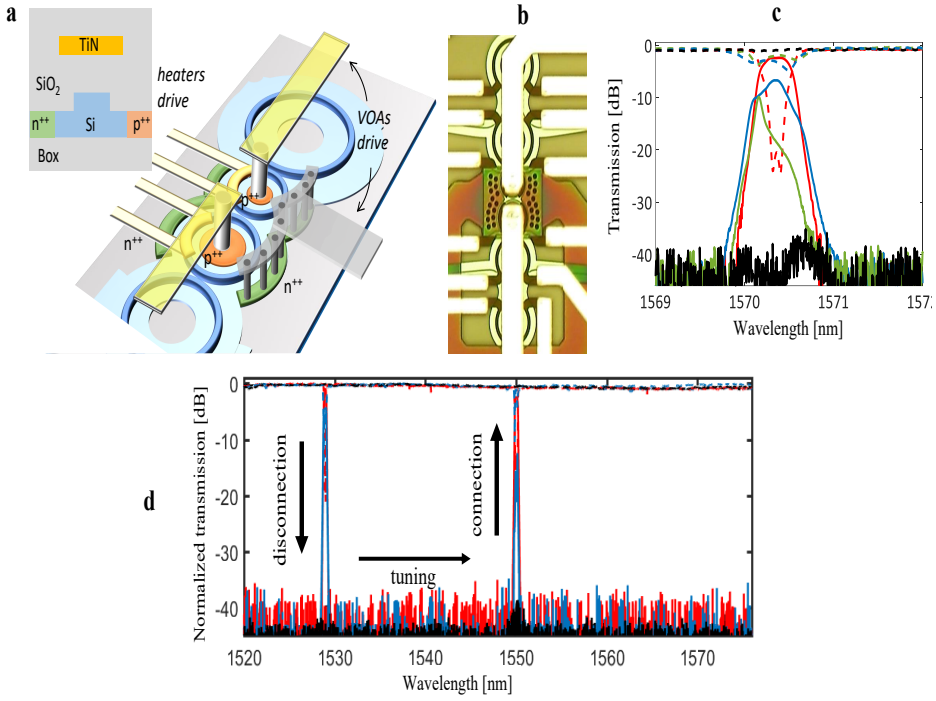

Figure 5.6: *Scheme of a single MRR with integrated p-i-n junction acting as VOA, beside the integrated thermal actuator. The rib-waveguide cross section with the TiN heater and the doped regions are shown. (b) microscopic picture of the central section of the silicon photonic filter with integrated VOAs. (d) Measured spectral response of the filter Through and Drop ports during the hitless operation at 1570.4 nm for different VOAs driving voltages: connected state (0 V, red), complete disconnected state (1.3 V, black), intermediate states (0.9 V, blue; 1V, green). (d) Hitless reconfiguration of the filter from channel 60 (1529.55nm) to channel 34 (1550.12nm) performed without introducing perturbation to WDM channels in between.*

same as in the device of Sec. 5.2.2. The forward-bias voltage driving the VOAs is applied to the p-doped regions inside the resonators through two independent metal electrodes. The n-doped regions lie at the outer side of the MRRs waveguide and are grounded to the same electrical line. The two identical VOAs have an active length of 30 μm (covering each about 60% of the MRR circumference) and introduce up to 1.4 dB additional round trip loss when fed with a driving current of 11 mA. A TiN heater 700nm above the core guarantee both the MRR tuning and the thermal compensation of the VOA during the hitless operation.

The concept of loss-mediated filter disconnection is experimentally demonstrated in Figure 5.2.(c). In the initial configuration, both VOAs are in the

transparent state (no voltage applied) and the filter passband is tuned at 1570.35 nm (red curves). From this condition an increasing forward-bias voltage of 0.9 V (0.13 dB round-trip loss, blue-dashed curves), 1 V (0.18 dB loss, green-solid) and 1.3 V (0.5 dB loss, black curves) is applied to both VOAs. At the end of the process, the filter passband is almost completely suppressed, with more than 35 dB isolation at the Drop port and less than 0.3 dB ripple at the Through port.

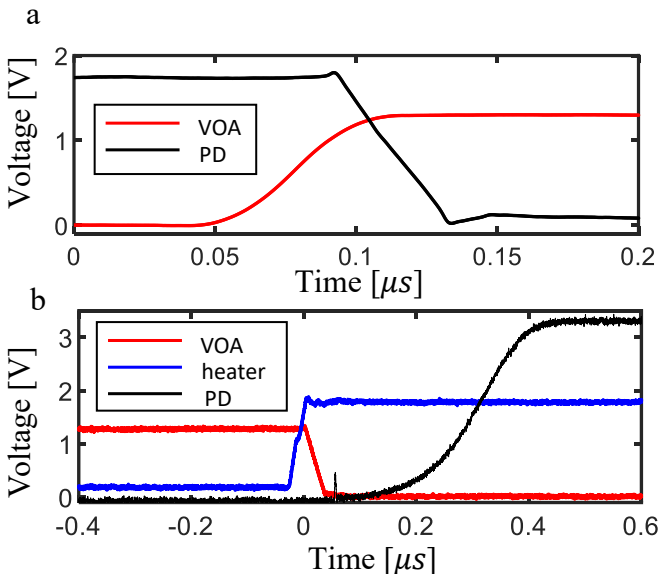

Figure 5.7: *(a) Time response of VOA turning-on process (filter disconnection) and (b) tuning-off, improved by heater thermal compensation. PD=photodetector connected at the output ports.*

Hitless wavelength selection is demonstrated in Figure 5.2.(d) showing an example of filter tuning from a 1529 nm to 1570.35 nm. Filter disconnection can be operated very fast, thanks to the ns-timescale response of carrier-injection in the VOAs. In our device, where the VOA design was not actually optimized for fast response, we achieved a VOA turn-on time ("filter disconnection") of about 40 ns (see Fig. 5.7.(a)), as measured by the power suppression at a photodiode coupled to the Drop port (black curve). Once the filter is disconnected from the bus waveguide, the final wavelength (1550 nm) can be selected by driving the MRRs heaters according to a pre-calibrated look-up table [96]. High isolation enables to perform the MRR resonance detuning with no effects on the Through port transmission of the filter across the entire wavelength range (1520 nm – 1580 nm). Back-connection of the filter to the bus waveguide is a critical

process because carrier-injection in the VOA action is also associated with plasma-dispersion [49] and thermal effects [100] , modifying the refractive index of the MRR waveguide. The resonance spread due these side-effects can be thermally counteracted by means of the integrated thermal tuners. In order to do that, the VOA turning off ("filter connection") needs to be conducted at a slower speed in order to match the higher time response of thermal tuners (tens of microseconds). As shown in Fig. 5.7.(b), by synchronizing the driving voltage signals of the thermal tuner (blue curve) and of VOA (red curve), the overall time response of the connection process can be as fast as 400 ns (black curve), that is more than one order magnitude less than the heater time response (see Sec. 5.3.2).

5.3.2 Time response of the hitless operation

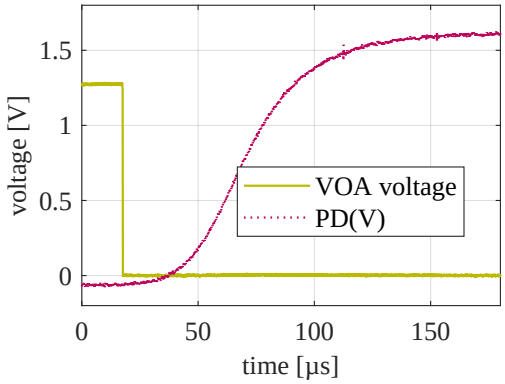

Figure 5.8: *Optical power at the output of the devices being turned ON (reconnected, turning off the VOA) demonstrates about 100μs of delay due to the time response of the thermal system.*

Implementing VOA inside MRR we can achieve perturbation free hitless disconnection of Vernier based coupled MRR filter with fast time response thanks to the fast mobility of the carriers in the junction. Observing the turning-on of the VOA inside a single MRR in Figure 5.7.a (disconnecting the MRR) we can see almost delay less response from the device to the applied signal. Cooling down of the MRR VOA following the switching-off the VOA itself is the most limiting factor in a correct hitless tuning mechanism. Figure 5.8 reports about 100us of delay to optically reconnect the MRR back, due to the time response of the thermal system dissipating the

buildup heat inside the VOA. To overcome this problem, we suggest using the integrated themro-optic actuators to cool down the MRR during the disconnection process. This should help speeding up the process by moving the system closer to the equilibrium point via compensating the heat generated inside the VOA. The suggested hitless disconnection process is described as bellow:

1. Disconnecting the device by turning on the integrated VOA;
2. Apply the new setpoint to the thermo-optic actuators to modify the optical device for the new configuration;
3. Add a cooling down bias to the voltage applied to the thermo-optic actuators to compensate for heat generated by the VOA;
4. Connect the device by turning off the integrated VOA and removing the Cooling down bias applied to thermo optical actuators;

Cooling bias is not introducing any optical perturbations since the MRR is optically lossy and disconnected form the device. In Figure 5.7.(b) we demonstrate an example of turn-off compensation based on this idea bringing the time response as low as 400 nsec from hundred microsecond. This time response can be improved by more careful choice of the cooling down bias or introducing appropriate lag between two electrical commands for heater and VOA.

5.4 Polarization independent add/drop filter

SiP waveguides and devices characteristics strongly depend on polarization and hence the two input orthogonal polarizations have to be treated separately. Polarization insensitivity is achieved by using the polarization diversity scheme of Fig. 5.9.(a). A PSR (building block from foundry [57]) splits the incoming signal in its two orthogonal polarizations (TE and TM) and rotates the TM polarization in order have only TE mode propagating in all the waveguides of the circuit. Two nominally identical filters are employed that are designed to work on the same (TE) polarization state [87]. To finely compensate for unequal loss in the two paths, a p-i-n VOA is integrated in both arms of the polarization diversity scheme. At the output, a PRC is used to rotate from TE to TM the mode that was not rotated before, and to combine the two orthogonal modes at the output.

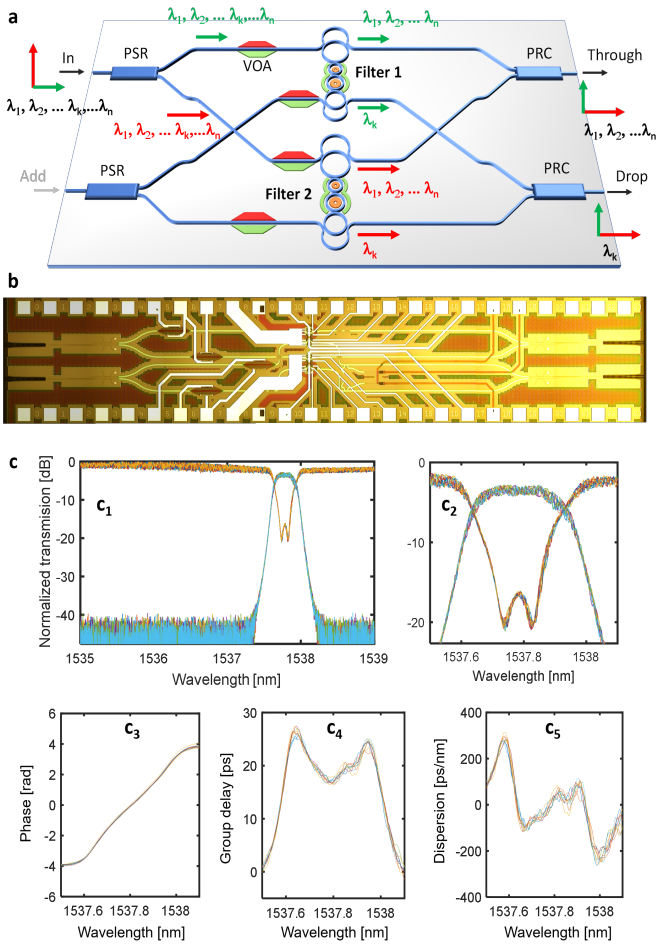

Figure 5.9: *(a) Balanced polarization diversity scheme of the polarization independent Add-Drop filter. Both filters operate on the TE mode, VOAs are used for tuning and calibration; (b) Top view microphotograph of the whole filter; (c1) Drop and Through ports spectral response measured with a polarization scrambler at the input. Each point of the curves is a different polarization. (c2) is a detail of the bandpass region highlighting the extremely low polarization dependence. (d1, d2) Filter spectral response in case of only the upper filter 1 tuned and in (d3, d4) with only the lower filter 2 tuned, leaving the other filter in the native state.*

Figure 5.9.(b) shows a photograph of the polarization diversity filter. Polarization independence was demonstrated by scrambling the polarization state of the light at the input of the device during the wavelength sweep. Figure 5.9.(c) shows ten independent measurements of the filter spectral response, where the polarization state is randomly changed dur-

ing data acquisition with a wavelength step of 1 pm (every point in each trace corresponds to a random polarization state). Results demonstrate that, when both filters are tuned, the polarization dependence of the filter is extremely small. Off-band rejection at the Drop port is higher than 40 dB and no notches appear in the Through port transmission Fig.5.9.(c1). Likewise, for the in-band behavior or the filter Fig.5.9.(c2), in-band isolation remains higher than 17 dB, with less than 1.6 dB variation in the Drop port transmission. These power fluctuations are partially due to the experimental setup, which introduces a PDL of about 0.4 dB, so that the filter PDL is ultimately 1.2 dB. Panels c3-c5 show that, when the input polarization state is scrambled, the spread of the phase response (< 0.05 rad std), of the group delay (< 1 ps) and of the dispersion (< 20 ps/nm std) at the Drop port of the filter is extremely low, thus confirming an almost polarization independent response of the filter architecture. Moreover, since the two filters have a very similar group delay characteristic and the scheme of Fig.5.9.(a) is geometrically balanced, polarization mode dispersion is negligible as well.

The VOAs introduced in the polarization diversity scheme are also used in the calibration phase to suppress one polarization and facilitate the tuning of the filter working on the orthogonal polarization. Its worth mentioning, in the Drop port of each filter, through a 10% coupler a photo detector is implemented, this detector is used during the operation to control and maintain the frequency responce of each filder operating on different polarizations. The phase response of Fig. 5.9.c3 is achieved by applying Hilbert transform [101] to the frequency domain transmission curves of Fig.5.9.c2, while the group delay (c4) and dispersion (c5) are derived by subsequent differentiation versus frequency.

Polarization transparency of this device is evaluated by analyzing its perturbation on a 100 Gbit/s Pol-Div QPSK channel quality through BER measurement. Starting from the back to back (B2B) evaluation which replaces the device by an optical fiber, BER of this channel is recorded versus its Optical Signal to Noise Ratio (OSNR) in black curve of Fig.5.10(a). Reconnecting the PIC, polarization transparency of this device is examined by detuning the filters from the channel wavelength to evaluate the penalty of the polarization diversity scheme including PSR, PRC, suspended couplers and optical circuitry on the channel. Overlap of the blue curve in Fig.5.10(a) on the black one demonstrates zero penalty due to transmission of the channel through the device from the In port to the Through. Tuning the filters to the channel, BER is measured at the Drop port. Yellow curve

in Fig.5.10(a) demonstrates improvements of the channel performance due to filtering of the out-band noise and reshaping the channel via filter.

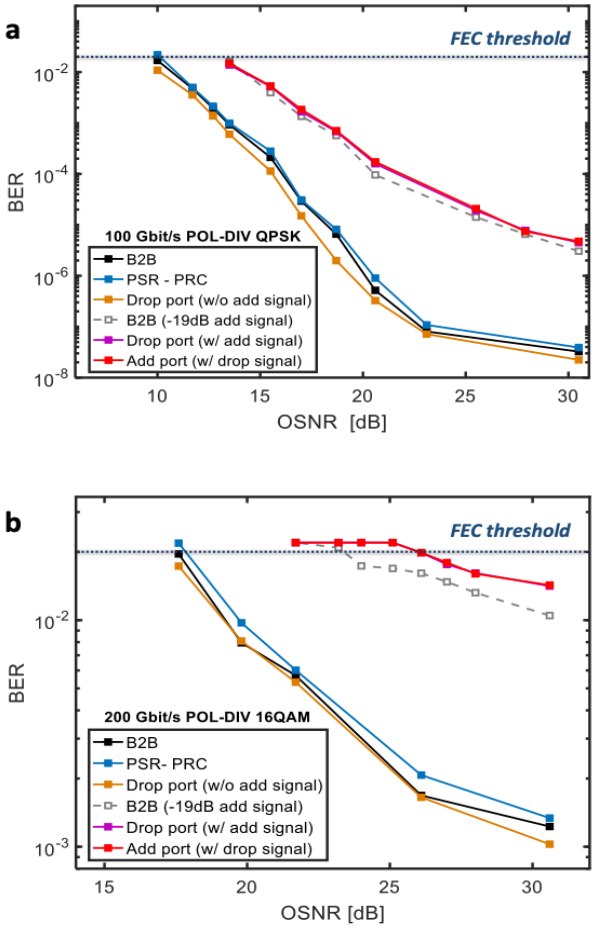

Figure 5.10: *BER versus OSNR of (a) 100 Gbit/s Pol-Div QPSK channel (b) 200 Gbit/s Pol-Div 16QAM channel. Black curve for back to back scenario replacing the device with a direct fiber in the setup, Blue curve for connected device while the filters were detuned from the channel to measure the transparency of Pol-Div scheme, Yellow curve for dropped channel. Red and Pink curves are for adding and dropping of two channels at the same wavelength with the same modulation scheme being launched at In and ADD port. Dashed-Black curve is the performance of the transceiver for B2B condition when two channels are coupled by a fiber coupler and one (the perturbing channel) is 19 dB below the measuring one.*

This device is capable of replacing a Pol-Div channel on the DWDM

grid, in other words, two channels with the same wavelength and the same modulation schemes can be simultaneously dropped and added to the grid. To evaluate the performance of the device in this scenario, two 100 Gbit/s double polarization QPSK channels are launched into this device, one at the In port, one at the ADD. BER of the dropped channel at the Drop port and added one in the Through port is recorded and presented in Fig.5.10(a) in pink and red curves, respectively. Same penalty is recorded for both of these channels, meaning same perturbation is introduced by the filters to both of them. To understand the nature of this penalty we disconnect the device from the setup (B2B) and using a fiber coupler we combined these two channels together while measuring their BER. Dashed-black curve in Fig.5.10(a) shows the condition when the perturbing channel is 19 dB weaker than the channel under study. Considering our device is measured to introduce 18 dB of in-band isolation, its penalty on the added or dropped channel is in line and can be improved by designing the device to have more in-band isolation if is necessary. In all of above mentioned scenarios we are below the FEC limit of the transceiver, meaning all the penalties due to the device perturbation is compensated leading to an error free transmission. These analysis are expanded to 200 Gbit/s Pol-Div 16 QAM channel in Fig.5.10(b). Having a limited dynamic range in BER versus OSNR comparing to 100Gbit channel, the recorded results are in line with previous trials and demonstrates polarization transparency even in presence of this complex modulation scheme.

5.5 Summary

In this chapter, we demonstrated that a functionality strongly craved for years, that is an integrated polarization-independent filter with ultra-wideband hitless tuneability, is nowadays realistic and fully compliant with current and future technologies for core networks and the emerging 5G back-haul networks and datacenter interconnects. Advantageously, the enabling innovation is not a specific technology process, since the device was fabricated in a commercial silicon foundry. We exploited instead new strategies for the design, calibration, tuning and control of the photonic integrated circuit, which can be ported to other circuits and optical functionalities. We expect that, beyond the high performance of the presented device for specific applications, these results may contribute to change the perception of what can be done now with integrated photonics, opening the door to new ultracompact, low cost, low-power consumption, fully reconfigurable and programmable photonic devices.

In particular, we report on a fully-reconfigurable add-drop silicon photonic filter, which can be tuned well beyond the extended C-band (almost 100 nm) in a complete hitless (>35 dB channel isolation) and polarization transparent (1.2 dB polarization dependent loss) way. This achievement is the result of blended strategies applied to the design, calibration, tuning and control of the device. Transmission quality assessment on dual polarization 100 Gbit/s (QPSK) and 200 Gbit/s (16-QAM) signals demonstrate the suitability for dynamic bandwidth allocation in core networks, back-haul networks, intra- and inter-datacenter interconnects.

CHAPTER 6

Free space beam manipulation

PIC consisting of generic programmable architectures that can be reconfigured during operation are emerging as a promising approach for advanced processing of optical signals. Examples of programmable PICs and optical processors have been recently proposed in different application fields, including microwave photonics [102], mode manipulation in telecommunications [103], quantum [104] and neural networks [21]. SiP is a promising photonic platform for the realization of large scale integration of photonic processors, not only because of the high degree of device miniaturization, but also because of the possibility to integrate fast and power-efficient tuning elements and on-chip monitor photodetectors, which are necessary for robust reconfiguration and control of the photonic architecture. Recently, we demonstrated that a SiP mesh of MZIs can self-configure to perform automatic reconstruction and unscrambling of guided modes which have been strongly mixed during the transmission through a multimode waveguide. In this thesis, we demonstrate that the same architecture can be effectively used to manipulate free-space optical beams. We discuss the performance of control algorithms for these structures and analyze some ideas to improve the performance of tuning and calibration techniques. A number of optical functions are implemented,

including beam steering, beaming back to the source, and identification and coupling of a free space beam coming from an arbitrary direction. At the end we demonstrate beam manipulation and beam front correction, achievable with this circuits implemented with appropriate control strategies.

6.1 Mach Zehnder meshes

Photonic integrated meshes made of tuneable interferometers enable us to implement functions programmable on demand and are being envisioned as the optical counterpart of electronic field programmable gate arrays. Several examples of photonics processors capable of performing arbitrary linear operations have been recently proposed, and are expected to find applications in different areas, from the on-chip processing of telecom signals to microwave photonics, and from quantum optics to neural networks. In this thesis, we use a reconfigurable mesh of silicon photonic MZIs to manipulate free-space optical beams. Among the variety of functionalities that can be implemented, we demonstrate beam steering, beam coupling from a free space optical source to a single mode waveguide and automatic identification of the direction of arrival of a beam from a free space source. For further detail about these structures refer to Appendix B.

Two major configurations of mesh circuits are known based on the arrangement of the MZI appropriate for different applications:

(i) **Binary Mesh** Figure 6.1 shows the schematic of a mesh of MZI in the binary (tree), topology. The control algorithm, as we discuss in detail in Sec 6.2, relies on the minimization of one branch, in which typically there will be the monitoring sensor, to direct all the light in the other one. Light inside the MZI goes through coherent interaction implying that the relative phase between the branches has to be carefully set.

In order to obtain a correct tuning of the structure, since we are dealing with interferometric devices, it is important that the optical modes, before entering in the MZI block, have experienced the same optical path. In this topology of mesh, this condition is guaranteed thanks to the symmetry of the structure meaning that no optical path compensation is needed.

Tuning process requires coherent comparison of modes in each two inputs through a stage of MZI and maximum (combination of two

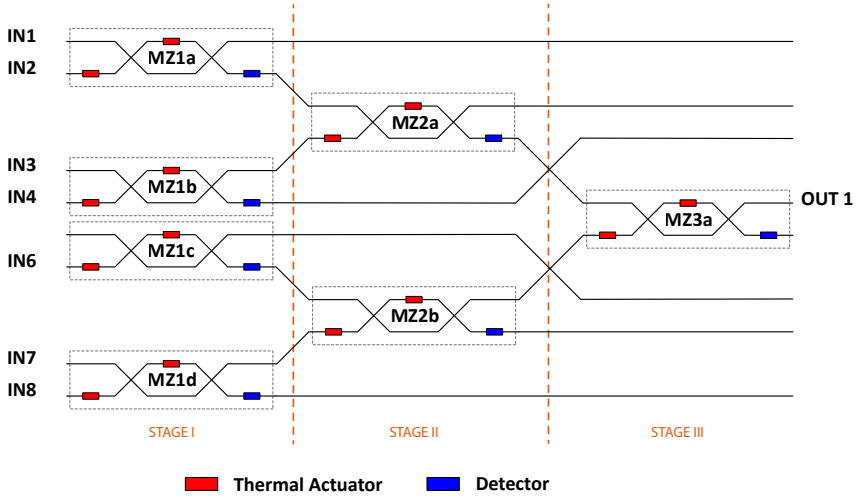

Figure 6.1: *Three stage binary Mesh with 8 inputs and one output*

modes) is fed into one output of the MZI which means minimization of the other port that is actually used in the controller as merit. In this topology of the mesh all the input pairs can be tuned at the same time (stage.I in Fig. 6.1) and their outputs in parallel too till we reach the single output in the last stage (stage.III in Fig. 6.1). For the case of mesh in Fig. 6.1 3 instance of tuning is needed. In the binary mesh the number of MZI available is equal to the total number of input available per stage divided by 2. Therefore the total number of stages is equal to the $log_2(N)$, with N number of total input.

However the binary mesh has some disadvantages. The main important drawback is the number of outputs per inputs available which is one output for N number of inputs with the possibility of handling only one mode. One last important disadvantage of this topology is the inevitable presence of crossing points in wave guide routing which has to be carefully designed and limited if possible to avoid optical cross talk between stages (see Sec. 2.5.2 for details on crossings).

(ii) **Diagonal Mesh**

Figure 6.2 shows the scheme of a mesh of MZI in the diagonal topology. First of all, in diagonal mesh, equal geometrical path length is not guaranteed due to the lack of symmetry. Looking at Fig.6.2 output of stage.I is one of the inputs for stage.II and since optical mode has experience the curvature of wave guides building the MZI of stage.I,

two paths do not have the same length and there is the need for compensation. This should be done carefully along the mask design process.

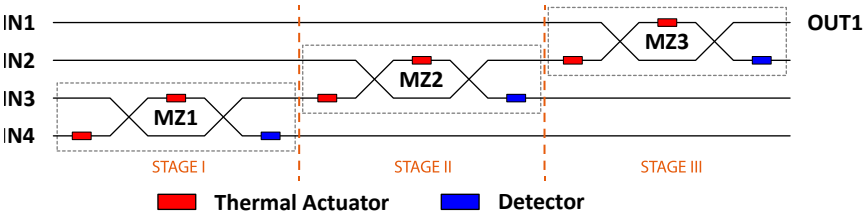

Figure 6.2: *Three stage binary Mesh with 8 inputs and one output*

Tuning this mesh topology requires each single MZI of a stage to wait for tuning of the previous stage and it doesn't allow for parallel tuning of MZIs. Therefore the total number of stage to tune is equal to N-1, with N number of total input.

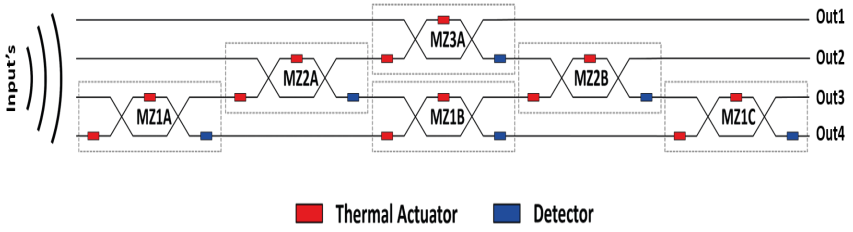

Figure 6.3: *Schematic of a triangular with 'four' possible outputs for four inputs implemented through 3 series triangular meshes.*

Even though these limitations and constraints, diagonal mesh has some interesting advantages. Due to the nature of this topology there is no need for wave guide crossings in implementation of the mesh, simplifying the optical circuits and reducing the optical loss for large scale meshes. More importantly, in case we implement sub-diagonals as shown in fig.6.3, there is access to larger number of outputs. In other words, we can handle N_D number of optical modes with this structure without the need for wave guide crossings which other than loss can introduce mode cross talk.

6.2 Self-adjusting building block

We study different approaches to implement parallel feedback loops steering and holding the MZI tunable couplers of a mesh to the desired working point. More specifically, we considered a 4x1 silicon mesh made of three cascaded MZIs, according to the architecture of Fig. 6.4, and we compared the performance of automatically controlling this structure by using two different approaches:

(i) A single off-chip photodetector coupled at the output port of the mesh (Fig. 6.4.a)

(ii) Multiple on-chip monitors integrated at the output ports of each MZI (Fig. 6.4.b).

In this experiment, four optical beams at the same wavelength of 1550 nm are provided at the four input ports IN1- IN4 and the mesh has to be automatically configured in order to have the four beam coherently summed up at output port OUT1. The same dithering-based (see Sec. 4.1.2 for details on dithering) control strategy is used for the two tuning approaches.

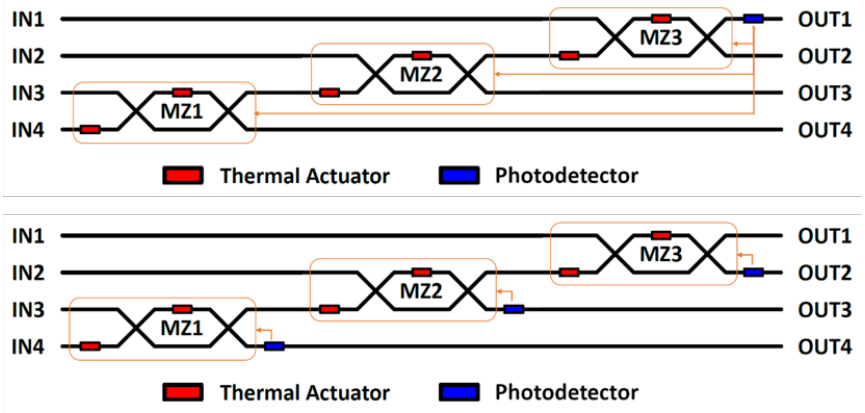

Figure 6.4: *(a) MZI mesh with single off-chip photodetector (photodiode) on the last output waveguide. (b) MZI mesh with on-chip transparent photodetectors (CLIPPs) at each MZI output.*

The main difference between the two approaches is that the scheme with only a single photodetector (Fig. 6.4.(a) requires the use of a different dithering frequency for each thermal actuator of the mesh, resulting in 6 different dithering in total. This is necessary to enable the control system to distinguish the contributions of the different actuators, but represents an obstacle for the scalability of this kind of approach. In contrast,

the structure in Fig. 6.4.(b) with a photodetector for each MZI requires instead only two different dithering frequencies, to distinguish the contributions of the two heaters in the single MZI. The same two frequencies can be advantageously re-used in subsequent MZIs. In fact, when a MZI is locked on a maximum or a minimum of the optical power, the dithering signal at its output is minimized and does not affect other interferometers.

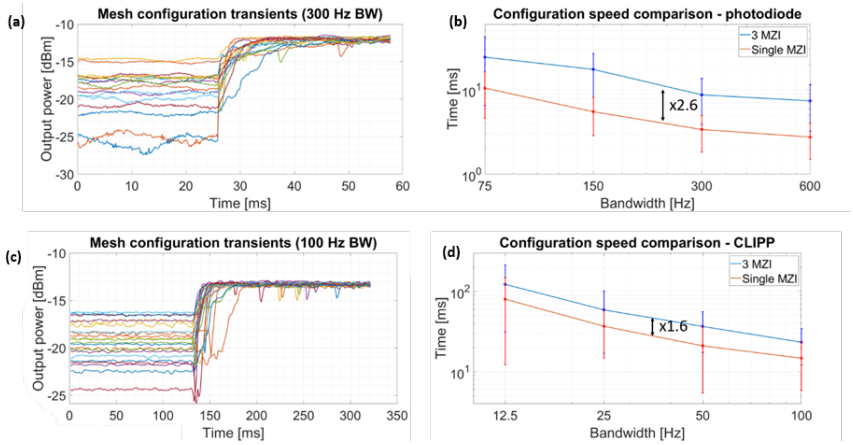

Figure 6.5: *(a,c) Transient responses and (b,d) comparison between the configuration time of a single MZI and a cascade of three, for different bandwidths of the control system. Measures are referred to a MZI mesh with single off-chip photodetector (photodiode) on the last output waveguide and a MZI mesh with on-chip transparent photodetectors (CLIPPs) at each MZI output, respectively.*

The performances of the two approaches were evaluated by activating the two different control systems starting from number of different initial mesh configurations, where the 6 heaters of the mesh are randomly set within their range of operation. From this condition the automated tuning scheme is activated, which evaluates the partial derivatives of the power measured at the detector(s) versus the phase shift provided by the heaters, searches for the minimum power (or maximum depending on the approach) at the detectors (in order to maximize the output port OUT1) and finally keeps heaters locked to the desired working point through an integral controller. Figure 6.5 shows the measured transient responses, from the random starting points to the desired settling point. In this experiment, all the dithering signals had a 50mV amplitude, while the selected frequencies were 6 kHz and 10 kHz for the experiment with detectors (CLIPPs) at each stage (scenario i) and 6 kHz, 8 kHz and 10 kHz (phase and quadrature) for the experiment with the single photodiode (scenario

ii). The main difference between the two approaches is about the scaling of the configuration time versus the number of cascaded MZIs. In fact, when a single photodetector is employed, an almost linear dependence is observed (2.6x configuration time for 3 MZIs with respect to a single MZI). In contrast, when multiple photodetectors are used, the configuration time scaling is clearly sub-linear. This result can be justified by observing that in the latter case the configuration of the three MZIs may run in parallel (at least partially) and the subsequent MZIs can start approaching the optimum biasing point even though convergence in the previous MZIs is not completely achieved. Therefore, using integrated photodetectors to realize local feedback loops appears as a viable strategy to speed up the configuration time of meshed scaled up to a large number of MZIs.

6.2.1 Phase sensitivity and accuracy of MZI elementary cells

The MZI elementary cell of the mesh circuit must be designed to behave as close as possible to an ideal tuneable coupler. To this aim, the two directional couplers of the MZI should be as close as possible to 50% split ratio (3dB condition) and the phase shifters should provide at least a 2πshift. Moreover, in order to finely tune the MZI bias point, high accuracy is required in the electronic system driving the phase shifters, that in the fabricated silicon mesh are implemented though thermal tuners (heaters see Sec. 2.3.1).

The phase sensitivity of the MZI cells was investigated in order to identify the requirements (voltage resolution) of the electronics used for the control of MZI meshes. To this aim we considered the SiP MZI of Fig. 6.6(a) with a thermal tuner integrated in each wave guide. The 3dB directional coupler consists of two coupled channel waveguides (500 nm x 220 nm core, 40 μm long waveguides) spaced by 300 nm from each other. TiN heaters with size 2μm x 80μm, placed 1 μm above the wave guide, were used as thermal tuners. The frequency response of this device, shown in Figs 6.6(b)-(c) confirms almost balanced configuration of MZI since the natural response (heaters off, red curve) is close to cross condition. By thermally controlling the phase unbalance, we show maximum isolation at the bar port (π phase shift – light green, 3π phase shift – dark green) and maximum isolation at the cross port (2π phase shift – light green), both exceeding 25 dB around 1558 nm. The wavelength dependence of the isolation at the base port is due to the wavelength dependence of the directional couplers. The electrical power required to introduce a π shift is about 15.5 mW, in line with typical values of thermal tuners in SiP waveg-

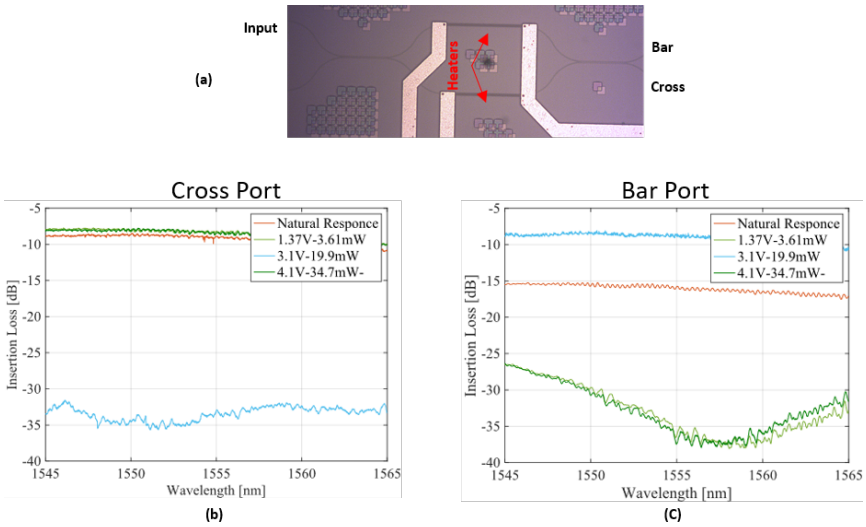

Figure 6.6: *(a) Microscopic picture of a silicon MZI cell including the electrical routing feeding the implemented heaters. Performance of MZI in its Cross port (b) and Bar port (c) demonstrate more than 25dB isolation in both states.*

uides. From these calibration curves we derived that 0.001 π resolution in the phase control of the MZI requires 1mV of resolution in the voltage driving the heaters.

6.2.2 Accuracy of meshes to extract phase information

We tested the accuracy that we can achieve when an MZI mesh is used to measure the phase difference between input optical beams. Conceptually, we intentionally introduce phase perturbations in the input beams of a mesh and we exploit the automatic control of the MZI to compensate against these perturbations. The compensating voltage stabilizing the MZI to the target working point provide information on the relative phase shift between the input beams.

In the reported experiment, we used a 4x1 triangular mesh of SiP MZIs and we controlled the phase different between the input beams by using the phase actuators integrated at the four input ports of the mesh (Fig.6.7(a) present the schematic of experiment). Figure 6.7(b) shows the optical power at the output port of the mesh when a sinusoidal phase perturbation with 200mV amplitude (about $\pi/5$ phase perturbation) and 220Hz frequency is used. If the feedback loop control is switched off (t < 120ms, no compensation of the phase perturbation) pronounced sinusoidal oscillations are clearly visible in the output power. If the MZI control algo-

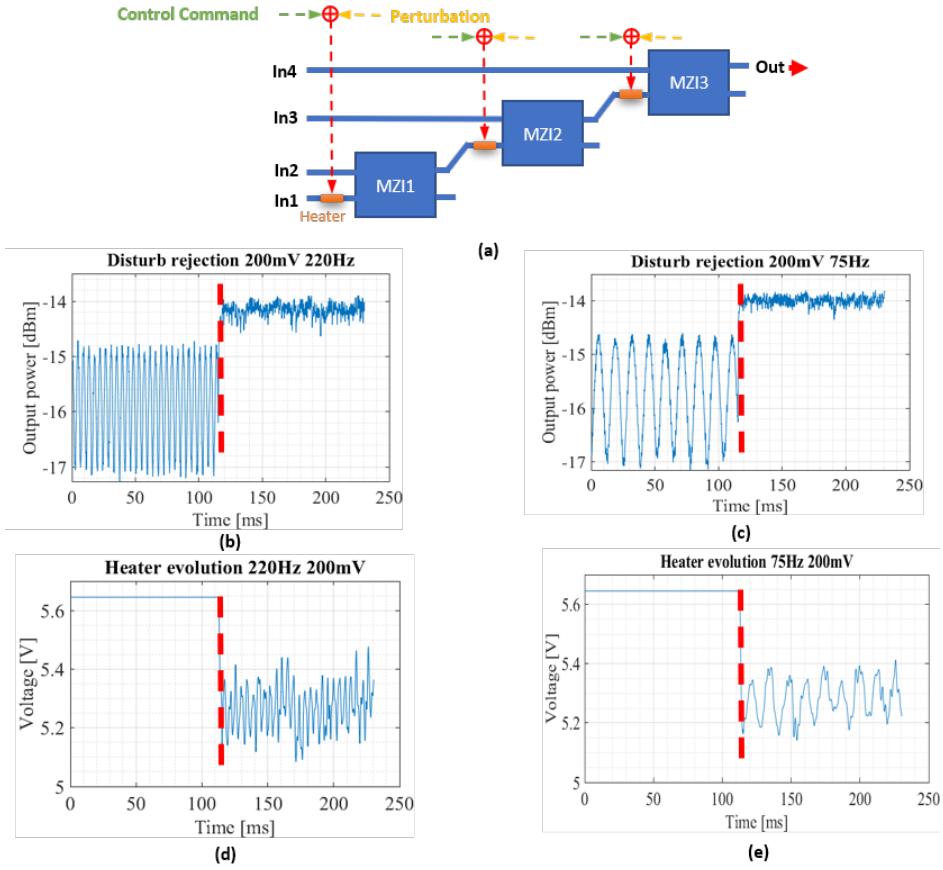

Figure 6.7: *(a) Present the schematic of experiment, introducing perturbation in phase shifters of mesh to replicate phase variation in incoming beam. (b,c) Output optical power of a triangular mesh in presence of sinusoidal perturbations in all the phase shifters, representing the possible external perturbation in the incoming beam before and after execution of the control algorithm demonstrated via the red line. (d,e) A heater evaluation after execution of control algorithm, demonstrates the appearance of the sinusoidal perturbation in heater voltage which is dictated by control algorithm.*

rithm is activated (t > 120ms), amplitude perturbations at the output port disappear. This happens because a sinusoidal voltage signal at the same frequency is imparted from the feedback control algorithm to the phase shifters (d), which is responsible for the cancellation of the intensity perturbation at the output. Figure 6.7 (c) and (e) show the same experiment carried out at a frequency of 75 Hz. The steady state error for sinusoidal perturbations with amplitude of 200mV ($\pi/5$ phase shift) is about 40 mV, corresponding to an accuracy of about $\pi/25$ in the phase compensation,

this value providing the accuracy of the MZI mesh to detect the phase difference between incoming beams.

6.3 Improving Control approaches for integrated meshes

Tuning algorithms based on local minimization loops demonstrates fast and robust control in MZI meshes (as discussed in Sec. 6.2). Large scale and dense meshes can suffer hugely from thermal cross talk presents inside MZI stages or between different stages. In Sec. 3.1.1 we demonstrated through simulations, using TED-based control algorithms we can cancel this coupling effect, obtaining a cross talk free system. In this section, we introduce a simple solution in design process of these circuits to reduce this unwanted phenomenon. This solution is compatible with commercial Si foundry platforms. Section 6.3.1 is dedicated to this concept.
In the following, we analyze the effect of these control techniques on the performance of array antennas connected to these meshes. Integrated meshes can be connected to antenna arrays to produce appropriate amplitude and phase of optical mode for each of array elements. Sections 6.4 and 6.5 discuss and demonstrate applications of these devices. In Sec. 6.3.2, through numerical simulations we distinguish the effect of control algorithms on different aspect of the free space beam and offer design solutions to reduce these effects.

6.3.1 Reduction of thermal cross-talk

In addition to the use of the TED method, we can reduce the coupling between the heaters and victim waveguides through careful design approaches without sacrificing the chip area. This coupling can be reduced by introducing deep trenches in the path of the heat flow. Deep trenches can be considered as deep holes inside the chip removing materials (silica and Silicon) between heaters and victim waveguides thus reducing the thermal flow by leaving only air in between. As shown in the Fig. 6.8(a), a trench is placed inside each MZI to limit the crosstalk (Heat Flow 1) between the two arms of the same MZI, this perturbation reducing the performance of the MZI. The trench is intentionally located closer to the "passive" (unheated) waveguide in order to avoid speed reduction on the heater response. In addition, a second deep trench is integrated outside the MZI, to prevent unwanted phase shift in the waveguides at the input of following MZI stages. In fact, this effect would result in a phase noise, which can be misinterpreted as variation of the phase of the incoming optical beam. based on these concepts a mask layout was designed and taped

out on January 2020, fabricated chips arrived prior to this thesis allowing us to capture microscopic pictures. Figure 6.8(b) presents zoomed of a MZI arm with a deep trench preventing the Heat Flow 1 while in (c) a snapshot of larger integrated mesh with suggested thermal cross-talk remedy.

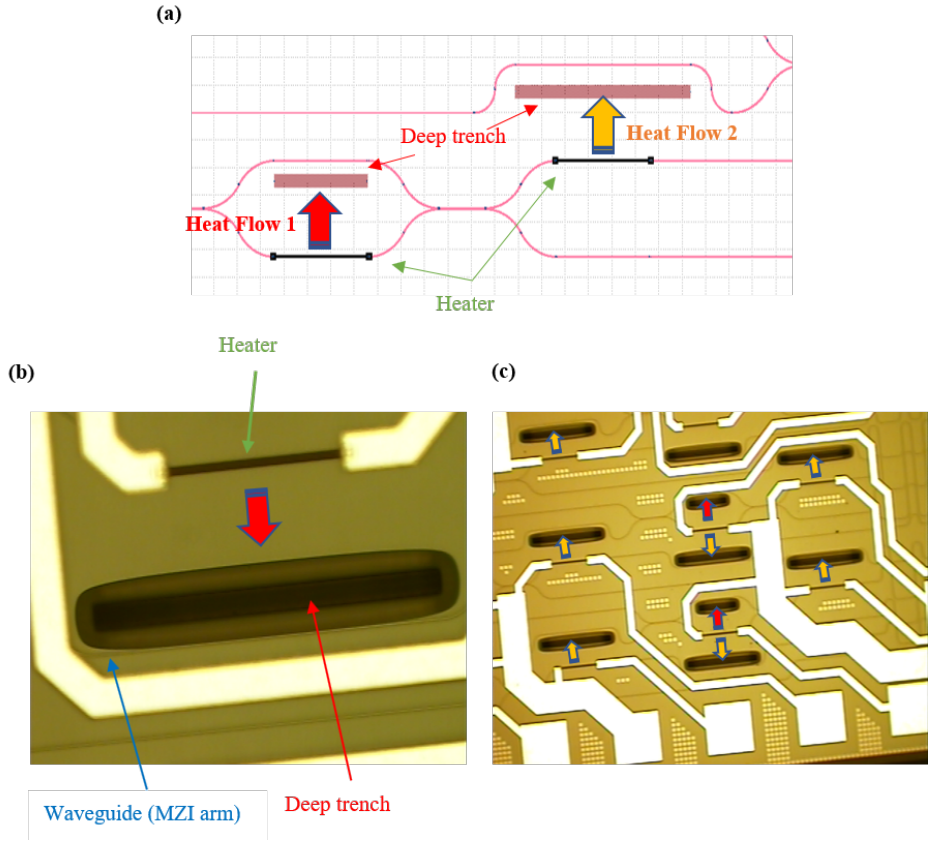

Figure 6.8: *(a) Chip layout demonstrating the use of deep trenches to prevent the thermal gradient (Heat flow) resulting from an actuated heater to change the refractive index of unwanted waveguide. Heat flow 1 is blocked to maintain the performance of the MZI by not introducing phase shift in the other arm of MZI. Heat flow 2 is blocked to prevent introduction of phase shift in neighboring waveguide which is not the desire. (b) Microscopic picture of the fabricated chip with deep trenches implemented, circuit elements and heat flow directions are marked to cross-connect with the introduced schematic of (a)*

6.3.2 Perturbations of the control system on mesh performance

As explained before (Sec. 6.2), our strategy for automatic control and stabilization of MZI elementary cells exploits the dithering of the phase actu-

ators to quantify (with no sign ambiguity) the MZI unbalance to be compensated and apply a suitable feedback control signal. Dithering inherently requires the introduction of a perturbing sinusoidal signal into the MZI phase shifters (and hence an optical modulation) and the use of the demodulated signal as the feedback. Such optical modulation results in an unwanted perturbation in the phase and amplitude of optical signal at the output port of the mesh. If the mesh is used as a beam forming network, that is to shape a free space optical beam by using the mesh output ports (grating couplers) as optical antennas, this amplitude and phase modulation is translated into perturbations of the overall radiation pattern. These perturbations can appear in the form of unwanted beam steering, variation of the directivity or degradation of side lobe rejection of the radiation pattern. Reducing the amplitude of the phase dithering reduces these side effects, but at the same time it makes the signal to noise ratio of the control system lower, thus reducing the performance in term of control speed and accuracy. To understand the sensitivity of the mesh performance to the amplitude of the dithering signals we developed a numerical simulator (Matlab [74] code) exploiting a frequency-domain transmission matrix method (TMM). The simulation tool is modular and can be used to investigate MZI meshes of arbitrary sizes and different topologies (diagonal, triangular, binary tree,...). Given an arbitrary set of optical signal provided to the input ports of the mesh, the simulator calculates the amplitudes and phases at the output ports of the mesh. These complex amplitudes are used to excite an array of point radiators positioned at an arbitrary distance from each other. The radiation pattern associated to these phased arrayed antennas is evaluated by using (Sensor Array Analyser tool in Matlab [74]) and the degradation caused by dither-induced phase perturbations can be evaluated.

For example, Fig. 6.9(a) shows the ideal radiation pattern generated by an array of 4 elements connected to a diagonal 1x4 mesh. In this example, we chose as a reference radiation pattern the case when all output fields share the same amplitude and phase (no phase difference among the four antennas), but arbitrary radiation patterns can be considered. To evaluate the effect of dithering signal, random phase perturbations distributed according to a normal pdf (around their ideal values) with standard deviation as large as $\pi/50$, $\pi/25$, $\pi/12.5$ are introduced in each phase shifter of the mesh (3 MZI, 6 phase shifters in total). For each amplitude of the phase perturbation, 2000 cases were simulated, where the frequency response of the 1x4 mesh was calculated and the associated radiation pattern was evaluated. Radiation performance was assessed in terms of 3dB beam width

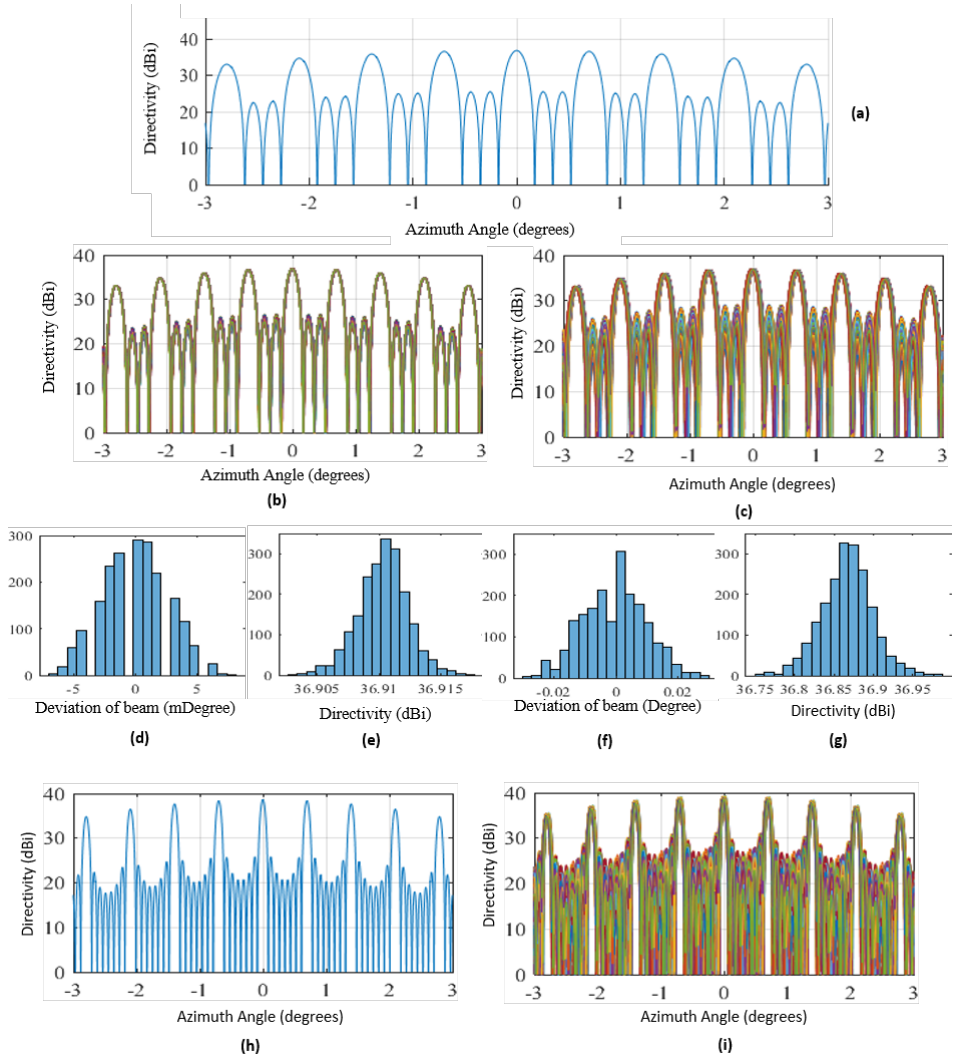

Figure 6.9: *(a) Ideal pattern of 4 element array. Radiation pattern of 2K cases with normally distributed phase perturbations in all the phase shifters of the mesh (uncorrelated) with standard deviation of $\pi/50$ (b) and $\pi/12.5$ in (c). Histogram of the deviation from the direction of max directivity (d) and directivity value (e) for $\pi/50$ and (f)-(g) for $\pi/12.5$. (h) Ideal radiation pattern of an array with 8 elements connected to a diagonal 1x8 mesh and (i) variation of the radiation pattern for 2K cases with random $\pi/12.5$ phase perturbations in the mesh actuators.*

(degree), directivity (dBi), unwanted steering from the reference beam direction (degree), and side lobe rejection (dB). These merits define the performance of free space system and dictate the max dithering signal can

be used in the system. As said before, in the developed simulation tool we can modify the size of the antenna array (mesh size), the mesh topology (binary, diagonal, triangular), the number of optical inputs, as well as the type of phase perturbations (e.g. different pdf, correlated/uncorrelated phase perturbations) and their magnitude, Fig. 6.9(h) present ideal radiation pattern of system with 8 elements and Fig. 6.9(i) effect of $\pi/12.5$ perturbation in that system. In the table 6.1 a summary of the performance of a triangular mesh with 4 and 8 elements is presented for 3 different amplitude of phase perturbations.
These studies can be expanded to different types of mesh, different configuration of radiators to understand the consequence of control on specific aspect of array. As an example we can study the deviation of the main lobe (known as steering) due to control perturbations. Simulator can be used to compare the resilience of two mesh typologies against these perturbation and for different number of radiators. Plot in Fig. 6.10 demonstrate for this example, binary mesh has better performance in this scenario while both meshes exhibits more robustness by increasing the radiators. Detailed numbers in table of Fig. 6.10 extend these analysis for both steering angle of the main lobe and its directivity.

This family of analysis allows us to decide upon both the topology and order of the meshes for different layout of radiators depending on the application needs. Based on these analysis, in January 2020 in an Multi Project Wafer (MPW) run for European project SuperPixels as demonstrator chip is designed and regarding layout is prepared.

Table 6.1: *performance of array with 4 and 8 elements for 3 different phase perturbations.*

		3dB beamwidth (degree)		Max directivity (dBi)		Steering (degree)		Side lobe rejection (dB)	
		mean	STD	mean	STD	mean	STD	mean	STD
4 element array	ideal	9.167	–	36.913	–	0	–	11.347	–
	$\pi/50$	9.15	0.064	36.91	0.002	0.004	0.149	11.338	0.381
	$\pi/25$	9.155	0.122	36.902	0.008	0.007	0.298	11.321	0.766
	$\pi/12.5$	9.187	0.249	35.867	0.032	-0.006	0.587	11.349	1.621
8 element array	ideal								
	$\pi/50$	4.511	0.038	38.596	0.031	0.001	0.038	12.786	0.399
	$\pi/25$	4.515	0.065	38.529	0.066	0.003	0.208	12.755	0.799
	$\pi/12.5$	4.526	0.126	38.577	0.158	0.004	0.415	12.606	1.538

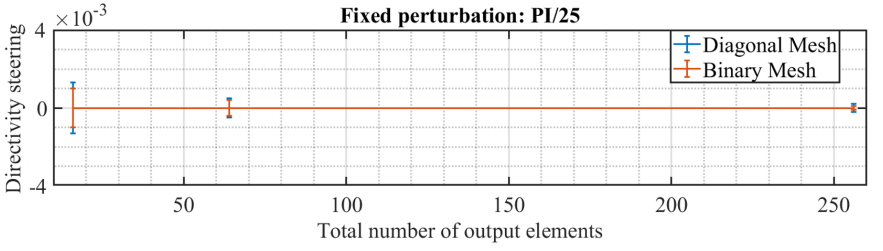

DIRECTIVITY MAX (dBi)		MEAN AND STANDARD DEVIATION EVALUTION INCREASING # OF ELEMENTS IN THE ARRAY					
PERTURBATION	TOPOLOGY:	N=16		N=64		N=256	
PI/25	BINARY MESH	38.7767	0.0258	38.8793	0.0195	38.9064	0.0201
	DIAGONAL MESH	38.8040	0.0666	39.0323	0.2472	39.6202	1.1613

DIRECTIVITY STEERING (°)		MEAN AND STANDARD DEVIATION EVALUTION INCREASING # OF ELEMENTS IN THE ARRAY					
PERTURBATION	TOPOLOGY:	N=16		N=64		N=256	
PI/25	BINARY MESH	0.0000	0.0010	0.0000	0.0004	0.0000	0.0001
	DIAGONAL MESH	0.0000	0.0013	0.0000	0.0005	0.0000	0.0002

Figure 6.10: *The mean and standard deviation of Maximum Directivity and correlate steering for binary mesh, in orange, and diagonal mesh, in blue, for different size of the array in table while Plot of these variations for steering angle in the plot.*

6.4 Processing free space optical beams

In this section, we demonstrate PIC mesh can be controlled and tuned based on the discussed techniques and tricks to manipulate and modify free space beams for different applications. Including free space coupling and tracking, source identification. In detail we study and discuss how through integrated meshes we can introduce appropriate beam fronts to correct for scattering mediums in free space channels.

6.4.1 Silicon Photonic mesh

The PIC consists of a triangular (diagonal) mesh of MZIs arranged as in the scheme of Fig. 6.11(a), which was fabricated on a standard 220 nm SiP platform by using 500 nm wide channel waveguides (see Fig. 6.11(b)). The four ports labeled as RPi consist of an array of radiating elements (grating couplers) with a mutual spacing of 127 μm to either couple a free-space optical beam into the photonic chip or to radiate a guided-wave signal out to the free space. All the balanced MZIs integrate 3 dB directional couplers with a gap of 300 nm and a length of 40 μm. Two phase shifters are integrated in each MZI by using TiN metal strips (1 μm x 100 μm) to implement amplitude- and phase-tuneable couplers. The electrical power consumption required to induce a π phase-shift is about 10 mW. The circuit bends have a curvature radius of 20 µm, reducing reflections and losses. To keep the total length of each path equal, hence equalizing the propagation losses and reducing the wavelength dependence of the response due to unbalanced paths, additional bends have been introduced in the design. At the output port of each MZI, on-chip photodetectors (here realized through CLIPP transparent detectors by using the same TiN used for thermal tuners) are used to locally monitor the switching state of each MZI and implement automatic tuning and stabilization procedures.

The SiP chip was mounted on an electronic printed circuit board (see Fig. 6.12) hosting the drivers of the thermal tuners and the electronics for the read-out of the on-chip detectors. Specifically designed to hold also two CMOS application specific integrated circuits (ASICs). These 32-channel ASICs allow high quality CLIPPs signal monitoring.

More details on the circuit design, fabrication technology and electronic circuit for the automatic control of the mesh can be found in [103]. All the experiments reported in this thesis were carried out at a wavelength of 1530 nm.

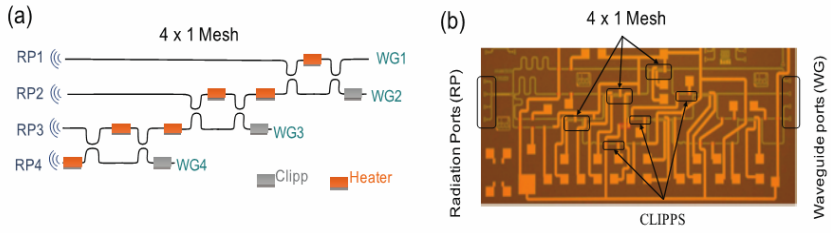

Figure 6.11: *(a) Schematic representation of a 4 x 1 triangular mesh and (b) its implementation on a conventional SiP platform. The overall footprint of the circuit is 3.7 mm by 1.5mm.*

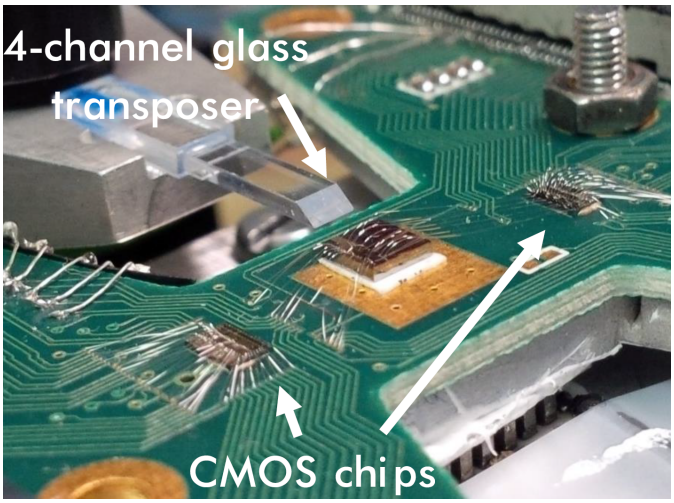

Figure 6.12: *Photo of the PCB with the PIC and the two CMOS ASICs. The glass transposer has to directly touch the grating couplers for injecting the modes. (Source: [103])*

6.4.2 Steering, coupling and identification of a free space optical beam

The SiP mesh was employed to manipulate free space optical beams, and, in detail, the following functionalities were demonstrated:

(i) **Beam steering** As a first application we used the mesh to demonstrate the steering of a free space optical beam. To this end, we injected into the mesh an optical signal from port WG1 (see Fig. 6.13(a) and we measured the radiation pattern generated by the grating array (RPi) for different tuning states of the mesh. The radiation pattern was measured by sampling the optical field along the transverse x-axis with a probe fiber with a resolution dx = 5 μm. Figure 6.13(b)

shows the radiated field at a distance of (11 mm) from the output ports when the mesh is tuned in order to maximize the power received by a first detector D_1 (placed in x = 0, mesh state M_1) and by a second detector D_2 (x = 100 μm, mesh state M_2). The spacing between the maxima of the field pattern (about 150 μm, corresponding to an angular spacing of about 1°) is related to the large physical distance (127 μm) between radiating elements. Figure 6.13(c) shows the optical power collected by a detector (1 mm fiber collimator spaced 51.5 cm away from the chip) placed at the same angular direction of D_1 and D_2, when the mesh is tuned in states M_1 and M_2. Though the steering angle is rather limited, this demonstrate high resolution in the control of the radiation direction.

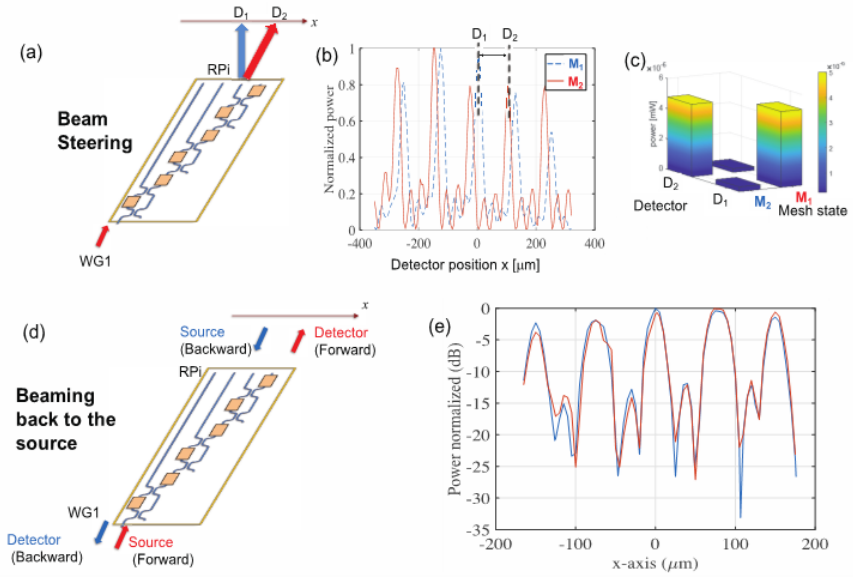

Figure 6.13: *(a) Schematic representation of the beam steering experiment. (b) Free-space radiation pattern measured at the distance of 11 mm from the grating array RPi when the light is coupled to input port WG1 and the mesh is tuned in two different states M_1 and M_2. (c) Optical power measured by a detector (collimator) placed at positions D_1 and D_2 when the mesh is configured in states M_1 and M_2; (d) schematic representation of the "beaming back" experiment: the source and the detector are swapped to observe the behavior of the mesh when the direction of the optical propagation is reversed. (e) Comparison between the field pattern measured by a free-space detector moving along the x-axis when the source is coupled to port WG1 (red line) and the optical power measured by a detector coupled to port WG1 when a free space source moves along the x-axis (blue line).*

(ii) **Beaming back to the source** We also investigated the behavior of the mesh when the direction of the optical propagation is reversed, that is when the source and the receiver are swapped. A free space beam coming from a collimator (beam waist 1 mm) at a distance of 6.5 mm from the mesh was used to shine the light on the grating array RPi while a photodiode was coupled to port WG1 (blue arrows in Fig. 6.13(d)). The blue curve in Fig. 6.13(e) shows the optical power at the photodiode (WG1) when the position of the collimator (free space beam) is shifted along the x-axis. The red curve is the power collected by the sliding collimator (receiver) when a light source is coupled to port WG1 and the grating array is used as a radiating antenna (red arrows in Fig. 6.13(e)). The good matching between the forward and backward behaviour demonstrate the capability of the mesh to beam the field back toward a free-space source along an arbitrary direction, this operation not being achievable with a conventional mirror.

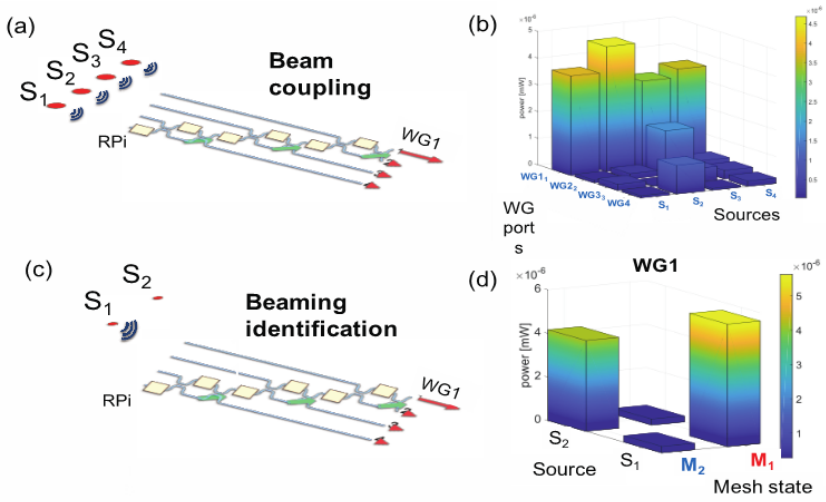

Figure 6.14: *(a) Schematic representation of the beam coupling experiment. (b) Optical power coupled at the waveguide ports (WG1-WG4) when the mesh is configured to couple the light from an arbitrary free space source (S_1-S_4) to port WG1. (c) Schematic representation of the beam identification experiment. (d) Optical power coupled at port WG1 when the mesh automatically self-configures to maximize the power coming from an unknown source (S_1 or S_2).*

(iii) **Beam coupling and source identification** The high angular resolution of the mesh can be exploited to couple into a single-mode optical waveguide a free-space beam coming from an arbitrary direction

of arrival, while minimizing the coupling from other directions. To demonstrate this concept, four free space optical beams (S_1-S_4) were simultaneously shone on the grating array RPi by using an array of 4 fibers spaced by d = 127 μm at a distance of 5.5 mm from the mesh (see Fig. 6.14(a)). When a beam for a given fiber impinges on the grating array, the mesh automatically self-configures by following a progressive tuning scheme in order to maximize the transmission to port WG1. Figure 6.14(b) show the power coupled to the waveguide ports WGi when the mesh is configured to couple the light from S_1- S_4 to WG1. This feature implies that the mesh can automatically identify the direction from which a beam is arriving. In Fig. 6.14(c)-(d) a beam is coming from a source whose position is not known (it can either be S_1 or S_2). The mesh automatically self-configures to maximize the coupling to WG1 and once convergence is achieved, the phase shifts (voltages) are applied to the thermal tuners of the MZIs of the mesh identify the position of the source.

6.5 Beam front reconstruction

In Sec. 6.4.2 we studied free space beam coupler behavior to steer and correct the direction of the main lobe of the beam. Correction to track source or distinguish and couple to specific source among others. In this section we study in detail the features of the free space beam, including the side lobes and their relations with the main lobe. We study effect of phase perturbations on their relations and use mesh circuit to compensate for these unwanted effects. We start by known perturbation with predictable consequence on beam front and go to unknown scattering mediums with random effects.

Lets start by studying the far field of the circuit introduced in Sec. 6.4.1 which includes 4 radiators spaced 127 μm on a line. Introducing this phase array system in Sensor array analzer in Matlab [74], using a guassian beam with 3 degree beam width as the array element (as an estimation to the radiation pattern of a single grating coupler), we get the far field beam shape as Fig.6.15(a). This is the directivity of the beam in Azimuth plain cut at Elevation angle 0. Since array elements are multiples of λ distanced, the Fourier transformation of the array is repeated closely in far field of this antenna. In each 0.698 degree we see a repetition of the main lobe presented by red arrows in Fig.6.15(a). In each period there are 2 side lobes (Green arrows) and 3 zeros which are pointed by orange arrows.

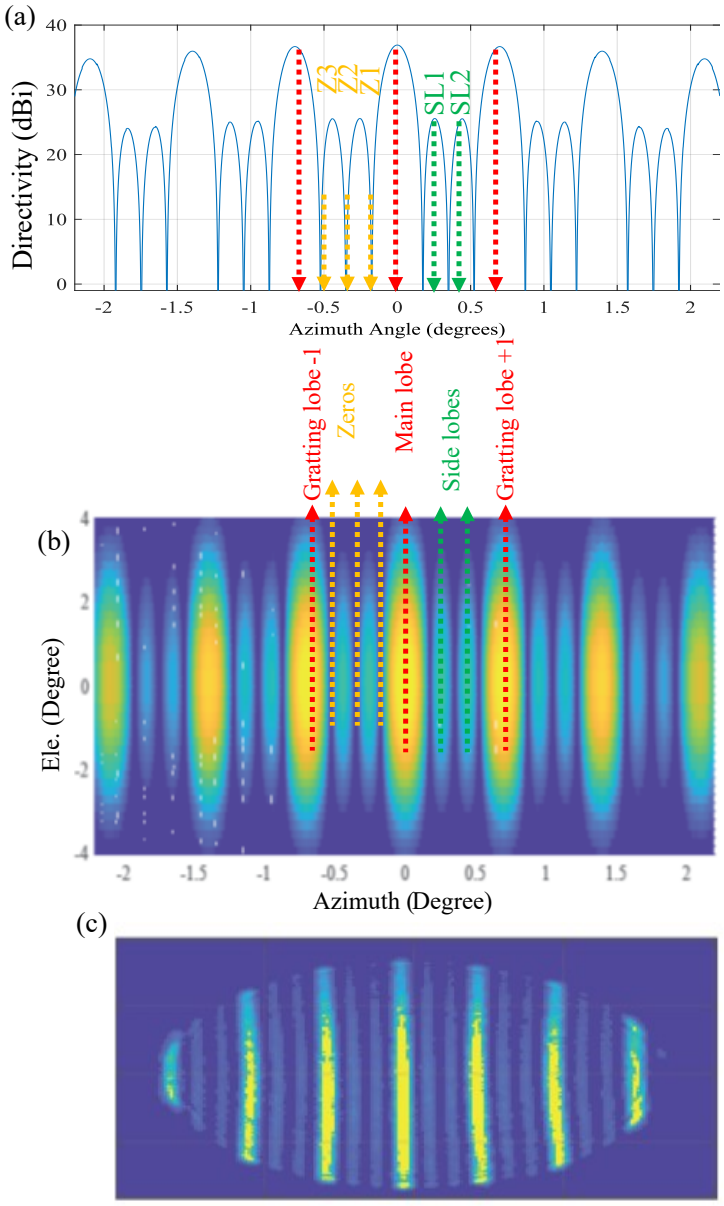

Figure 6.15: *(a) Elevation plain cut in simulation pattern of 4 element array spaced 127µm with uniform excitation highlighting the main lobe along side side lobes and the zeros. Grating lobes are spaced 0.688 degree apart due to large spacing of the array elements. (b) Simulated far field pattern in ± 2.2 degree Azimuth and ± 4 degree Elevation range. (c) Captured slice of the far field pattern via NIR camera through experimental trials.*

Fig.6.15(b) shows the simulation of the far field pattern in Azimuth ± 2.2 degree and Elevation ± 4 degree range. Beam front features like Main and side lobes alongside the zeros are pointed out with the same corresponding arrow colors.

Fig.6.15(c) is an experimental trials, presents a slice of the far field pattern captured via NIR camera (2.2.3). We can see direct match with the beam features obtained with simulation. In the next sections we introduce free space perturbations, to study their effects on the beam front and utilize mesh to correct and compensate for their effect. We start in Sec. 6.5.1 by introducing perturbations directly in array elements to have more clear understanding of the effects and then take a step further to perturbations in far field in Sec 6.5.2. Transformation introduced in the pattern can be automatically compensated by re-tuning the mesh according to techniques discussed in sec 6.2. Re-tuning the mesh ,which is direct minimization of stages, means introducing appropriate transformation to cancel the effect of the perturbing media.

6.5.1 Image plain perturbations

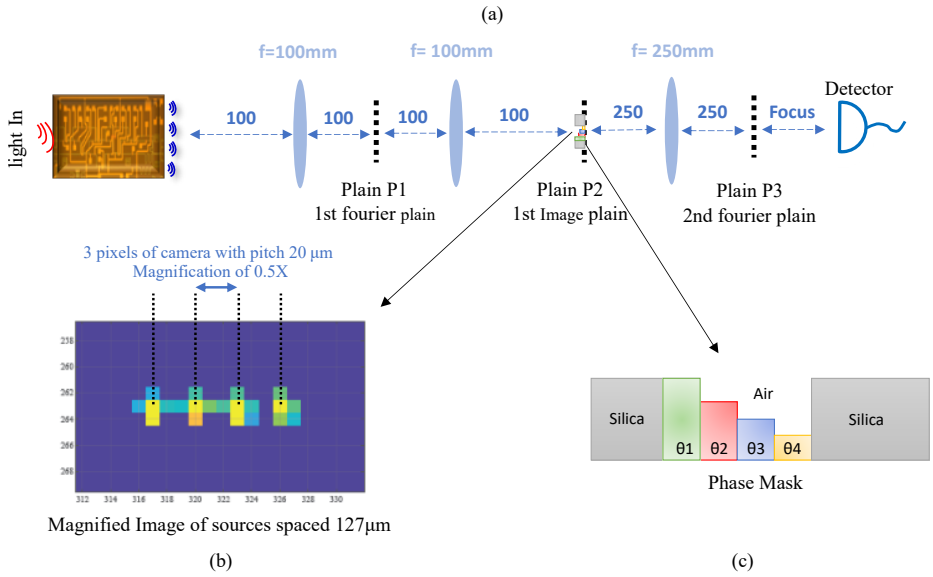

Figure 6.16: *(a) Optical setup to provide image of the array elements in plain P2. Far field pattern of the system is formed in plain P3 and image thorough a NIR camera. (b) Image of the sources formed in plain P2 captured by NIR camera, this images is magnified through a single lens system to compensate for de-magnification of the camera system to offer overall 0.5X magnification, space between elements is 3 (pixels)*20 µm (pixel pitch). (c) Schematic of phase mask providing combination of 3 variations of phase between 4 elements of the array. Build by 3 level of etching through a Borosilicate Glass wafer.*

Consequence of phase perturbations directly in array elements and their effects in the far field pattern of the antenna is more straight forward to understand than the ones in the far field. For example, introducing π phase difference between elements of the array in form of $[0 \quad \pi \quad 2\pi \quad 3\pi]$ exhibits itself as a half period steering in the far field beam. Introducing phase mask directly on the SiP chip is not practical due to close presence of wire bonding and small dimension of the chip (see Fig. 6.12). To avoid this difficulty, we can image the grating coupler (array elements) and introduce the perturbation in the image plain, Figure 6.16(a) presents the appropriate setup to do this.

Output fields of the 4 grating couplers are brought in Fourier plain (Plain P1) through a fourier transforming lens. This is done by placing the source at focal distance of a 100mm bi-convex lens to form the translation from angular frequency elements to spatial spacing in lens focal plain on

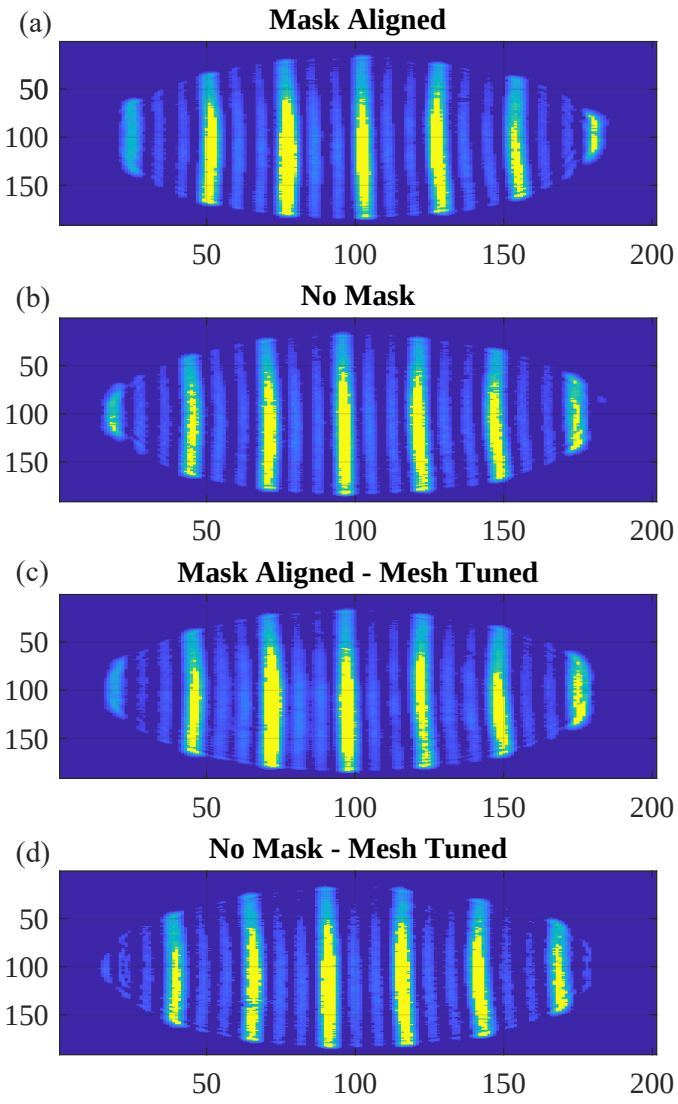

Figure 6.17: *Captured slice of the far field beam for (b) without perturbations in image plain as ideal beam front (the reference) (a) when the phase mask ($[0 \quad \pi/2 \quad 2\pi/2 \quad 3\pi/2]$) is aligned in the image plain resulting to shift of the main lobe to first zero on the right (c) re-tune of the mesh in presence of phase mask compensating for the phase perturbation and restoring the ideal beam front similar to b) front. (d) re-tuned condition of the mesh while the phase mask is removed demonstrating the pattern related to conjugate phase introduced by mesh to compensate for effects of phase mask. Axis are pixel numbers with pitch of $20\mu m$ between each pixel.*

the right (plain P1). Using the same lens (to have the same transforming coefficients) with the same spacing we can bring back the Fourier plain to image plain (sources) as pointed out by plain P2 in Fig.6.16(a). Plain P2 is the exact 1 to 1 image of the 4 gratings couplers, Fig.6.16(b) shows the magnified image of this plain (captured by NIR camera) presenting 4 grating couplers with small aberration effect due to the strong magnifying single lens setup. Considering the 0.5X magnification, camera sees them about 120μm spaced which is as they are considering the resolution limits of this camera.

Phase mask can be introduced easier in plain P2 to perturb directly the elements of the array. To observe the far field we can place the camera in far field distance or use a Fourier transforming lense and image its focal plain by the camera. Second technique preserve optical beam power by preventing it from diverging specially in the direction which array does not introduce gain (Elevation). In this experiment, this is done through a 250mm bi-convex lens as demonstrated in Fig. 6.16(a). The camera is focused at the right focal plain (P3) of this lens to capture the Fourier plain of the plain P2.

Phase mask is a SiO_2 wafer that is etched in 3 different levels (depths) to introduce 4 different phase levels if we consider no etched level as zero phase shift. Figure 6.16(c) present a schematic of this phase mask. From now onwards, we explain the introduced phase shift in the plain P2 by a vector of phases introduced by the phase mask as presented in Fig. 6.16(c).

We start by $[0 \quad \pi/2 \quad 2\pi/2 \quad 3\pi/2]$ as the phase mask, through simulation we understand it introduce 0.175 degree of shift in the far field pattern, shifting the main lobe to the first right zero. By placing this mask in plain P2 of Fig.6.16(a) in an experimental trial we captured the shifted beam presented in Fig. 6.17(a). Comparing (a) and (b) we can observe the expected shift. Considering a receiver placed in the center of the beam on the max of the main lobe in (b), with this shift the power coupling is reduced dramatically since there is the first zero at the left in the place of the main lobe. To restore the efficiency of the link we tuned the mesh connected to these 4 grating couplers to maximize the coupled power. Radiation pattern of retuned mesh is captured in Fig. 6.17(c), demonstrating exactly the same pattern without any phase mask (case (b)). To cancel the effect of phase mask $[0 \quad \pi/2 \quad 2\pi/2 \quad 3\pi/2]$ we need to use the phase mask $[0 \quad -\pi/2 \quad -2\pi/2 \quad -3\pi/2]$. If we remove the phase mask in Fig. 6.16(a) while maintaining the new tuning which gave us the Fig. 6.17(c), we observe that mesh is radiating with the pattern presented in Fig. 6.17(d) which is the consequence of changing

the phase of array elements exactly as $[0 \quad -\pi/2 \quad -2\pi/2 \quad -3\pi/2]$. Without any information about the phase mask and only by re-tuning the mesh considering the optical power as the merit, we can introduce exactly the needed modifications in the radiation beam to compensate for the phase mask.

We repeat this experiment with another phase mask to introduce even larger steering in the pattern. Inserting $[0 \quad \pi \quad 0 \quad \pi]$ in plain P2 of Fig. 6.16(a) we are shifting the main lobe half a period. Captured pattern in Fig. 6.18(a) present experimental proof of this shift which leads to loss of the coupling to the receiver placed in the middle of the beam. To recover the coupling efficiency mesh is re-tuned and optimum link is recovered as presented in Fig. 6.16(c). Removing the phase mask and looking at the radiation pattern of the system with new configuration, we can understand mesh introduced $[0 \quad -\pi \quad 0 \quad -\pi]$ in the array elements to cancel the effect of the phase mask.

To this point, we studied cumulative phase shifts leading to steering of the pattern which are compensated by the mesh through introduction of the inverse phase shift. At this stage we introduce a phase mask that not only steer the pattern but also change the ratio between side lobes and main lobe. Among huge set of phase changes presenting this kind of perturbation on the far field pattern, we chose $[\pi \quad \pi \quad 0 \quad 0]$ since its far field is easily distinguishable with camera. With numerical simulation we recorded the new pattern as presented in Fig. 6.19 at Elevation cut of zero degree. This distinctive pattern helps with alignment of the phase mask with the image of the gratings in free space.

After a good alignment of the phase mask the perturbed far field pattern is captured by NIR camera and presented in Fig. 6.20(a). Comparing with the optimum pattern in (b) one of the side lobes gain directivity (with reduction of the main lobe) to become equivalent to the directivity of the main lobe and the second side lobe lost its directivity completely. These results completely match with the simulation presented in Fig. 6.19. Receiver placed in the middle of the far field pattern completely lost its coupling efficiency in this new configuration. Re-tuning the mesh allowed us to recover the power at the receiver which translated to the ideal pattern of the system captured in Fig. 6.20(c). Max of the main lobe is at the center of the far field overlapping with the receiver.

Removing the phase mask from the setup in Fig.6.16(a) and capturing the far field of the mesh we see the radiation pattern corresponding to

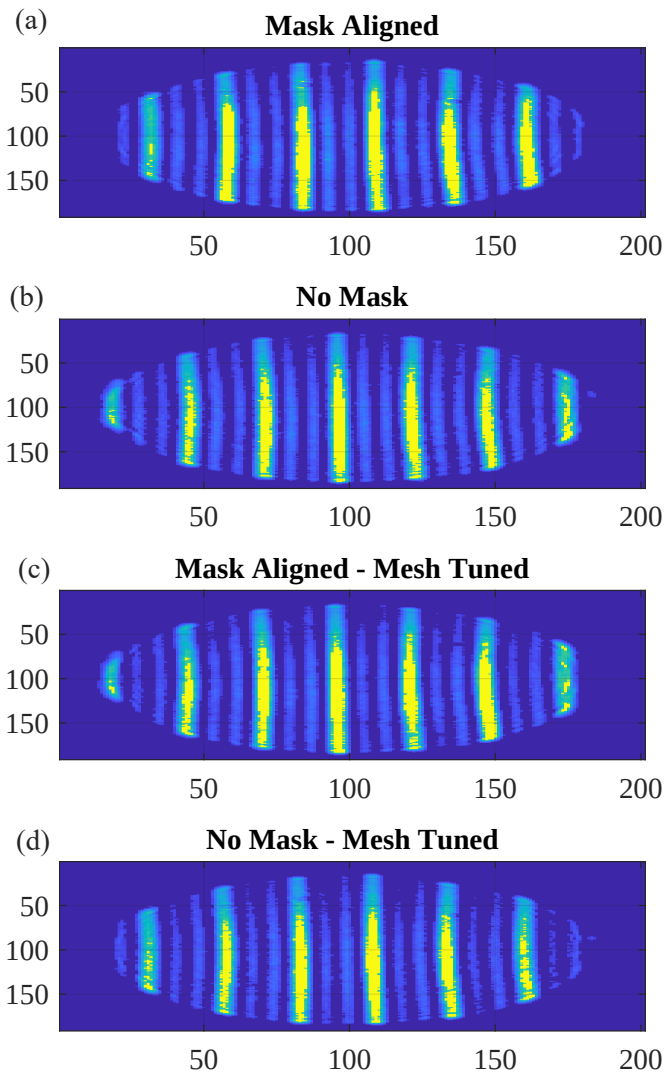

Figure 6.18: *Captured slice of the far field beam for (b) without perturbations in image plain as ideal beam front (the reference) (a) when the phase mask ($[0 \quad \pi \quad 0 \quad \pi]$) is aligned in the image plain resulting to shift of the main lobe half period to the second zero on the right (c) re-tune of the mesh in presence of phase mask compensating for the phase perturbation and restoring the ideal beam front similar to b) front. (d) re-tuned condition of the mesh while the phase mask is removed demonstrating the pattern related to conjugate phase* $[0 \quad -\pi \quad 0 \quad -\pi]$ *introduced by mesh to compensate for effects of phase mask. Axis are pixel numbers with pitch of* $20\mu m$ *between each pixel.*

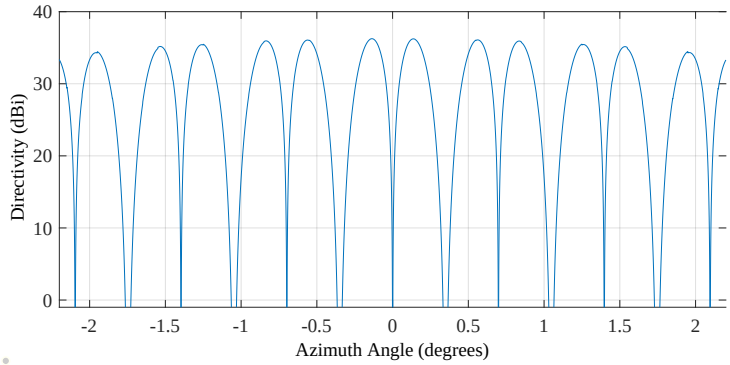

Figure 6.19: *Simulated Elevation cut plain of the 4 elements array with* $[\pi \quad \pi \quad 0 \quad 0]$ *perturbation in each element. In this pattern side one side lobe has the same directivity of the main lobe while the other one is zero.*

phase changes of $[-\pi \quad -\pi \quad 0 \quad 0]$ in the array elements which are automatically introduced by the mesh. This phase configuration was expected to cancel the effect of the phase mask and mesh automatically through tuning process manage to introduce it. This is done without the information on the value or type of the phase perturbation in the phase mask.

A step further, we introduce a mask not only introducing phase perturbations but also modify the amplitude of the sources. This is done by patterning 40nm of Chromium layer on the phase mask through thermal evaporation. The mask is introducing $[20^\circ \quad 20^\circ \quad 0 \quad \pi]$ phase shift and $[0.2 \quad 0.2 \quad 1 \quad 1]$ amplitude transmission. Aligning the mask in the image plain (plain P2 of Fig.6.16) we obtain perturbed pattern as capture in Fig.6.21(a) via NIR camera. It's not possible to compensate this perturbation by a phase array systems and we need to modify the amplitude of the radiators too. This is one of the moments that integrated meshes shine comparing to traditional phase arrays. Not only this compensation can be done automatically by minimization of each stage (as described in Sec. 6.2) but via integrated mesh we can also modify the amplitude of the radiators to obtain best fit pattern compensating the effect of this mask. Figure 6.21(c) shows the captured pattern after re-tuning the mesh to new condition of free space link. Comparing images (c) and (b) in Fig.6.21 we can appreciate the realigning of the pattern for maximum coupling to the receiver at the center of the pattern. These images in Fig.6.21 are normalized in power to the (a) and observing (c) we can understand the lower received

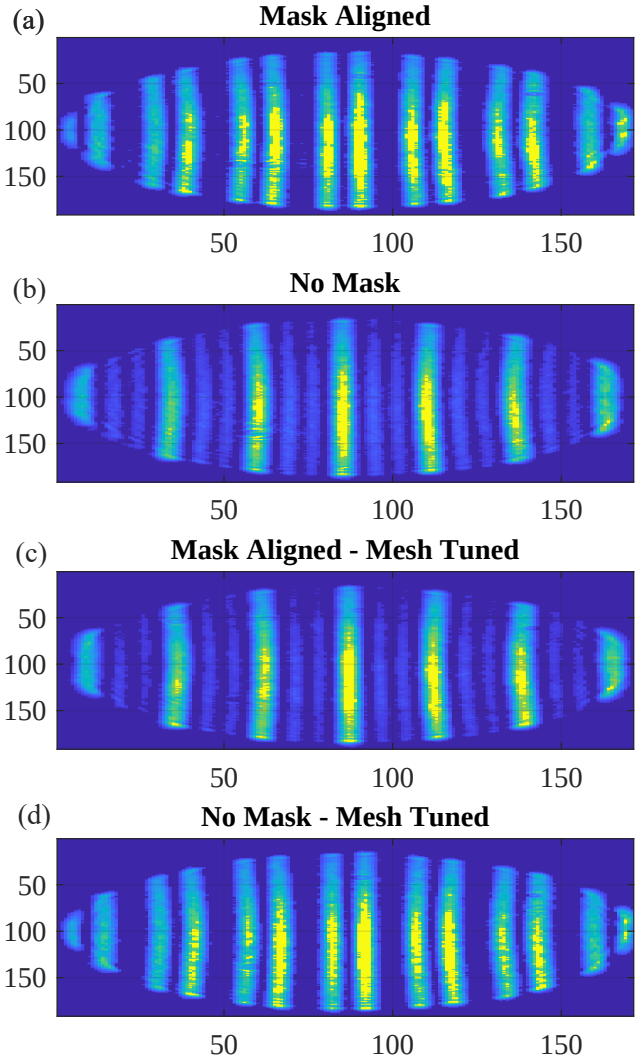

Figure 6.20: *Captured slice of the far field beam for (b) without perturbations in image plain as ideal beam front (the reference) (a) when the phase mask ($[\pi \quad \pi \quad 0 \quad 0]$) is aligned in the image plain resulting to null of one side lobe and growth of the other one to the same directivity of the main lobe leading to dual-main lobe pattern. (c) re-tune of the mesh in presence of phase mask compensating for the phase perturbation and restoring the ideal beam front similar to b) front. (d) re-tuned condition of the mesh while the phase mask is removed demonstrating the pattern related to conjugate phase introduced by mesh to compensate for effects of phase mask. Axis are pixel numbers with pitch of $20\mu m$ between each pixel.*

power at the detector since there is no amplifying unit (active device) inside this integrated mesh to produce additional power compensating for the attenuation of the mask. This mesh can only re-distribute the radiated power to compensate for the attenuation of the mask recovering optimum free space beam.
To compensates this mask the mesh needs to modify radiator phases as $[-20^{\circ} \quad -20^{\circ} \quad 0 \quad -\pi]$ and re-distribute the power at each radiators like $[1.4 \quad 1.4 \quad 0.6 \quad 0.6]$. This beam compensate the perturbation of the mask leading to the uniform array after wards to obtain the beam front as captured in Fig.6.21(c). The compensating beam front from the mesh is captured by maintaining the new tuning and removing the mask which is presented in Fig.6.21(d). Comparing images captured in Fig.6.21(a and d) by numerical simulation taking into account perturbations of the mask and modification of the mesh to compensate for it in Fig.6.22(a,b), one can appreciate the accuracy of self-adjusting mesh performance. Integrated mesh re-tune itself to radiate appropriate beam without the knowledge of the mask only by self-adjusting each MZI stages.

Linear perturbations introduced in the image plain, directly at the array elements, mathematically should be compensated by the conjugate perturbation and with experimental trials we observed the same behavior is automatically obtained by re-tuning the mesh. Re-tuning the mesh to optimized a goal function which could be max power at a receiver or stage minimization of the power, automatically introduce appropriate linear transformation to compensate the effect of the perturbing medium. There is no need to know the phase mask to prepare the appropriate tuning condition while re-calibration process is the same regardless of the phase mask. A library (LUT) of tuned conditions of mesh for different phase masks can help identifying the presence of an unknown phase mask. This concept can be translated as transparent label identification by integrated mesh. In the next sections we observe the same behavior in the far field, meaning perturbations in the Fourier plain are automatically compensated by the mesh through introduction of the appropriate transformation by modifying the individual array elements.

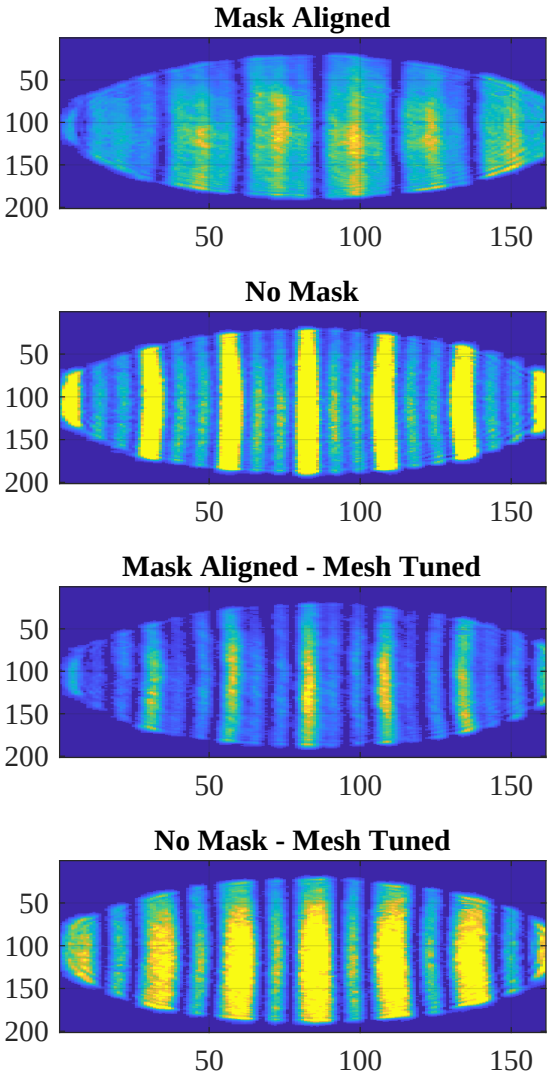

Figure 6.21: *Captured slice of the far field beam for (b) without perturbations in image plain as ideal beam front (the reference) (a) when the mask (phase =* $[20^\circ \quad 20^\circ \quad 0 \quad \pi]$*, amplitude =* $[0.2 \quad 0.2 \quad 1 \quad 1]$*) is aligned in the image plain resulting to null of one side lobe and growth of the other one to the same directivity of the main lobe leading to dual-main lobe pattern. (c) re-tune of the mesh in presence of phase mask compensating for the phase perturbation and restoring the ideal beam front similar to b) front. (d) re-tuned condition of the mesh while the phase mask is removed demonstrating the pattern related to conjugate phase introduced by mesh to compensate for effects of phase mask. Axis are pixel numbers with pitch of* $20\mu m$ *between each pixel.*

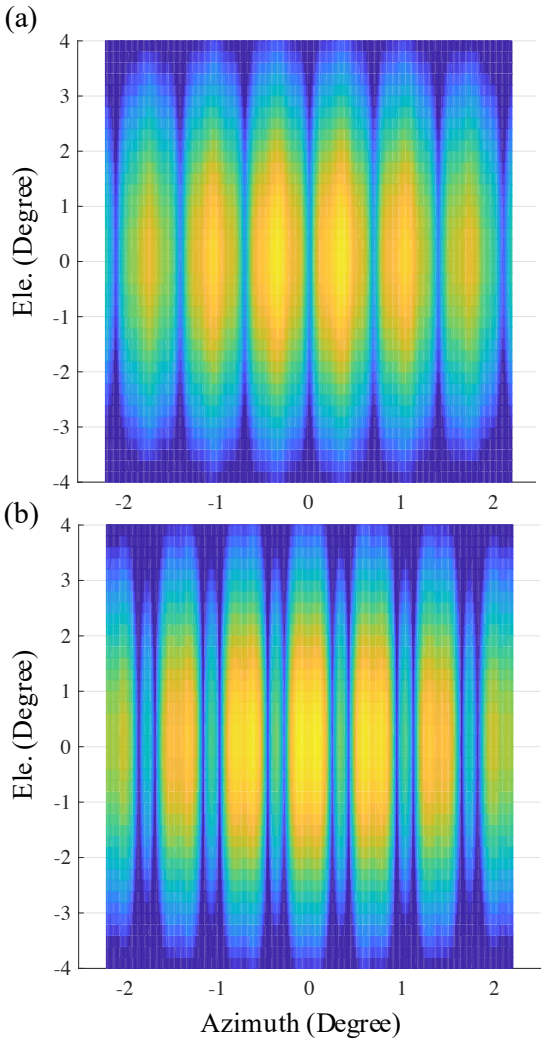

Figure 6.22: *Simulated slice of the far field beam for (a) when the mask (phase=*[20° 20° 0 π]*, amplitude=*[0.2 0.2 1 1] *) is aligned in the image plain resulting to null of one side lobe and growth of the other one to the same directivity of the main lobe leading to dual-main lobe pattern.(b) re-tuned condition of the mesh while taking into account required compenastion to cancel the effect of the mask.*

6.5.2 Far Field beam perturbations

The capability of the mesh to operate as a programmable beam carver was exploited to demonstrate free space transmission through an obstacle corrupting the phase front of the free space beam. Figure 6.23(a) shows the schematic of the free space setup where the 1x4 mesh is used as a transmitter while a near-IR camera is used as a detector. The mesh is initially configured in order to establish the optimum communication link, that is to maximize the light intensity at the center of the camera [Fig. 6.23(c)]. A planar phase mask [Fig. 6.23(b)] consisting of two transparent slits spaced by 300 μm and introducing local π-shifts across the phase front of the beam was introduced along the path at a distance of 10 cm from the mesh output.

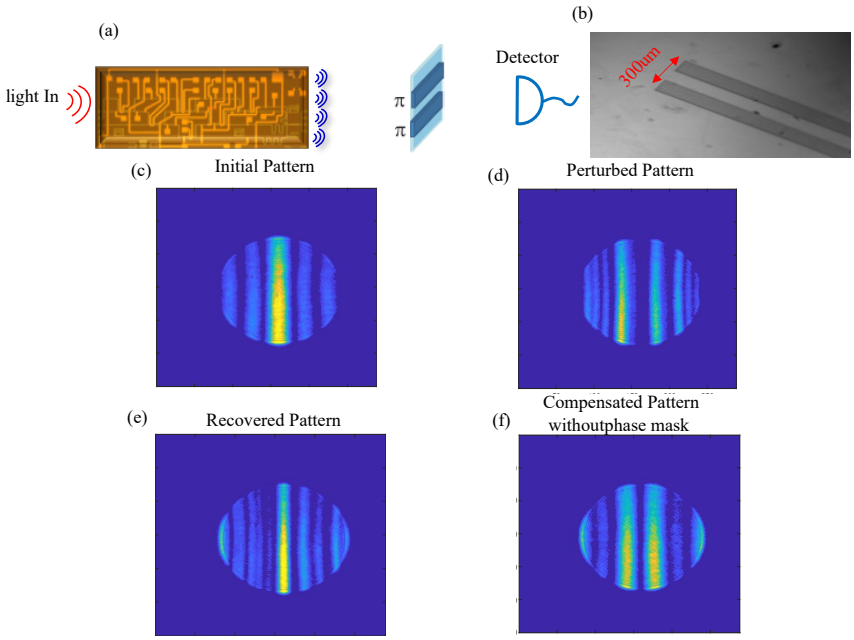

Figure 6.23: *Phase front corrections in a free space optical link: (a) schematic of the setup, where a 1x4 diagonal mesh is used as a beam shaper for free space communications and a near-IR camera monitors the intensity profile at the detector. (b) Phase mask employed along the free space link to introduce phase front perturbations (π shifts) across the beam profile. Radiation pattern recorded by the near-IR camera for (c) optimum free-space channel established without the phase mask in the path, (d) after the introduction of the phase mask medium and (e) after the re-calibration of the mesh compensating for the phase front distortion due to the phase mask, (f) maintaining the re-calibration status while removing the phase mask demonstrate the radiated pattern from the mesh compensating for phase mask effects.*

Upon the introduction of the phase mask, the field pattern is substantially altered and exhibits zero intensity at the center of the beam profile at the camera [Fig. 6.23(d)]. Figure 6.23(e) shows that the phase-front perturbation introduced by the phase mask can be compensated by reconfiguring in mesh, whose amplitude and phase output beams can be set to re-establish the best communication channel. Removing the phase mask, Fig. 6.23(f) shows this beam which , as expected, is the phase conjugation of the phase mask. Similar results were achieved by replacing the phase mask with a diffusive optical element, in which case the recovery of the link performance provided by the mesh is only limited by the number of radiating elements of the mesh itself.

6.5.3 Compensating scattering medium effects on free space beam

In previous section (Sec. 6.5.2) we demonstrated the effects of engineered phase perturbing mask on the far field beam and re-tuned the mesh to radiated with the appropriate beam, canceling the effect of that mask. Since the mask was known, compensation could be done by modifying the mesh to change the beam to the phase conjugation of the mask without the need for re-tuning the mesh. Changing actuators to apply the needed phase variation. In this section we want to understand the effectiveness of the mesh in presence of unknown masks. This can be a representation of badly aligned and dirty free space setup or perturbation in free space link like particles or smoke. In this experiment, we start from the established link at further distance from the mesh (comparing with previous section) with the optimized beam presented in Fig. 6.24(b). A weak plano-cylindrical lens, with finger prints and pieces of scotch is added to the link as the scattering medium presented in Fig. 6.24(a). The perturbed far field beam at the detector is presented in Fig. 6.24(c) demonstrating the distorted beam with loss of coupling to the receiver at the center of the pattern. Re-tuning the mesh to maximize the coupled power to the receiver we can recover the appropriate beam for the setup Fig. 6.24(d).

New configuration of the mesh is compensating for the phase and amplitude perturbations caused by the scattering medium as much as allowed by the resolution and arrangement of the mesh. If we remove the scattering medium and observe the beam front (see Fig. 6.24(e)) we can appreciate the appropriate beam canceling the effect of scattering medium. This beam is not know prior to re-tuning the mesh since behavior of the scattering medium inside the far field is not known. In all the stages of this

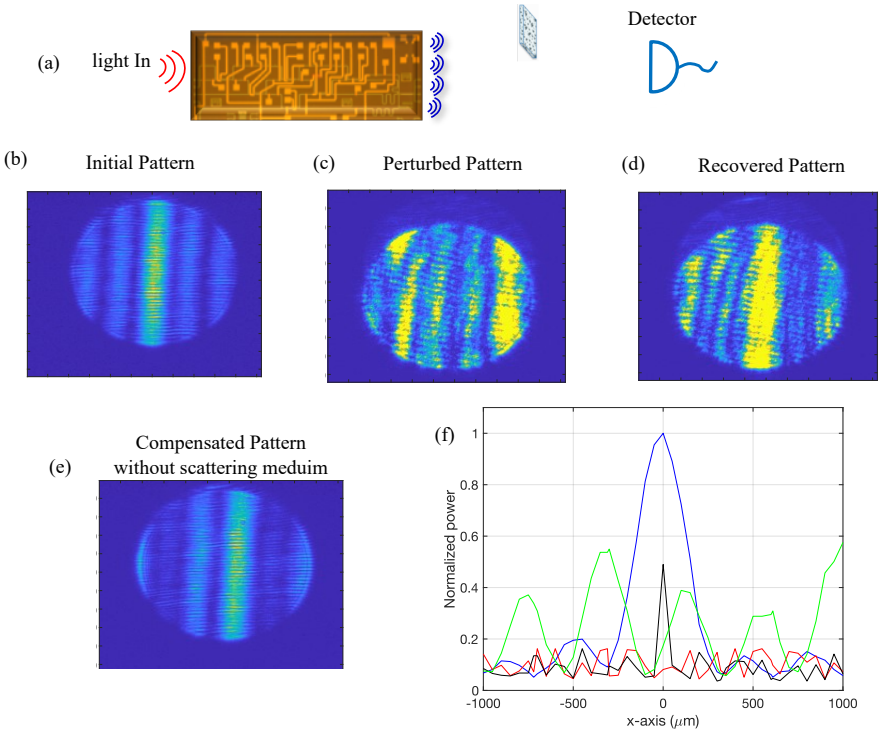

Figure 6.24: *Phase front corrections in a free space optical link: (a) schematic of the setup, where a 1x4 diagonal mesh is used as a beam shape for free space communications and a near-IR camera monitors the intensity profile at the detector. (b) Initial pattern in far field of the array captured via NIR camera, (c) Introducing a weak and dirty cylindrical lens as a scattering medium in the free space link leads to destruction of the far field pattern capture here, (d) far field pattern of the re-calibrated mesh to maximize the coupled power at the receiver which is placed in the center of the beam. Limited degrees of freedom in mesh managed to restore parts of the pattern appropriate for restoring the coupling to the source in the center of the beam. (e) Radiated pattern from the mesh suitable to compensate for the effect of the scattering medium recorded by removing the scattering medium while maintaining the re-calibration. (f) Sampled far field pattern by linear shifts of the receiver for b) initial in blue curve c) perturbed in red d) recovered pattern in black and e) compensating pattern in green curve.*

experiment we swept the receivers ± 1000 μm to record a cut in the beam amplitude on the plain of the receiver. Blue curve in Fig. 6.24(f) is the initial, the starting point of the experiment with acceptable coupling to the receiver. Introduction of the scattering medium leads to the loss of the coupled power in the receiver depicted by red curve in Fig. 6.24(f). Re-tuning the mesh allows for the partial recovery of the optimum coupling condition as observable by the Black curve. Part of the power which is scat-

tered away or lost inside the medium is obviously beyond compensation and higher resolution of the mesh and 2D arrangements of the radiators should improve the results dramatically due to higher degrees of freedom to produce better compensating mode for the scattering medium. If we remove the scattering medium, Green curve in Fig. 6.24(f) demonstrate the best offer-able beam by this mesh to cancel the effect of the scattering medium in this link.

Integrated meshes can establish and maintain the optimum communication link for the specific perturbed channels. They can automatically introduce appropriate transformation to cancel the effect of the transformation due to the scattering mediums in the link. Multiple output diagonal meshes can guarantee multiple orthogonal diffraction limited free space channels between two integrated meshes.

6.6 Summary

We demonstrate manipulation of free-space optical beams by using a 4x1 self-configuring SiP mesh. The performance of the mesh in steering, coupling and identifying free-space beams can be improved by optimizing the design of the radiating elements, whose number can be scaled up without impairing the progressive self-configuration procedure employed for the tuning of the mesh. Applications are envisioned to more advanced free-space optical processing, including phase front reconstruction, beaming through scattering media and chip-to-chip free space communications.

In particular, after comparing variety of integrated mesh structures a self-converging control loop is suggested and examined capable of tuning and re-steering such devices. The performance of control approach is examined for the case of global detector (single PD) or spread detection (CLIPP at each stage). Effect of these control algorithms on the radiation performance of the device are analyzed to understand the silver lining between sensitivity and perturbation. Then using a simple 4X1 diagonal mesh, we successfully performed beam coupling from a light source in the free space to a SMF just accurately tuning the MZIs mesh. As expected, also the reversed process, from a SMF to a specific position, worked as well. Steering the beam through mesh tuning is therefore a straightforward consequence of the alienable beam coupler when used in the opposite propagation direction. Capability of mesh to reconstruct the beam front was putted to trials by introducing known and unknown (replicating unwanted free space perturbations) perturbing mediums in the image and far filed

plane of the device. In all the trials (within the degrees of freedom offered by this mesh) ideal beam pattern was recovered which demonstrated the possibility of mesh to reconstruct the optimum free space channel. Integrated meshes can be automatically tuned (by simply minimizing stages) to manipulate both phase and amplitude of the array elements to offer more degrees of modification in beam front comparing with phase array structures.

Conclusions and Future Directions

It is wise to keep in mind that neither success nor failure is ever final.

- Roger Babson

In this thesis, we discussed essential recipes to cook reconfigurable and robust PICs. These concepts include techniques applicable in design, calibration and operation phase of PIC implementation. We examined each of these concept on different PIC topologies implemented in multiple technologies.

We started from studying the effect of mutual crosstalk induced by thermal tuners and suggested a cancellation technique by using as control parameters the eigenvectors of the thermally coupled system (TED technique). The TED method enables to speed up the convergence of generic automated tuning algorithms and make them more robust against instabilities and convergence failures. The best performance of TED-based algorithms is achieved when the phase coupling matrix $\mathbf{T}$ describing thermal crosstalk is exactly known, which is hardly achievable in most cases. However, just slightly sub-optimal performance is observed with an approximate estimation of the $\mathbf{T}$ matrix, which can be easily achieved electrically by exploiting integrated heaters as temperature sensors. Tuning procedures are advantageously carried out by defining a suitable cost function on the optical signal(s) at the output of the PIC without targeting a predefined frequency response. This enables to steer the PIC to a state that

optimizes its operation on those specific channels. In order to make it possible when several signals coexist in the same PIC, each signal is labeled though weak modulation tones in such a way that it can be monitored independently form the others by a lock-in detection. Applying this concept to a 2x2 cross-bar interconnect of MRRs we showed that optical paths across the PIC are correctly set when the cost function can discriminate the optical power of each signal.

If the spectral characteristics of the signal change, for instance its bandwidth, the control parameters driving the PIC actuators are automatically modified to re-optimize the cost function on the new set of input signals. We showed that the frequency response of a third order coupled MRR filter, which is not supposed to be a tunable bandwidth device, is significantly reshaped when the bandwidth of the input signal is reduced (from 5 GHz to CW), in order to maximize the isolation across the signal bandwidth. This feature is of particular interest for programmable filters, such as the variable bandwidth filter where, instead of using predetermined values of the control parameters to obtain a specific response, automated tuning of the filter to the optical signals try to find the best compromise for all the present channels, according to the defined cost function.

Tuning strategies presented in this thesis were employed for calibration and control of an add/drop hitless filter operating on a DWDM grid [80]. In particular we successfully demonstrated that these procedures can be used to automatically generate and dynamically update the lookup table of the filter when it is operated on a system with flexible bandwidth channels from 10 Gbit/s to 100 Gbit/s. Further we suggested using the optical output signal from a golden filter (as a reference to its frequency behavior) can be adopted to tune the same family of devices, reducing the time and resources needed in calibration phase of PIC.

These techniques, which here are applied to several PICs, can be employed to generic reconfigurable PIC architectures with an arbitrary topology and implementing different functions, such as MZI switch matrices [105] [32] and programmable photonic processors [24] [106].

This thesis is concluded in last two chapters to design and implementing two complex families of PICs following the recipes given in previous chapters. These devices includes a reconfigurable and hitless tunable add/-drop device operating on C+L telecommunication band capable of adding and dropping network channels while being polarization independent. In particular, we report on a fully-reconfigurable add-drop silicon photonic filter, which can be tuned well beyond the extended C-band (almost 100 nm) in a complete hitless (>35 dB channel isolation) and polarization trans-

parent (1.2 dB polarization dependent loss) way. This achievement is the result of blended strategies applied to the design, calibration, tuning and control of the device. Transmission quality assessment on dual polarization 100 Gbit/s (QPSK) and 200 Gbit/s (16-QAM) signals demonstrate the suitability for dynamic bandwidth allocation in core networks, back-haul networks, intra- and inter-datacenter interconnects.

The second device is an integrated mesh of MZIs capable of manipulating and modifying free space beams to either satisfy the new requirements of free space communication or compensate for the presence of random perturbing mediums in the path. We suggested design techniques and control approaches for both of these devices to satisfy desired requirements and demonstrated these results through experimental trials. In details, after comparing variety of integrated mesh structures a self-converging control loop is suggested and examined capable of tuning and re-steering these devices. The performance of control approach is examined for the case of global and local detection. Effect of these control algorithms on the radiation beam of the device is analyzed to understand the trade off between sensitivity of control and detrimental perturbation. Using a 4X1 diagonal mesh, we successfully performed beam coupling from a light source in the free space to a SMF while tuning the MZIs mesh minimizing the optical power at each stage. Steering the beam through mesh tuning is therefore a straightforward consequence of the alienable beam coupler when used in the opposite propagation direction. Capability of mesh to reconstruct the beam front was putted to trials by introducing predefined and unknown (replicating unwanted free space perturbations) mediums in the image and far filed plane of the device as perturbation plans. In all the trials (within the degrees of freedom offered by this mesh) ideal beam pattern was recovered which demonstrated the possibility of mesh to reconstruct the optimum free space channel. Integrated meshes can be automatically tuned (by simply minimizing stages) to manipulate both phase and amplitude of the array elements to offer more degrees of modification in beam front comparing with phase array antennas.

Future directions

Most of this thesis work were done in cooperation with an industry partner or European projects that had specific goals and tasks. This dictated some margins preventing deep exploration of different scientific aspects of these solutions in this work. Thus, as works to be further investigated

I can recommend:

- Higher resolution integrated meshes were designed based on this thesis and should be explored to study two dimensional array antennas with higher beam performance and tunability. It enables more degrees of freedom to better compensate for effect of scattering mediums.
- Multiple diffraction limited channels for mesh to mesh communication should be studied and demonstrated via higher resolution meshes and two dimension antenna array. A triangular mesh with multiple rows can be adopted to establish orthogonal optimum free space links between two meshes suitable to the free space channel.
- The concept of transparent labels can be explored via integrated meshes to obtain multi-dimensional coding. Depending on the compensation applied through mesh and via recording of the phase shifter values, we can cross reference and distinguish labels implemented in the free space link as scattering mediums.
- Automatic control techniques for add/drop device of chapter 5 should be explored to compensated for non-linearities in Silicon technology more specifically Two Photon Absorption (TPA). Control approaches based on TED technique can compensate resonance shifts due to TPA induced drifts and compensate via thermal actuators to restore the optimum frequency response of the device.
- Filter replication concept can be further expanded to evaluated the performance of the device before recording the calibration values. An automatic tunning technique can try to compensate for fabrication tolerances and based on the best value of the obtained merit function, one can judge the usability of the device. Then the obtained values of the actuators can be recorded in the LUT to guarantee the performance of device if its chosen as a valuable device. This step can be considered a testing phase before calibration of the device which can be automatized.
- Electronics multiplexers and grouping together optical wave guides to reduce electrical I/O was implemented in MPW run based on this thesis and need to be demonstrated to maintain the efficiency of the read out and actuation electrical commands while reducing the chip area needed for electrical wire bonding pads.

- Further exploration of thermal systems, including thermo dynamic and optical study of PICs to better optimize and calibrate design parameters which in return improves the control efficiency. In an MPW run based on this thesis some test structures are implemented to calibrate and validate numerical models and simulation results.

At the end, it's needed to be mentioned that the author was directly involved in all the discussed topics in terms of idea development, design of the chips (Chp.5 and new version of mesh in Chp.6), experimental setup development and analysis of the results. Along this thesis work several master students were followed and tutored. These works were carried out through collaboration of Photonics Devices group and I3N innovative integrated instrumentation for nanoscience following european H2020 and industrial projects.

APPENDIX A

Coupled Microring resonator filters

A.1 Spectral definitions and requirements

To introduce the fundamental parameters that qualify the transfer function (TF) of a generic band-pass filter, the terminology proposed in [107] is followed. Referring to Fig. A.1, that represents the typical transfer function of a band-pass filter where the grey columns represent the the WDM channels and f_1 and f_2 are respectively the distance in frequency between two adjacent channels and two non adjacent ones, the following figures of merit are defined.

- **Insertion Loss (IL)**: measure of how much the filter attenuates a channel at a given frequency.
- **Bandwidth (B)**: generally defined as interval of frequencies, in filter design is used to characterize the range of frequencies in which an insertion loss greater than 3dB or 20dB is introduced for channels added (or dropped) through the filter to the WDM grid.
- **Port Isolation, return loss ($\mathbf{R}_{in}$)**: is described as the minimum tolerated insertion loss experienced by the resonant channel when is selected and dropped from the WDM grid through the filter.

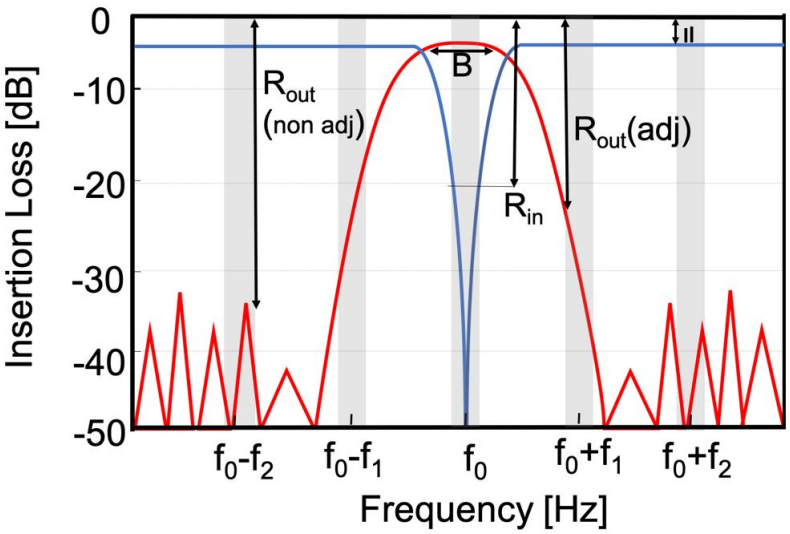

Figure A.1: *Typical transfer function of a band pass filter. The gray columns represent the WDM channels*

- **Out band rejection ($\mathbf{R}_{out}$)**: is defined as the minimum tolerated insertion loss experienced by the channels neighboring the resonant one. In this work specifically is refers to channels placed at 50 and 100 GHz spacing regarding the resonance of the filter.
- **Wavelength tuning range** range of wavelength filter demonstrates acceptable performance.In this range, known as operation band, filter should not has frequency footprints which can introduce perturbations to other channels of WDM grid.

Understanding these definition, the 4th order coupled MRR filter introduced in Chap. 5 was designed to satisfy desired requirements. These requirement are needed for a add/drop filter operating on DWDM grid to have optimum operations while being perturbation free. Table A.1 details these requirements and their limits along the measured performances obtained by the filter in Chap.5. Observing different rows of this table and comparing different merits with requirements we validate the optimum design of the device offered based on the novel design techniques.

Table A.1: *Filter Specification requirements along the performance measured with design suggestion in Chap. 5*

Parameters	Min	Typical	Max	Chap. 5 device	Unit	Notes
Operating wavelength	1529.16-1567.13			90	nm	Extended C band. FSR should be larger than operation wavelength range.
Channel spacing	100			100	GHz	
Polarization dependent Loss		0.5	1	<1	dB	Including coupling loss and on-chip loss.
Bandwidth@3dB	40			>39.8	GHz	Dispersion of DC coupler and even waveguide should be suppressed.
Bandwidth@20dB			80	>80	GHz	
Channel Isolation @50 GHz	20	25		>20	dB	Defined with respect to the clear pass band of the adjacent channel and channel.
Channel Isolation @100 GHz	30	35		>30	dB	
Port Isolation	18	20		>17	dB	Within Clear Pass Band (+/- 20 GHz)
Depth of notches outband			1.2	<1.2	dB	Along the complete tuning range
Locking Accuracy			+/-1	<1	GHz	
Heater response time		30			μs	
Clear Pass band		20			GHz	
Voltage of heaters		3.3	5		V	
Height of peaks			20	>20	dB	Along the complete tuning range below the max of drop
Insertion Loss			3	<1	dB	Relating to filter only

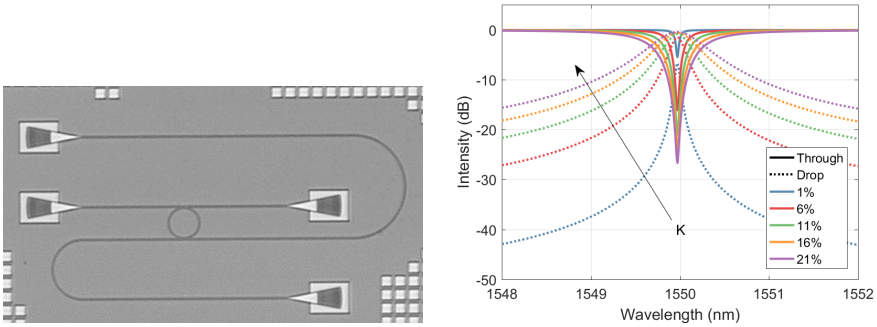

Figure A.2: *First order ring resonator a) microphotograph showing also input and output grating couplers and b) optical response as for diverse coupling coefficients.*

A.2 Micro-ring resonator

An add/drop single ring resonator as shown in Fig. A.2(a) is the simplest optical waveguide filter with a single-pole response. The location of the pole is determined by the coupling ratios and the attenuation in the ring. Its spectral response provides a narrower passband with higher stopband rejection as the pole moves closer to the unit circle, which is achieved by decreasing the coupling ratios and minimizing the ring loss. The main characteristics of this class of filters is a frequency response with high rejections and narrow bandpass. Figure A.2(b) demonstrate frequency response of this device against variation of its coupler.

A MRR OADM is a circle waveguide coupled to two straight bus waveguides providing the input and output path for WDM grid form the interferometer as presented in Fig. A.3.

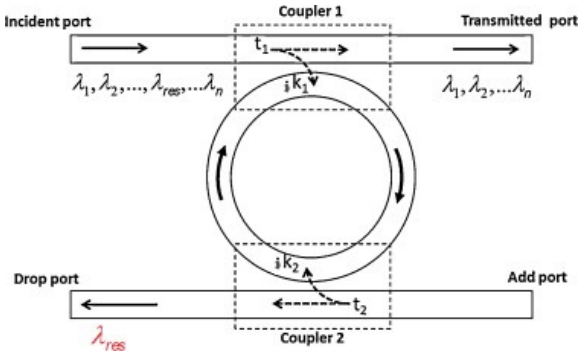

Figure A.3: *Concept of a single micro-ring resonator filter*

In order to explain the working principle of the MRR is important to introduce some spectral features that characterize the behaviour of the interferometer.

- *Resonance Condition*: it represents the condition for the light, after one round trip in the cavity, to have constructive interference the resonator. Resonant Wavelengths are given by

$$\frac{2\pi}{\lambda} n_{eff} L_r = 2N\pi \longrightarrow \lambda_{res} = \frac{n_{eff} L_r}{N}; \tag{A.1}$$

  where L_r is the ring circumference, n_{eff} the effective refractive index and the integer number N is called resonance order or angular mode number [107], and N=1 is the fundamental (or first) angular mode number.

- *Free Spectral Range (FSR)*: it is defined as the distance, in wavelength (or frequency), between two consecutive resonant wavelengths (or frequencies) [107]

$$FSR(\lambda)_{MRR} = \lambda_{N+1} - \lambda_N \leftrightarrow FSR(f)_{MRR} = \frac{c}{n_g L_r}; \tag{A.2}$$

  where c is the vacuum speed of light and n_g is the group index of the waveguide.

- *Finesse*: it is defined as the ratio between the FSR and the Bandwidth. This parameters is useful to quantify the frequency selectivity of the filter [107], i.e. rejections.

$$Finesse = \frac{FSR}{B}. \tag{A.3}$$

  Referring to Fig.A.3 and assuming the two couplers lossless and identical ($k_1 = k_2 = k$), the bandwidth of the MRR can be written as

$$B = \frac{FSR}{\pi} \frac{K}{\sqrt{1-K}}; \tag{A.4}$$

  where K=k^2 is the power coupling ratio of the directional coupler.

To select only one channel in the WDM grid and avoid aliasing due to the periodic resonance of the filter, the FSR should be larger than the operation band the span of the WDM grid. However, since the FSR is inversely proportional to the length of the resonator, this could require a very small radius which may lead to high bending loss for the guided optical mode.

Moreover the bandwidth of filter should be larger than the width of the WDM channels to avoid signal distortion and unwanted spectral shaping. This can be achieved through a careful dimensioning of the couplers, taking into account that each modification could worsen the finesse and therefore the rejections of the filter.

By cascading ring resonators one can create higher order filters. This allows the designer more flexibility in the filter design, who is able to, for instance, design filters with flatter passband or higher in-band isolation. The trade-off is the additional complexity required to manage the control parameters of the filter and the fabrication tolerances.

Tuning range

One key aspect when designing large FSR MRR filters is its tuning range. Since the actual length of the resonating structure can be quite small, few tens of micrometers, the thermo-optical tuning of that ring might require a reasonably high amount of temperature increase.

Further, the increase in the temperature of the filter poses requirements not only on the heater design *per se* but also creates problems related to cross-talk. In a PIC with diverse individual components such as modulators, filters, and photodiodes, the amount of heat generated by each one of those components might affect the performance of the others.

A.3 Coupled Resonator Vernier Filter

Consider high-order series-coupled ring resonators consisting, for simplicity, of two ring radii R1 and R2 (to be specific we choose R2 < R1). It can be demonstrated that, considering the group index n_g constant in all the elements of the filter, the total FSR is expressed by [108] [109]

$$FSR_{total} = m_1 FSR_1 = m_2 FSR_2; \tag{A.5}$$

where m_1 and m_2 are integers called Vernier Coefficients (VC) and represent the reciprocal proportion between the smallest FSR in the cascade, $FSR_{min} = FSR_1$, and the other FSRs in the series. As proposed in [110], to have the maximum increment in the FSR_{total}, m_1 and m_2 should be chosen as relatively prime integers or coprimes. The Extension Factor M can be therefore defined as the Least Common Multiple (L.C.M.) between m_1 and m_2. The length of each ring resonator can be determined by using

$$\frac{m_2}{m_1} = \frac{L_2}{L_1}, \tag{A.6}$$

being $R_2 < R_1$, $FSR_2 > FSR_1$ and $m_2 < m_1$ hold. The minimum of R_2 is determined by technological constraints and bending losses. Usually it is associated to a minimum acceptable bending radius through the Vernier coefficient m_2. Finally the condition for which all the rings in the series coupled microrings filter are resonating simultaneously at the same wavelength λ_{res} can be written as

$$\lambda_{res} = \frac{n_{eff,1} L_{r,1}}{N_1} = \frac{n_{eff,2} L_{r,2}}{N_2}; \tag{A.7}$$

where $n_{eff,n}$,$L_{r,n}$ and N_n are the respectively the refractive indexes, geometrical length and resonance order in ring N.
In order to identify the Vernier coefficients (VC) that maximize the FSR extension, some strategies are proposed in the literature [108] [111] [110].

However, the filters based on integers ratio of resonators could not comply with the spectral requirements in Table A.1, due to FSR smaller than tuning range dictated by the requirements. This is coming from the practical limit of the minimum radius of the resonators to have reasonable optical loss. Solution is using non-integer ratios between resonatros as discussed and analysed in Chap. 5 and in details in Sec. 5.1.

APPENDIX B

Self-aligning universal beam coupler

In this appendix, we briefly introduce (from literature) the most important theoretical concepts on the interferometric meshes, then, based on those principles, we will describe a universal beam coupler device and a universal optical component. We will briefly focus on free space communication channel realization in Section B.4.
These ideas are already described theoretically and published in couple of works, the aim of this Appendix is to bring important concepts needed for deep understanding of the Chap.6 discussions.

B.1 Mode conversion via linear optical devices

Our analysis starts analyzing a generic objects with linear behavior used in optics. A mode converter is a device capable of converting a set of orthogonal input modes to a matching set of orthogonal output modes. It can be demonstrated that if an optical device acts only linear transformations to the input modes, it can be described as a mode converter [112]. A mode can be defined as the field distribution that can be sustained by the considered volume. Therefore propagating modes in waveguides are different from modes in fiber or in free space. It is useful to say that the orthogo-

nal modes in one volume (e.g. waveguide) generate an Hilbert functional space that contains all the possible functions in that volume.

B.1.1 The mode converter basis set

A linear device can always be described by some linear operator D that can be called the device operator. D will have the mathematical function to take an input $|\phi_I\rangle$ and to generate the corresponding output $|\phi_O\rangle$

$$|\phi_O\rangle = D\,|\phi_I\rangle\,. \tag{B.1}$$

Knowing what output function will be generated for each input function, then D is completely defined and, by another point of view, D completely defines the optical component's behavior. The possible input function $|\phi_I\rangle$ will be in one mathematical function space (input's Hilbert space) H_I while the output one will be in the correspondent H_O. Generally the choice of these spaces is free, depending on the considered optical component.

The D operator can be seen as a general scattering matrix S, where the generalization comes from having no restriction in the mathematical characteristics of the input/output functions. In fact, S is usually creating monochromatic modes to output just reflecting the input ones. With D, the boundaries of the same physical volume or surface are removed and the output modes can be in very different volumes. Moreover, D doesn't need to be a square matrix nor a unitary one: squareness isn't required because the Output mode will be projected on the H_O functions that may be not present in H_I (for example from plane waves in free space, H_I, to guided modes in fiber, H_O), and a non-unitary matrix takes into account possible gain/loss or scattering into modes that are not included in the output mathematical space H_O.

Input/output mode functions are indicated by $|\phi\rangle$ due to the necessity of use a general notation. In a wide generalization, $|\phi\rangle$ may represent many different possible kind of fields, like monochromatic waves, waves varying in space, vector fields (like e.m. field), pulses, quantum spin fields and so on.
D can also be a time-dependent operator. If the devices structure depends explicitly in time, its describing operator has to presents the same behavior. E.g. pulse modes are orthogonal in time as spatial modes are orthogonal in space, and a combination of pulsed spatial modes has both the orthogonality characteristics. Of course linearity is a requirement in this analysis and to assure this property any variation in time in the device's response are predetermined and independent from the input or output.

A proper analysis of the D operator can be performed via the single value decomposition (SVD). From eq.(B.1) we can write

$$D = \sum_m s_{Dm} \left|\phi_{DOm}\right\rangle \left\langle \phi_{DIm}\right| \Longleftrightarrow D = V D_{diag} U^{\dagger} \tag{B.2}$$

where U and V are unitary operators in matrix form with $|\phi_{DIm}\rangle$ and $|\phi_{DOm}\rangle$ as column vectors and D_{diag} diagonal matrix with diagonal complex elements s_{Dm}. Functions $|\phi_{DIm}\rangle$ and $|\phi_{DOm}\rangle$ constitutes orthogonal sets in their respective spaces and are the solutions of the eigenvalues problems

$$D^{\dagger} D \left|\phi_{DIm}\right\rangle = \left|s_{Dm}\right|^2 \left|\phi_{DIm}\right\rangle \tag{B.3}$$

$$D D^{\dagger} \left|\phi_{DOm}\right\rangle = \left|s_{Dm}\right|^2 \left|\phi_{DOm}\right\rangle \tag{B.4}$$

in which the self-adjoint $D^{\dagger}D$ and $DD^{\dagger}$ operators share the same eigenvalues $|s_{Dm}|^2$.
The resulting sets of functions are complete: any function in the output space generated by the devices from a function in the input space can be written as a linear combination of the set of functions $ket\phi_{DOm}$ corresponding to non-zero singular values, and any function that can be generated by the device in the output space can be generated by some function in the input space that is a linear combination of the $|\phi_{DIm}\rangle$ corresponding to non-zero singular values.

The result pops up naturally: any linear optical device can be described by a linear operator D, which can always be decomposed to singular values, between input and outputs and there are two sets of orthogonal functions $|\phi_{DIm}\rangle$ and $|\phi_{DOm}\rangle$ which, living in different spaces, are related by a non-zero coupling coefficient s_{Dm}. Given D, it's always possible to retrieve the basis functions and the singular values which are unique. The device matrix or operator is diagonal when expressed in these basis sets. The result states that any linear optical device can be written as a mode converter, from specific orthogonal input modes to specific orthogonal output modes.

B.1.2 Mathematical implications

Let's consider now input functions $|\phi_I\rangle$ shining a linear optical component described by D which gives outputs $|\phi_O\rangle$. SVD can be performed, obtaining $|\phi_{DIm}\rangle$, $|\phi_{DOm}\rangle$ and s_{Dm}. The functions can be choose to be normalized

$$\left\langle \phi_{DIm}|\phi_{DIm}|\phi_{DIm}|\phi_{DIm}\right\rangle = \left\langle \phi_{DOm}|\phi_{DOm}|\phi_{DOm}|\phi_{DOm}\right\rangle = 1 \tag{B.5}$$

and among these the set of values s_{Dm}, at east one will have the largest possible magnitude $|s_{max}|$. Presuming 100% efficiency from input to output,

the mode of interest ($|\phi_{DI1}\rangle$ and $|\phi_{DO1}\rangle$) must be one of the possible SVD pairs with the largest magnitude of singular value s_{max}.

If instead of the ideal input function there is a misaligned one $|\phi_{Imis}\rangle$, it can be decomposed into a linear combination of the SVD set plus a another function $|\phi_N\rangle$ orthogonal to all the $|\phi_{DIm}\rangle$

$$|\phi_{Imis}\rangle = \sum_m a_m |\phi_{DIm}\rangle + |\phi_N\rangle \tag{B.6}$$

having $a_m = \langle\phi_{DIm}|\phi_{Imis}|\phi_{DIm}|\phi_{Imis}\rangle$. Each one of the components $a_m|\phi_{DIm}\rangle$ leads to a corresponding one proportional to $|\phi_{DOm}\rangle$, while any $|\phi_N\rangle$ will give no output in H_O: $D|\phi_N\rangle = 0$. Formally:

$$\begin{aligned} |\phi_{Omis}\rangle = D|\phi_{Imis}\rangle &= D\sum_m a_m|\phi_{DIm}\rangle + D|\phi_N\rangle \\ &= \sum_m s_{Dm}|\phi_{DOm}\rangle \end{aligned} \tag{B.7}$$

so the $|\phi_{Omis}\rangle$ component coupled to the output mode of interest is

$$\langle\phi_{DO1}|\phi_{Omis}|\phi_{DO1}|\phi_{Omis}\rangle = a_1 s_{max} \tag{B.8}$$

for an output mode of $a_1 s_{max}|\phi_{DO1}\rangle$.

By choice it can be said that $s_{max}|\phi_{DO1}\rangle$ corresponds to a unit power transfer efficiency ($\left\langle\phi_{DO1}|s^*_{max}s_{max}|\phi_{DO1}\middle|\phi_{DO1}|s^*_{max}s_{max}|\phi_{DO1}\right\rangle = |s_max|^2 = 1$ is the unit power in the output beam) and so power efficiency for coupling a misaligned beam into a 100% efficient coupler can be defined as:

$$\eta = |a_1|^2 \equiv |\langle\phi_{DI1}|\phi_{Imis}|\phi_{DI1}|\phi_{Imis}\rangle|^2. \tag{B.9}$$

Another very important consequence is the impossibility to combine multiple modes loss-lessly. Consider to have a perfectly loss-less coupling of beams into one output mode from some number of input modes. Let's start assuming that the pair of perfectly coupled modes is $|\phi_{DI1}\rangle$ and $|\phi_{DO1}\rangle$, so they have to be a pair of the mode converter basis modes for D. If there is another input mode $|\phi_{Dextra}\rangle$ orthogonal to $|\phi_{DI1}\rangle$ (so no component of $|\phi_{DI1}\rangle$ in the expansion for $|\phi_{Dextra}\rangle$). $|\phi_{Dextra}\rangle$ has to be a linear combination of the modes $|\phi_{DIm}\rangle$ for $m \geq 2$ or contains functions orthogonal to all $|\phi_{DIm}\rangle$. Hence, there is no coupling of the power from $|\phi_{Dextra}\rangle$ into the output mode $|\phi_{DO1}\rangle$ and any power is coupled into the other orthogonal modes $|\phi_{DOm}\rangle$ for $m \geq 2$ or is not coupled into any of them. Therefore, loss-less coupling from two orthogonal modes into one is not possible for any linear component (without an amplification mechanism)

This result is expected also from the Second Law of Thermodynamics, which does not allow the existence of a system that heat up a warmer black body from the output of two cooler black bodies.
The same result come from another interpretation can be given by Constant Radiance Theorem [113] in terms of optics schemes.

Concluding, any linear optical component can be considered as a mode converter that couples, one by one, from each of a set of orthogonal input modes to each of a set of orthogonal output modes. The idea of modes is understood to refer space-time variations of the considered fields, including both spatial beam forms as well as pulse shapes in general.

B.2 Coupling beams automatically

With the knowledge acquired in [112], it can be proposed a device that can take an arbitrary monochromatic input beam and couple it into a single mode guide or beam. With the use of feedback loops from detectors to modulator elements it would be possible to automatically adapt the device to any specific beam form [114].

B.2.1 Device concept

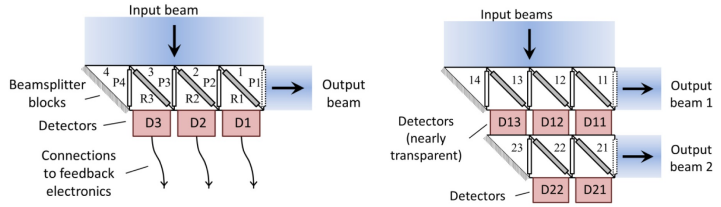

Figure B.1: *Conceptual scheme of the device: the incoming beam is sampled by beam splitter blocks, each with tunable phase shifter, reflector and detector. (a) With one single output mode and (b) with several outputs, in this case the detectors have to be transparent. (Source: [114])*

A conceptual scheme is reported in Fig. B.1. The beam is varying only in one direction and for illustration is divided into 4 pieces, each incident on a different one of the 4 blocks. One block, or beam splitter block BS_i, includes a variable reflector R_i and a phase shifter PS_i.

To start, the beam is shined onto the beam splitters and initially R_i and PD_i can be arbitrary as long as the reflectivities are non-zero (in order to have some power on the detectors D_i). First, PS_4 is adjusted to force the wave reflected downwards from BS_3 to be in anti-phase with any transmitted wave from the top through BS_3, in this way the power on detector $D3$ encounters a minimum value. Then, to keep minimizing it, the reflectivity R_3 has to be adjusted: when the reflected and the passing through waves have the same amplitude, being already in anti-phase, the power detected by D_3 is completely canceled. The process can be repeated for BS_2 and then $BS1$ first adjusting the phase shifter to minimize the detected power and then modifying the reflectivity to cancel out the power. At the end of the process, all the incident beam power emerges from the output port on the right.
This method has the peculiarity to be progressive and not iterative as typ-

ical adaptive optical schemes, and it is complete when the last reflector is adjusted. Requiring only local feedback for the minimization of one variable at a time, simple low-speed electronics can perform the loop, with no global calculation required. Because of this, the feedback system can be left running, cyclically stepping through the discussed minimizations.

B.2.2 Waveguide device

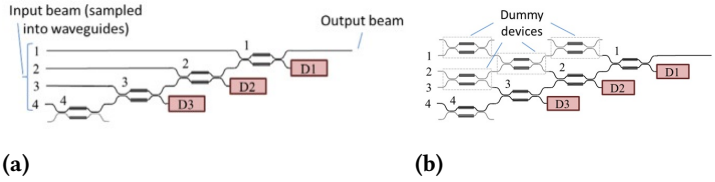

Figure B.2: *Mach-Zehnder Interferometer realization of the device a) with one single output mode and b) with added dummy MZIs in order to match the path length inside the mesh. (Source: [114])*

In Fig. B.2a is represented a device version that uses Mach-Zehnder Interferometers (MZIs) as adjustable beam splitter blocks. A MZI can act a controllable phase shift in each arm thanks to the common mode drive and a variable reflectivity (the splitting ratio between output ports) exploiting the differential arm drive. This configuration allows equal path lengths for all the beam portions and avoids diffractions inside the apparatus. Having equal path lengths is necessary to operate over a broad wavelength range in order to prevent relative propagation phase from changing with wavelength in the different waveguide paths, so dummy MZIs can be added to even the lengths as in Fig. B.2b. Dummy MZIs setting is not strict because, as long as there are no losses in their open arms, the subsequent system can compensate any loss-less modification.

To use the device with a spatially continuous beam, different portions of the beam have to be coupled into different waveguides. There can be used a single grating coupler [115] on each waveguide forming phased array-antennas [116]. With large and 2D arrays it can be necessary to pass the waveguides between the grating couplers obtaining a non perfect fill factor as in Fig. B.3a or lenslets arrays can be used above the system to focus the beam portions onto the grating couplers to improve the fraction of the beam that impinges on them as in Fig. B.3b.

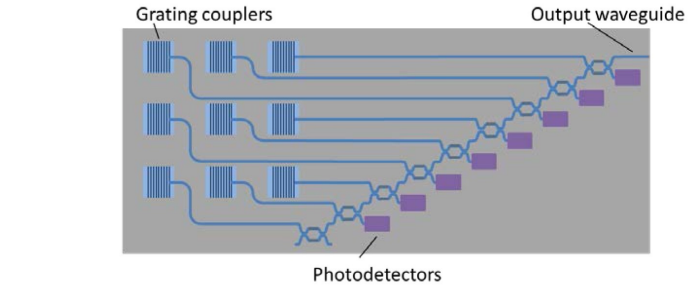

(a)

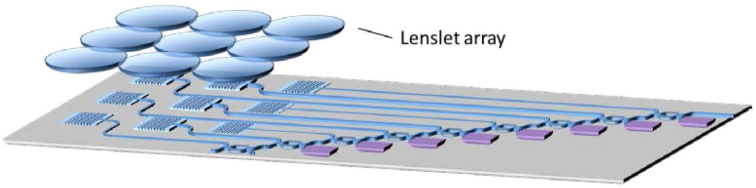

(b)

Figure B.3: *Beam coupler with two-dimensional gratings array a) with an imperfect fill factor and b) with lenslets to focus the beam on the grating couplers. (Source: [114])*

B.2.3 Multiple orthogonal beam separation

These concepts can be extended just like in Fig. B.1b to detect multiple orthogonal modes simultaneously. The main difference of the device in Fig. B.4 with respect the single output implementation is the type of detectors needed: to allow light to be processed by a multilevel system, detectors have to be mostly transparent sampling just a tiny portion of power and transmitting the rest. Having those, once set the "top" row of phase shifters and reflectors if a second orthogonal beam is shined on the device it will transmit completely through the first row. This happens because for any loss-less beam coupler that couples all of one input mode into a single output mode it is impossible to combine any power from any other orthogonal beam into the same output mode. And the second beam, having nowhere else to go, it will all pass through to the second row of *BS* blocks. Surely, the beam form will be affected by the first row crossing, but the second row can adapt to an arbitrary beam as well just using the same alignment process to direct all of the power to the second output.
Just adding rows allow the device to separate an increasing number of orthogonal beams, even with 2D gratings array. To recognize the orthogonal beams it can be used some sort of a coding to label them, like a small

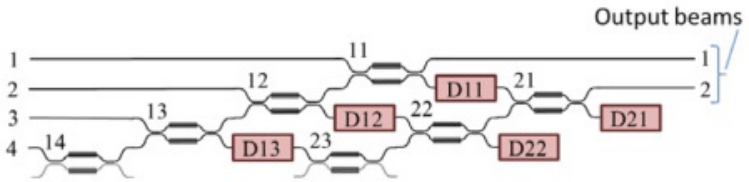

Figure B.4: *Device scheme with more than one output, in perfect accordance to Fig. B.1b. (Source: [114])*

amplitude modulation at different frequencies: now detectors of each row can be set to detect a particular frequency and the feedback loop to minimize the associated power on each detector, coupling the mode on the right output.

Potential applications of such device include automatic compensation for misalignment and defocusing of an input beam, coupling of complex modes or multiple beams from fibers or free space to single-mode guides, and retaining coupling to a moving source.

B.3 Universal linear optical device

The just seen device it is a mode converter that translates the modes from a volume to another. Being able to operate this conversion, a similar machine could do the opposite process. Therefore it is possible to change modes space, process them separately and then re-join them in the original space [20].

B.3.1 Device concept for spatial beams

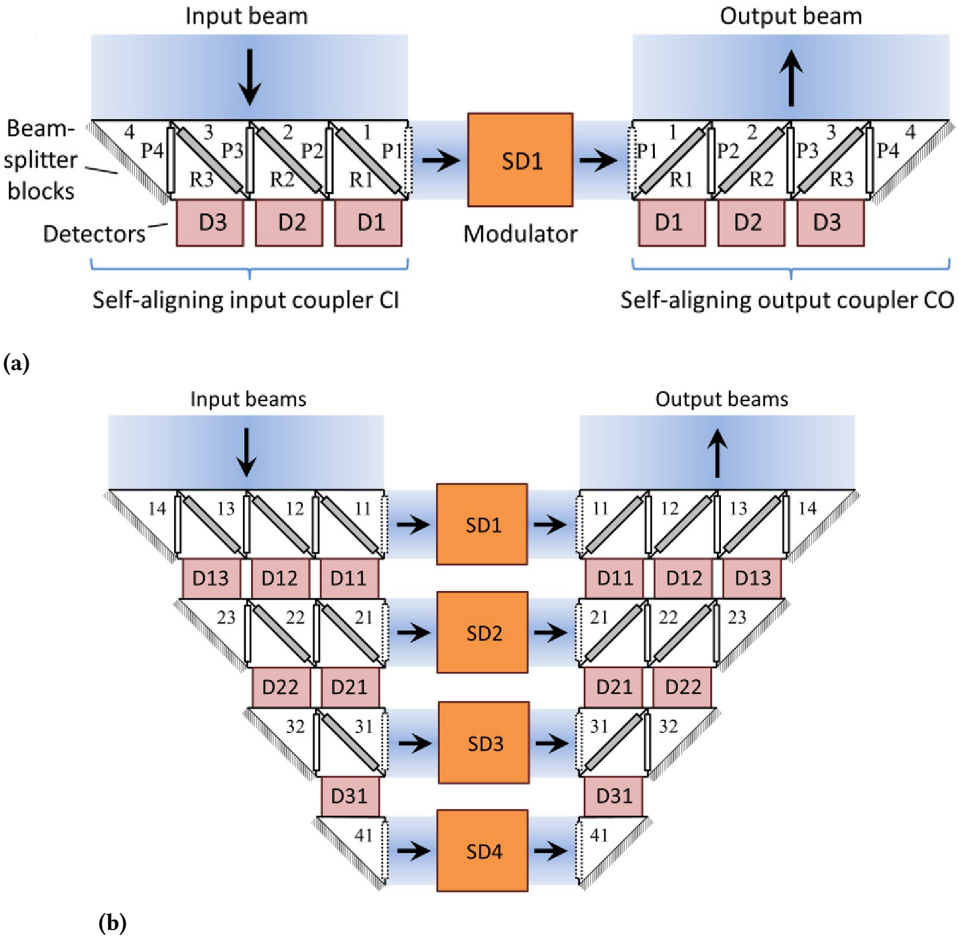

Figure B.5: *Schematic illustration of the self-configuring device. Configurations for a) one input and output beam pair and b) four possible beam pairs. (Source: [20])*

In Fig. B.5 it is showed the conceptual approach for an arbitrary device operating on spatial modes with the inputs and outputs sampled to four

channels. It is constituted by two self-aligning beam couplers: one, CI, at the input and a second, CO at the output. These two are back-to-back connected through modulators that can set amplitude and phase and can also include gain stages. Knowing what the device has to do, any linear component can be completely described this way. The simplest operation is to convert a specific spatial input mode to one specific spatial output mode.

The input coupler CI of the device in Fig. B.5a can be shined with the input mode and then tuned according to [20] as described before in order to obtain all the power in the input mode to emerge in the single output beam on the right.
The second part of the training is to shine a reversed (i.e. phase conjugated) version of the desired specific output mode onto the output coupler CO and tune the BS blocks accordingly to a similar process used for CI, which will lead to the reversed beam emerging from the left of the row of BS blocks, going backward into modulator SD_1. Having this step done, if a simple beam is shined from the output of the modulator SD_1 into CO, all the power will come out of the top of CO and the resulting field magnitudes of beams emitted from the top of the beam splitters will be the same as the ones incident during the training.

So with the device trained this way, shining the desired input mode onto CI will lead the desired output mode emerging from CO. It is finally possible to set the modulator SD_1 to get the desired overall amplitude and phase in the emerging beam.

The same process can be extended to more orthogonal beams. In Fig. B.5b it is showed a device that, after having trained the first row of BS blocks, i.e. having set the first desired input and output beams, it can be trained for the second row of BS. Since the device is now set so that all of the first beam shined onto CI will emerge into modulator SD_1, any second beam orthogonal to the previous one will instead pass entirely into the photodetectors , being fully transmitted through them to the second row of BS. The process can obviously continue until the third row is trained. At that point, due to orthogonality requirements, the fourth orthogonal pair is automatically defined.

A practical solution for implementations is the same as the one for the self-aligning universal beam coupler: Mach-Zehnder Interferometers in waveguide configuration. This is no different from the device in Fig. B.5b, and also this time a two-dimensional array can be implemented, to perform optical operations over beams that have more than just one varying direction.

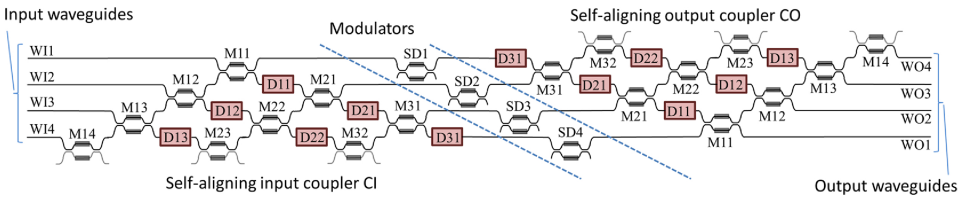

Figure B.6: *Planar layout of universal device in Fig. B.5b with MZIs. (Source: [20])*

B.3.2 Mathematical discussion

Mathematically speaking, any linear optical device can be described in terms of a linear device operator D that relates an input wave $|\phi_I\rangle$ to an output wave $|\phi_O\rangle$

$$|\phi_O\rangle = D\,|\phi_I\rangle\,. \tag{B.10}$$

It can be demonstrated that any linear operator D corresponding to a linear physical wave interaction in a device can be factorized using the singular value decomposition SVD, yielding to

$$D = \sum_m s_{Dm}\,|\phi_{DOm}\rangle\langle\phi_{DIm}| \iff D = V D_{diag} U^\dagger \tag{B.11}$$

where U is a unitary matrix operator that has the vectors $|\phi_{DIm}\rangle$ as column vectors, V has $|\phi_{DOm}\rangle$ as column vectors and D_{diag} is a diagonal matrix with complex elements s_{Dm}. The column vectors form complete orthonormal sets for describing input and output spaces H_I and H_O. The resulting singular values and the operators are uniquely specified: an input $|\phi_{DIm}\rangle$ leads to an output $s_{Dm}\,|\phi_{DOm}\rangle$, so these pairs of vectors define the orthogonal mode-converter channel through the device.

The input space can be described with a number M_I of modes, while the output one requires M_O modes. Going through the device there are M_C orthogonal channels. If M_C us equal to the smaller of M_I or M_O, then the device is maximally connected, i.e. it has the largest number of possible orthogonal channels from input to output given the dimensionalities of the input and output spaces.

In general M_I, M_C and M_O are different values so it is useful to define U as an $M_I \times M_C$ matrix ($U^\dagger$ is a $M_C \times M_I$ matrix) and V as an $M_O \times M_C$ matrix. In this way D_{diag} is an $M_C \times M_C$ square diagonal matrix with the s_{Dm} elements.

In the device of Fig. B.5, the input coupler CI corresponds to the matrix $U^\dagger$, the modulators line corresponds to the diagonal line of possibly

nonzero diagonal elements in D_{diag}, and the output coupler CO corresponds to the matrix V.

Without entering too much into details, it can be retrieved a direct relation between the number of adjustable parameters in the physical devices and the complexity number N_D of real numbers required to specify the device according to [117]. The number of independent real numbers required to specify the M_I-dimensional vector $|\phi_{DI1}\rangle$ (choose an arbitrary specific first output beam) is $2M_I - 2$ where the -2 comes from the vector normalization (which removes one degree of freedom) and the arbitrarity of the overall phase of such a vector (removing another degree of freedom). This number exactly corresponds to the number of adjustable parameters in the devices in the first row of the self-aligning coupler CI. The number of independent real numbers required to specify $|\phi_{DI2}\rangle$ is $2M_I - 4$, so smaller by 2, due to the required orthogonality of both real and imaginary parts of $\langle \phi_{DI2}|\phi_{DI1}|\phi_{DI2}|\phi_{DI1}\rangle = 0$.
By following this approach, the total complexity number N_D of real numbers required to specify a maximally functional device is generally

$$N_D = 2M_C(M_I + M_O - M_C). \tag{B.12}$$

that indicates the total number of physically adjustable parameters in a such device.

To conclude, there is at least one building method to design an arbitrary linear optical component able of any linear mapping. This include spatial, polarization and spectral mapping in any combination. In the view of extension of the self-aligning universal beam coupler, this device can be self-configuring with the solely use of simple feedback loops to optimize one parameter at a time, avoiding complex calculations of analog values with interferometric precision in optical components collections. Simultaneous and separately modulated conversions from multiple orthogonal inputs to corresponding orthogonal outputs is possible as well with this approach. These concepts, although discussed for optics, can be applied to other linear wave problems like radio-frequency electromagnetics, acoustics, quantum mechanical waves and superpositions.
The optics field is the main considered one because of the practical possibilities thanks to the current planar optical technology.

B.4 Automatic free space communication channels

Establish optimal interconnections, communication channels or beams with waves is of great importance in many applications in several fields. For example, the increasing technological performances require the consideration of spatial degree of freedom in multimode optical fibers to have more orthogonal communication channels. Of course the use of self-aligning channels can be very useful in free-space communication or interconnects. Difficulties are encountered when there is scattering effects between simple channels during propagation. In radio frequency multiple-input multiple-output (MIMO) systems the known techniques to overcome the issue require knowledge and measurement of the transmission matrix between transmitting and receiving antennas. Those schemes necessitate extensive mathematical calculation to evaluate the necessary channels, with SVD of the transmission matrix. Optical phase conjugation can perform an optimization without measurements nor calculations, but it only find the most strongly coupled SVD channel and suitable nonlinear optical materials are needed. Moreover, multiple optical channel schemes have the added difficulty of losslessly combine or separate channels: in radio-frequency measurements and calculations do the job, in optics it is often impossible to measure the field right at the input and the generation of an arbitrary optical wave from some desired computed form is still debated. The challenge of establish multiple power-optimal orthogonal channels through arbitrary linear scatterers without measuring the wave field or the transmission matrix is of great importance.

B.4.1 Single channel optimization

The description of how this goal can be performed [118] with the use of the device previously described starts considering Fig. B.7. A beam from an external inward source shines onto the grating couplers, which represent the inputs of a self-aligning universal beam coupler. The MZI are adjusted to couple essentially all the light into one single-mode input/output waveguide (orange-colored arrow).
After this setting, a "backward wave" is shined into the single-mode input/output waveguide (red-colored arrow). The wave will experience the same phase delays and amplitude splitting as the inward wave did propagating in the opposite direction. The set of complex amplitudes in the single-mode waveguides W_1 – W_4 connected to the grating couplers can be seen as a supermode of those single-mode guides. The result is that the backward wave going into the grating couplers represent the phase

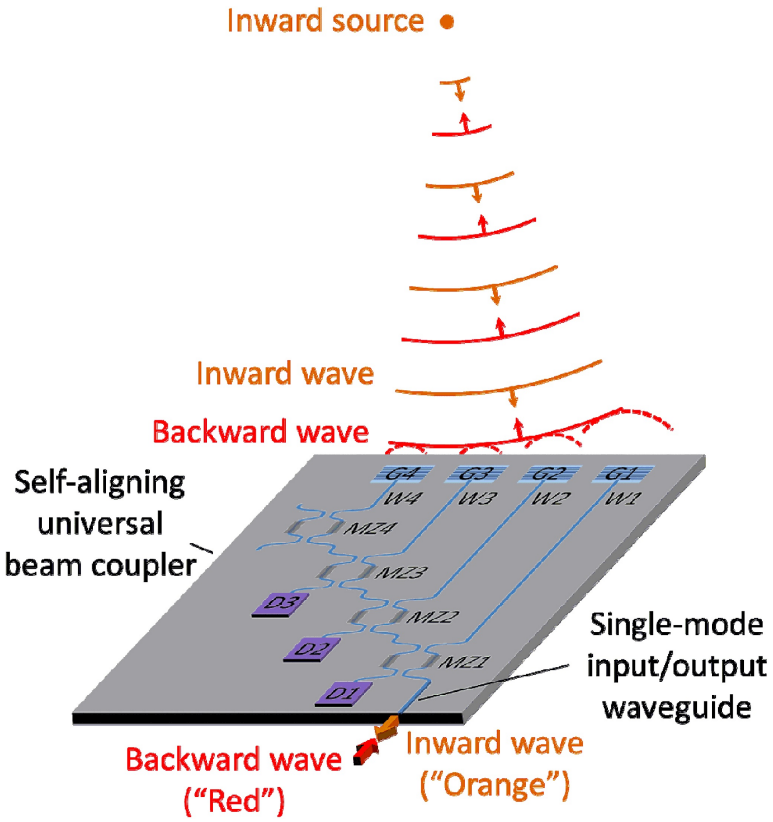

Figure B.7: *Illustration of bidirectional optimized coupler from free space to waveguide and viceversa. (Source: [20])*

conjugate version [119, 120] of the inward wave coming from the couplers. Therefore the grating couplers excite a phase conjugate wave in the free space and that wavefront will retrace exactly the same path back to the source: the working principle is exactly the same also in presence of a scattering medium. In Fig. B.7 the orange phase front will arrive last at the grating coupler G_1, hence when running backward the phase front will get first to G_1, generating the red-colored phase front.

The device is only sampling the wavefront, but according to Huygens' principle [121, 122] the wavelets from the couplers construct their best representation of the red-colored backward propagating phase fonts. Obviously a denser coupler array will generate a better representation of the wave.

This device is already useful to communicate with the source, establishing an efficient backward channel. In some cases, there is no need to power the system since there is the possibility to use the exiting orange wave to power the feedback loop and reflect the rest of it allowing a simplified scheme for remote applications e.g. environment and biological in-vivo sensing.
Moreover, letting the feedback loop running, it is possible to keep trace of a radiating object or, propagating the beam backward, it is possible to trace the position of a generic object making use of the reflected light.

List of publications

A list of publications and achievements that are fruit of this work.

Patents

1 Andrea Melloni, Francesco Morichetti, Ji Ruiqiang, Douglas Oliveira De Aguiar, Maziyar Milanizadeh, Zhou Sujie, Li Yanbo, Luo Long, Zeng Li. "Upload and download filter and optical add-drop multiplexer". International and Us patent. Huawei Technologies Co. Ltd. Application number 18878769.1-1220 PCT/CN2018083036

2 Andrea Melloni, Francesco Morichetti, Maziyar Milanizadeh, Ji Ruiqiang, Guangcan Mi, Zecen Zhang. "Add/Drop Filter, Optical Add/Drop Multiplexer, And Wavelength Control Method". Huawei Technologies Co. Ltd., Politecnico Di Milano. Filed for patent,

3 Andrea Melloni, Francesco Morichetti, Maziyar Milanizadeh, Matteo Petrini, "Testing e calibrazione di circuiti ottici integrati". Patent file in preparation,

Journal papers

1 Maziyar Milanizadeh, Douglas Aguiar, Andrea Melloni, and Francesco Morichetti. Canceling thermal cross-talk effects in photonic integrated circuits. *J. Lightwave Technol.*, 37(4):1325–1332, Feb 2019

2 M. Milanizadeh, S. Ahmadi, M. Petrini, D. Aguiar, R. Mazzanti, F. Zanetto, E. Guglielmi, M. Sampietro, F. Morichetti, and A. Melloni. Control and

calibration recipes for photonic integrated circuits. *IEEE Journal of Selected Topics in Quantum Electronics*, 26(5):1–10, 2020

3 Douglas Oliveira Morais de Aguiar, Maziyar Milanizadeh, Emanuele Guglielmi, Francesco Zanetto, Giorgio Ferrari, Marco Sampietro, Francesco Morichetti, and Andrea Melloni. Automatic tuning of silicon photonics microring filter array for hitless reconfigurable add–drop. *Journal of Lightwave Technol.*, 37(16):3939–3947, Aug 2019

4 F. Morichetti, M. Milanizadeh, M. Petrini, D. Aguiar, F. Zanetto, M. Sampietro, and A. Melloni. Polarization-transparent silicon photonic add-drop multiplexer with wideband hitless tuneability. *Nature Photonics*, 2020 Under Review

5 M. Milanizadeh, Tigers Jonuzi, Piero Borga, F. Morichetti, and A. Melloni. Free space optical beam manipulation with integrated silicon photonic mesh. *Optica*, 2020 Under Review

6 Francesco Zanetto, Vittorio Grimaldi, Fabio Toso, Emanuele Guglielmi, Maziyar Milanizadeh, Douglas Aguiar, Miltiadis Moralis-Pegios, Stelios Pitris, Theoni Alexoudi, Francesco Morichetti, Andrea Melloni, Giorgio Ferrari, and Marco Sampietro. Dithering-based real-time control of complex silicon photonic architectures by means of non-invasive detectors. *IET research journals*, 2020 Under Review

7 Francesco Zanetto, Alessandro Perino, Matteo Petrini, Fabio Toso, Maziyar Milanizadeh, Francesco Morichetti, Andrea Melloni, Giorgio Ferrari, and Marco Sampietro. Electrical conductance of silicon photonic waveguides. *Optics Letters*, 2020 Under Review

Conferences

1 Maziyar Milanizadeh, Matteo Petrini, Francesco Morichetti, and Andrea Melloni. Fsr-free filter with hitless tunability across c+l telecom band. In *Advanced Photonics Conference 2020 (IPR)*. Optical Society of America, 2020

2 Maziyar Milanizadeh, Elena Damiani, Tigers Jonuzi, Mario Junior Mencagli, Brian Edwards, David A.B. Miller, Nader Engheta, Andrea Melloni, and Francesco Morichetti. Recursive mzi mesh for integral equation implementation. In *European Conference on Integrated Optics 2020 (ECIO)*, 2020

3 Maziyar Milanizadeh, Matteo Petrini, Francesco Morichetti, and Andrea Melloni. Polarization insensitive tunable hitless filter for extended c band. In *European Conference on Integrated Optics 2020 (ECIO)*, 2020

4 Matteo Petrini, Maziyar Milanizadeh, Francesco Morichetti, and Andrea Melloni. Fsr free coupled microring resonator filter on extended c-band in silicon photonics. In *European Conference on Integrated Optics 2020 (ECIO)*, 2020

5 M. Milanizadeh, T. Jonuzi, F. Toso, G. Ferrari, M. Sampietro, D.A.B. Miller, A. Melloni, , and F. Morichetti. Control of programmable photonic integrated meshes for free-space optics applications. In *Advanced Photonics Conference 2020 (PSC)*. Optical Society of America, 2020

6 M. Milanizadeh, P. Borga, F. Morichetti, D. A. B. Miller, and A. Melloni. Manipulating free-space optical beams with a silicon photonic mesh. In *2019 IEEE Photonics Society Summer Topical Meeting Series (SUM)*, pages 1–2, 2019

7 Maziyar Milanizadeh, Douglas Aguiar, Francesco Morichetti, and Andrea Melloni. Automatic look up table generation technique for photonic integrated circuits. In *European Conference on Integrated Optics 2019 (ECIO)*, 2019

8 M. Milanizadeh, D. Aguiar, M. Petrini, E. Guglielmi, F. Zanetto, F. Toso, F. Morichetti, and A. Melloni. Automatic tuning and locking of hitless add-drop filters. In *2019 IEEE 16th International Conference on Group IV Photonics (GFP)*, pages 1–2, 2019

9 M. Milanizadeh, P. Borga, F. Morichetti, D. A. B. Miller, and A. Melloni. Manipulating free-space optical beams with a silicon photonic mesh. In *2019 IEEE Photonics Society Summer Topical Meeting Series (SUM)*, pages 1–2, 2019

10 M. Milanizadeh, S. Ahmadi, D. Aguiar, A. Melloni, and F. Morichetti. Efficient thermal cross-talk effect cancelation in photonic integrated circuits. In *2019 Optical Fiber Communications Conference and Exhibition (OFC)*, pages 1–3, 2019

11 M. Milanizadeh, D. Aguiar, F. Morichetti, and A. Melloni. Automatic configuration and wavelength locking of coupled micro-ring resonators

in presence of thermal cross-talk. In *2018 20th International Conference on Transparent Optical Networks (ICTON)*, pages 1–4, 2018

12 M. Milanizadeh, D. Melati, A. Waqas, F. Morichetti, and A. Melloni. Tuning and locking of integrated optical filters and circuits. In *2017 International Conference on Numerical Simulation of Optoelectronic Devices (NUSOD)*, pages 177–178, 2017

13 Maziyar Milanizadeh, Douglas Aguiar, Sara Ahmadi, Francesco Morichetti, and Andrea Melloni. A tuning method for photonic integrated circuits in presence of thermal cross talk. In *European Conference on Integrated Optics 2020 (ECIO)*, 2020

14 Maziyar Milanizadeh, Douglas Aguiar, Francesco Morichetti, and Andrea Melloni. Automatic tuning of microring-based hitless reconfigurable add-drop filters. In *European Conference on Integrated Optics 2020 (ECIO)*, 2020

15 Douglas Aguiar, Maziyar Milanizadeh, Emanuele Guglielmi, Francesco Zanetto, Ruiqiang Ji, Sujie Zhou, Yanbo Li, Xiaolu Song, Lewei Zhang, Marco Sampietro, Francesco Morichetti, and Andrea Melloni. Automatic tuning of microring-based hitless reconfigurable add-drop filters. In *Optical Fiber Communication Conference*, page W2A.41. Optical Society of America, 2018

16 Douglas Aguiar, Maziyar Milanizadeh, Emanuele Guglielmi, Francesco Zanetto, Marco Sampietro, Francesco Morichetti, and Andrea Melloni. Automatic hitless reconfiguration of silicon photonics microring filters (Conference Presentation). In *Silicon Photonics: From Fundamental Research to Manufacturing*, volume 10686. International Society for Optics and Photonics, SPIE, 2018

List of Figures

List of abbreviations

BER	Bit Error Rate. 3, 9, 13, 41, 65, 69, 70, 98–100, 173, 177
CLIPP	ContactLess Integrated Photonic Probe. 17, 18, 20, 24, 60, 61, 63, 65, 73, 74, 81, 105, 106, 116, 169, 173–175, 177
CMOS	Complementary Metal Oxide Semiconductor. 18, 116, 117
DP-QPSK	Double Polarization - Quadrature Phase Shift Keying. 68, 74, 76, 174
DSP	Digital Signal Processing. 9, 24, 65
DWDM	Dense Wavelength Division Multiplexing. 2, 11, 13, 61, 73, 75, 98, 138, 142
FPGA	Field Programmable Gate Array. 24, 73, 75
FSR	Free Spectral Range. 3, 11, 13, 42, 46, 60, 63, 66, 68, 72, 73, 84–92, 143, 145–147, 175
GDSII	Graphic Database System. 17
Ge	Germanium. 16
InP	Indium Phosphide. 16, 17
$LiNbO_3$	Lithium Niobate. 19
LUT	Look Up Table. 2, 10, 12, 59, 72, 73, 75, 82, 130, 139
MFD	Mode Field Diameter. 25, 27
MPW	Multi Project Wafer. 114, 140
MRR	Microring Resonator. 3, 7, 11, 35, 36, 39, 41–44, 46–49, 51–54, 56–58, 61–63, 66–70, 72, 73, 83–89, 91–96, 142, 144, 146, 171–173, 175, 176
MZ	Mach-Zehnder. 22, 60, 61, 79, 84

MZI	Mach-Zehnder Inteferometer. 3, 7, 11, 13, 29, 35, 36, 39, 40, 44–46, 57, 60, 63, 64, 66, 67, 73, 74, 78–81, 86, 101–108, 110–112, 116, 119, 130, 138, 171, 173–175, 177, 178
NRZ	Non Return to Zero. 23
OOK	On-Off Keying. 42, 44, 47, 49, 50, 66, 68–70, 74–77, 172–174
OSNR	Optical Signal to Noise Ratio. 98–100, 177
PAM-4	4-Level Pulse Amplitude Modulation. 23
PC	Personal Computer. 46, 68
PDK	Photonic Design Kit. 28
PDL	Polarization Dependent Loss. 23, 34, 84, 96
PIC	Photonic Integrated Circuit. 1–3, 6–10, 12, 13, 15, 18, 20, 21, 23–25, 29, 35–38, 40, 41, 44, 46, 51–54, 57–60, 62, 63, 65, 66, 68, 71–73, 77, 79, 82, 91, 98, 101, 116, 117, 137, 138, 140, 146, 169, 170, 178
PRC	Polarization Rotator and Combiner. 33, 34, 96, 98, 170
PSD	Power Spectral Density. 9, 10, 12, 65, 66, 68, 70–72, 74, 82, 174
PSR	Polarization Splitter and Rotator. 33, 34, 96, 98, 170
QPSK	Quadrature Phase Shift Keying. 74–77, 90, 98, 99, 174, 177
RF	Radio Frequency. 58
SEM	Scanning Electron Microscope. 26, 27, 169
Si	Silicon. 16, 17, 26, 73
SiO_2	Silicon Dioxide. 27, 125
SiON	Silicon Oxynitride. 20, 46–48, 52, 61, 62, 67–69, 172, 173
SiP	Silicon Photonics. 7, 11, 16, 17, 19, 20, 25, 26, 28, 29, 33, 83, 84, 96, 101, 107, 108, 116, 117, 123, 169, 170, 178
SNR	Signal to Noise Ratio. 24
SOI	Silicon On Insulator. 28, 72
TE	Transverse Electric. 27, 30, 33, 96
TEC	Thermo Electric Cooler. 18, 47, 49
TED	Thermal eigenmode Decomposition. 9, 10, 12, 36–52, 54, 57, 58, 62, 66–68, 72, 110, 137, 139, 170–173
TIA	Trans-Impedance Amplifier. 24, 61, 80
TiN	Titanium Nitride. 19, 86, 89, 92, 93, 107, 116, 175, 176
TM	Transverse Magnetic. 27, 33, 96
TPA	Two Photon Absorption. 139
VOA	Variable Optical Attenuator. 23, 79, 84, 91–98, 176
WDM	Wavelength Division Multiplexing. 10, 12, 33, 59–61, 82, 83, 85, 91, 93, 141, 142, 144–146, 176

Bibliography

[1] C. R. Doerr. Proposed architecture for mimo optical demultiplexing using photonic integration. *IEEE Photonics Technology Letters*, 23(21):1573–1575, 2011. 6

[2] David A. B. Miller. Reconfigurable add-drop multiplexer for spatial modes. *Opt. Express*, 21(17):20220–20229, Aug 2013. 6

[3] N. K. Fontaine, C. R. Doerr, M. A. Mestre, R. R. Ryf, P. J. Winzer, L. L. Buhl, Y. Sun, X. Jiang, and R. Lingle. Space-division multiplexing and all-optical mimo demultiplexing using a photonic integrated circuit. In *OFC/NFOEC*, pages 1–3, 2012. 6

[4] David A. B. Miller. Device requirements for optical interconnects to cmos silicon chips. In *Integrated Photonics Research, Silicon and Nanophotonics and Photonics in Switching*, page PMB3. Optical Society of America, 2010. 6

[5] Papichaya Chaisakul, D. Marris-Morini, Jacopo Frigerio, Daniel Chrastina, Said Rouifed, Stefano Cecchi, Paul Crozat, Giovanni Isella, and Laurent Vivien. Integrated germanium optical interconnects on silicon substrates. *Nature Photonics*, 8:482–488, 05 2014. 6

[6] Lian-Wee Luo, Noam Ophir, Christine Chen, Lucas Gabrielli, Carl Poitras, Keren Bergmen, and Michal Lipson. Wdm-compatible mode-division multiplexing on a silicon chip. *Nature communications*, 5:3069, 01 2014. 6

[7] Tom Claes, Wim Bogaerts, and Peter Bienstman. Experimental characterization of a silicon photonic biosensor consisting of two cascaded ring resonators based on the vernier-effect and introduction of a curve fitting method for an improved detection limit. *Opt. Express*, 18(22):22747–22761, Oct 2010. 6

[8] M. Iqbal, M. A. Gleeson, B. Spaugh, F. Tybor, W. G. Gunn, M. Hochberg, T. Baehr-Jones, R. C. Bailey, and L. C. Gunn. Label-free biosensor arrays based on silicon ring resonators and high-speed optical scanning instrumentation. *IEEE Journal of Selected Topics in Quantum Electronics*, 16(3):654–661, 2010. 6

[9] Vittorio Passaro, Mario La Notte, Benedetto Troia, Lorenzo Passaquindici, Francesco De, and Giovanni Giannoccaro. Photonic structures based on slot waveguides for nanosensors: State of the art and future developments. *International Journal of Research and Reviews in Applied Sciences*, 11:411–427, 06 2012. 6

[10] R. Waterhouse and D. Novack. Realizing 5g: Microwave photonics for 5g mobile wireless systems. *IEEE Microwave Magazine*, 16(8):84–92, 2015. 6

[11] J. Capmany and P. Muñoz. Integrated microwave photonics for radio access networks. *Journal of Lightwave Technology*, 32(16):2849–2861, 2014. 6

[12] Joshua Silverstone, Damien Bonneau, K. Ohira, N. Suzuki, H. Yoshida, Norio Iizuka, M. Ezaki, Chandra Natarajan, Michael Tanner, Robert Hadfield, V. Zwiller, G. Marshall, J. Rarity, Jeremy O'Brien, and M. Thompson. On-chip quantum interference between silicon photon-pair sources. *Nature Photonics*, 8, 01 2014. 6

[13] Smit, Leijtens, Ambrosius, Erwin Bente, Van Tol, Smalbrugge, De Vries, Geluk, Jeroen Bolk, P.J. Veldhoven, L.M. Augustin, Thijs, Domenico D'Agostino, H. Rabbani-Haghighi, Lawniczuk, Stanislaw Stopinski, Saeed Tahvili, Corradi, Kleijn, and Gilardi Giovanni. An introduction to inp-based generic integration technology. *Semiconductor Science and Technology*, 29:1–41, 06 2014. 6

[14] Jie Sun, Erman Timurdogan, Ami Yaacobi, Ehsan hosseini, and M.R. Watts. Large-scale nanophotonic phased array. *Nature*, 493:195–9, 01 2013. 6, 7

[15] Amin Vahdat, Hong Liu, Xiaoxue Zhao, and Chris Johnson. The emerging optical data center. 03 2011. 6

[16] Keren Bergman, John Shalf, and Tom Hausken. Optical interconnects and extreme computing. *Opt. Photon. News*, 27(4):32–39, Apr 2016. 6

[17] D. A. B. Miller. Device requirements for optical interconnects to silicon chips. *Proceedings of the IEEE*, 97(7):1166–1185, 2009. 6

[18] Tom Baehr-Jones, Thierry Pinguet, Patrick Guo-Qiang, Steven Danziger, Dennis Prather, and Michael Hochberg. Myths and rumours of silicon photonics. *Nature Photonics - NAT PHOTONICS*, 6:206–208, 03 2012. 6

[19] Robert Chau, Barney Doyle, S. Datta, J. Kavalieros, and Kevin Zhang. Integrated nanoelectronics for the future. *Nature materials*, 6:810–2, 12 2007. 6

[20] David A. B. Miller. Self-configuring universal linear optical component [invited]. *Photonics Research*, 2013. 6, 16, 164, 165, 166, 169

[21] Yichen Shen, Nicholas C. Harris, Scott Skirlo, Mihika Prabhu, Tom Baehr-Jones, Michael Hochberg, Xin Sun, Shijie Zhao, Hugo Larochelle, Dirk Englund, and et al. Deep learning with coherent nanophotonic circuits. *Nature Photonics*, 11(7):441–446, Jun 2017. 7, 35, 103

[22] Daniel Pérez, Ivana Gasulla, Lee Crudgington, David J Thomson, Ali Z Khokhar, Ke Li, Wei Cao, Goran Z Mashanovich, and José Capmany. Author correction: Multipurpose silicon photonics signal processor core. *Nature communications*, 8(1):1925, November 2017. 7, 9, 35, 36

[23] Jacques Carolan, Christopher Harrold, Chris Sparrow, Enrique Martín-López, Nicholas J. Russell, Joshua W. Silverstone, Peter J. Shadbolt, Nobuyuki Matsuda, Manabu Oguma, Mikitaka Itoh, Graham D. Marshall, Mark G. Thompson, Jonathan C. F. Matthews, Toshikazu Hashimoto, Jeremy L. O'Brien, and Anthony Laing. Universal linear optics. *Science*, 2015. 7, 35

[24] Leimeng Zhuang, Chris G. H. Roeloffzen, Marcel Hoekman, Klaus-J. Boller, and Arthur J. Lowery. Programmable photonic signal processor chip for radiofrequency applications. *Optica*, 2(10):854–859, Oct 2015. 7, 35, 142

[25] J. Komma, Christophe Schwarz, Gerd Hofmann, Daniel Heinert, and Ronny Nawrodt. Thermo-optic coefficient of silicon at 1550 nm and cryogenic temperatures. *Applied Physics Letters*, 101, 07 2012. 7

[26] Fengnian Xia, Lidija Sekaric, and Yurii Vlasov. Ultracompact optical buffers on a silicon chip. *Nature Photonics*, 1(1):65–71, 2007. 7, 35

[27] M. A. Popovic, T. Barwicz, E. P. Ippen, and F. X. Kartner. Global design rules for silicon microphotonic waveguides: Sensitivity, polarization and resonance tunability. In *2006 Conference on Lasers and Electro-Optics and 2006 Quantum Electronics and Laser Science Conference*, pages 1–2, 2006. 7

[28] Po Dong, Wei Qian, Hong Liang, Roshanak Shafiiha, Ning-Ning Feng, Dazeng Feng, Xuezhe Zheng, Ashok V. Krishnamoorthy, and Mehdi Asghari. Low power and compact reconfigurable multiplexing devices based on silicon microring resonators. *Opt. Express*, 18(10):9852–9858, May 2010. 9, 36

[29] K. Yu, C. Chen, C. Li, H. Li, A. Titriku, B. Wang, A. Shafik, Z. Wang, M. Fiorentino, P. Yin Chiang, and S. Palermo. 25gb/s hybrid-integrated silicon photonic receiver with microring wavelength stabilization. In *2015 Optical Fiber Communications Conference and Exhibition (OFC)*, pages 1–3, 2015. 10

[30] Xuezhe Zheng, Eric Chang, Philip Amberg, Ivan Shubin, Jon Lexau, Frankie Liu, Hiren Thacker, Stevan S. Djordjevic, Shiyun Lin, Ying Luo, Jin Yao, Jin-Hyoung Lee, Kannan Raj, Ron Ho, John E. Cunningham, and Ashok V. Krishnamoorthy. A high-speed, tunable silicon photonic ring modulator integrated with ultra-efficient active wavelength control. *Opt. Express*, 22(10):12628–12633, May 2014. 10, 35

[31] Robert Hunsperger. *Integrated Optics*. Springer-Verlag New York, 2009. 16

[32] Lei Qiao, Weijie Tang, and Tao Chu. 32 × 32 silicon electro-optic switch with built-in monitors and balanced-status units. *Scientific Reports*, 7:42306, 02 2017. 16, 142

[33] A. Annoni, E. Guglielmi, M. Carminati, S. Grillanda, P. Ciccarella, G. Ferrari, M. Sorel, M. J. Strain, M. Sampietro, A. Melloni, and F. Morichetti. Automated routing and control of silicon photonic switch fabrics. *IEEE Journal of Selected Topics in Quantum Electronics*, 22(6):169–176, 2016. 16, 60, 61, 65, 73

[34] Kishore Padmaraju, Dylan F. Logan, Takashi Shiraishi, Jason J. Ackert, Andrew P. Knights, and Keren Bergman. Wavelength locking and thermally stabilizing microring resonators using dithering signals. *J. Lightwave Technol.*, 32(3):505–512, Feb ts , url = http://jlt.osa.org/abstract.cfm?URI=jlt-32-3-505,. 16, 39, 57

[35] C. Sun, M. Wade, M. Georgas, S. Lin, L. Alloatti, B. Moss, R. Kumar, A. H. Atabaki, F. Pavanello, J. M. Shainline, J. S. Orcutt, R. J. Ram, M. Popović, and V. Stojanović. A 45 nm cmos-soi monolithic photonics platform with bit-statistics-based resonant microring thermal tuning. *IEEE Journal of Solid-State Circuits*, 51(4):893–907, 2016. 16, 35

[36] Erman Timurdogan, Zhan Su, Christopher Poulton, Matt Byrd, Simon Xin, Ren-Jye Shiue, Benjamin Moss, Ehsan hosseini, and M.R. Watts. Aim process design kit (aimpdkv2.0): Silicon photonics passive and active component libraries on a 300mm wafer. page M3F.1, 01 2018. 16

[37] R. Broeke. European inp photonic integrated circuit foundry platform development. In *2016 Optical Fiber Communications Conference and Exhibition (OFC)*, pages 1–3, 2016. 16

[38] M. Carminati, A. Annoni, F. Morichetti, E. Guglielmi, G. Ferrari, D. O. M. de Aguiar, A. Melloni, and M. Sampietro. Design guidelines for contactless integrated photonic probes in dense photonic circuits. *Journal of Lightwave Technology*, 35(14):3042–3049, 2017. 17

[39] Francesco Morichetti, Andrea Annoni, Marc Sorel, and Andrea Melloni. High-sensitivity in-band osnr monitoring system integrated on a silicon photonics chip. *Photonics Technology Letters, IEEE*, 25:1939–1942, 10 2013. 17

[40] Stefano Grillanda, Francesco Morichetti, Nicola Peserico, Pietro Ciccarella, Andrea Annoni, Marco Carminati, and Andrea Melloni. Non-invasive monitoring of mode-division multiplexed channels on a silicon photonic chip. *J. Lightwave Technol.*, 33(6):1197–1201, Mar ts. 17, 41, 60, 61, 65, 73

[41] D. Li, L. Zhou, L. Lu, and J. Chen. Optical power monitoring with ultrahigh sensitivity in silicon waveguides and ring resonators. *IEEE Photonics Journal*, 9(5):1–10, 2017. 18

[42] Akhilesh S. P. Khope, Takako Hirokawa, Andrew M. Netherton, Mitra Saeidi, Yujie Xia, Nicolas Volet, Clint Schow, Roger Helkey, Luke Theogarajan, Adel A. M. Saleh, John E. Bowers, and Rod C. Alferness. On-chip wavelength locking for photonic switches. *Opt. Lett.*, 42(23):4934–4937, Dec 2017. 19

[43] M. S. Akhter, P. Somogyi, C. Sun, M. Wade, R. Meade, P. Bhargava, S. Lin, and N. Mehta. Wavelight: A monolithic low latency silicon-photonics communication platform for the next-generation disaggregated cloud data centers. In *2017 IEEE 25th Annual Symposium on High-Performance Interconnects (HOTI)*, pages 25–28, 2017. 19

[44] Sangyoon Han. Large-scale silicon photonic mems switch. 2015. 19

[45] C. Hoessbacher et al. The plasmonic memristor: a latching optical switch. 2014. 19

[46] R. Amin et al. Ito-based electro-absorption modulator for photonic neural activation function. 2018. 19

[47] Arash and Kruger Joushaghani et al. Sub-volt broadband hybrid plasmonic-vanadium dioxide switches. 2013. 19

[48] J. Tao, N. W. Cheung, and C. Hu. Characterization and modeling of electromigration failures in multilayered interconnects and barrier layer materials. *IEEE Transactions on Electron Devices*, 43(11):1819–1825, 1996. 20

[49] R. Soref and B. Bennett. Electrooptical effects in silicon. *IEEE Journal of Quantum Electronics*, 23(1):123–129, 1987. 21, 22, 95, 175

[50] M. Nedeljkovic, R. Soref, and G. Z. Mashanovich. Free-carrier electrorefraction and electroabsorption modulation predictions for silicon over the 1–14- μm infrared wavelength range. *IEEE Photonics Journal*, 3(6):1171–1180, 2011. 22

[51] G. Reed, Goran Mashanovich, Frederic Gardes, and D. Thomson. Silicon optical modulators [review]. *Nature Photonics*, 4:518–526, 07 2010. 22

[52] H. Ramon, M. Vanhoecke, J. Verbist, W. Soenen, P. De Heyn, Y. Ban, M. Pantouvaki, J. Van Campenhout, P. Ossieur, X. Yin, and J. Bauwelinck. Low-power 56gb/s nrz microring modulator driver in 28nm fdsoi cmos. *IEEE Photonics Technology Letters*, 30(5):467–470, 2018. 23

[53] J. Sun, R. Kumar, M. Sakib, J. B. Driscoll, H. Jayatilleka, and H. Rong. A 128 gb/s pam4 silicon microring modulator with integrated thermo-optic resonance tuning. *Journal of Lightwave Technology*, 37(1):110–115, 2019. 23

[54] Lukas Chrostowski and Michael Hochberg. *Silicon Photonics Design: From Devices to Systems*. Cambridge University Press, 2015. 23

[55] J.A. Nelder and R. Mead. A Simplex Method for Function Minimization. *Comput. J.*, 7:308–313, 1965. 24

[56] Lianxi Jia, Chao Li, Tsung-Yang Liow, and Guo-Qiang Lo. Efficient suspended coupler with loss less than −1.4 db between si-photonic waveguide and cleaved single mode fiber. *J. Lightwave Technol.*, 36(2):239–244, Jan 20018. 27

[57] Advanced Micro Foundry. 11 science park rd, singapore 117685. `http://http://www.advmf.com//`. 33, 91, 96

[58] Zeqin Lu, Jaspreet Jhoja, Jackson Klein, Xu Wang, Amy Liu, Jonas Flueckiger, James Pond, and Lukas Chrostowski. Performance prediction for silicon photonics integrated circuits with layout-dependent correlated manufacturing variability. *Opt. Express*, 25(9):9712–9733, May 2017. 35

[59] Stefano Grillanda, Shengmeng Fu, Ruiqiang Ji, Francesco Morichetti, Nicola Peserico, Isaia Belladelli, Marco Carminati, Giorgio Ferrari, Marco Sampietro, Antoine Dentin, Alberto Dedè, Antonello Vannucci, Barry Holmes, Charalambos Klitis, Marc Sorel, and Andrea Melloni. Wavelength locking platform for dml-based multichannel transmitter on a silicon chip. In *Optical Fiber Communication Conference*, page W1E.2. Optical Society of America, 2016. 35

[60] Hasitha Jayatilleka, Kyle Murray, Miguel Ángel Guillén-Torres, Michael Caverley, Ricky Hu, Nicolas A. F. Jaeger, Lukas Chrostowski, and Sudip Shekhar. Wavelength tuning and stabilization of microring-based filters using silicon in-resonator photoconductive heaters. *Opt. Express*, 23(19):25084–25097, Sep 2015. 35, 41

[61] Hasitha Jayatilleka, Hossam Shoman, Robert Boeck, Nicolas A. F. Jaeger, Lukas Chrostowski, and Sudip Shekhar. Automatic configuration and wavelength locking of coupled silicon ring resonators. *J. Lightwave Technol.*, 36(2):210–218, Jan 2018. 35, 39

[62] J. C. C. Mak, W. D. Sacher, T. Xue, J. C. Mikkelsen, Z. Yong, and J. K. S. Poon. Automatic resonance alignment of high-order microring filters. *IEEE Journal of Quantum Electronics*, 51(11):1–11, 2015. 35, 39, 41

[63] Yu Li and Andrew W. Poon. Actively stabilized silicon microrings with integrated surface-state-absorption photodetectors using a slope-detection method. *Opt. Express*, 24(19):21286–21300, Sep 2016. 35

[64] Nicholas C. Harris, Yangjin Ma, Jacob Mower, Tom Baehr-Jones, Dirk Englund, Michael Hochberg, and Christophe Galland. Efficient, compact and low loss thermo-optic phase shifter in silicon. *Opt. Express*, 22(9):10487–10493, May 2014. 35

[65] P. DasMahapatra, R. Stabile, A. Rohit, and K. A. Williams. Optical crosspoint matrix using broadband resonant switches. *IEEE Journal of Selected Topics in Quantum Electronics*, 20(4):1–10, 2014. 35

[66] Biswajeet Guha, Jaime Cardenas, and Michal Lipson. Athermal silicon microring resonators with titanium oxide cladding. *Opt. Express*, 21(22):26557–26563, Nov 2013. 36

[67] Stevan S. Djordjevic, Kuanping Shang, Binbin Guan, Stanley T. S. Cheung, Ling Liao, Juthika Basak, Hai-Feng Liu, and S. J. B. Yoo. Cmos-compatible, athermal silicon ring modulators clad with titanium dioxide. *Opt. Express*, 21(12):13958–13968, Jun 2013. 36

[68] Liangjun Lu, Linjie Zhou, Xiaomeng Sun, Jingya Xie, Zhi Zou, Haike Zhu, Xinwan Li, and Jianping Chen. Cmos-compatible temperature-independent tunable silicon optical lattice filters. *Opt. Express*, 21(8):9447–9456, Apr 2013. 36

[69] S. Dwivedi, H. D'heer, and W. Bogaerts. A compact all-silicon temperature insensitive filter for wdm and bio-sensing applications. *IEEE Photonics Technology Letters*, 25(22):2167–2170, 2013. 36

[70] Jonathan Fisher, Anna Kodanev, and Moshe Nazarathy. Multi-degree-of-freedom stabilization of large-scale photonic-integrated circuits. *J. Lightwave Technol.*, 33(10):2146–2166, May 2015. 39, 57

[71] Robert L. Williams II and Douglas A. Lawrence. *Linear State-Space Control Systems*. John Wiley and Sons, 2007. 39

[72] Kishore Padmaraju, Lian-Wee Luo, Xiaoliang Zhu, Madeleine Glick, Raj Dutt, Michal Lipson, and Keren Bergman. Wavelength locking of a wdm silicon microring demultiplexer using dithering signals. In *Optical Fiber Communication Conference*, page Tu2E.4. Optical Society of America, 2014. 39, 57

[73] A. Melloni, F. Morichetti, G. Cusmai, R. Costa, A. Breda, C. Canavesi, and M. Martinellit. Progress in large integration scale circuits in sion technology. In *2007 9th International Conference on Transparent Optical Networks*, volume 1, pages 223–226, 2007. 46, 61

[74] The Mathworks, Inc., Natick, Massachusetts. *MATLAB version 9.6.0.1335978 (R2019a) Update 8*, 2019. 46, 114, 122

[75] Maziyar Milanizadeh, Douglas Aguiar, Andrea Melloni, and Francesco Morichetti. Canceling thermal cross-talk effects in photonic integrated circuits. *J. Lightwave Technol.*, 37(4):1325–1332, Feb 2019. 57, 70, 90, 171

[76] Andri Mahendra, Chunle Xiong, Xiang Zhang, Benjamin J. Eggleton, and Philip H. W. Leong. Multiwavelength stabilization control of a thermo-optic system with adaptive reconfiguration. *Appl. Opt.*, 56(4):1113–1118, Feb ts. 57

[77] Po Dong, Robert Gatdula, Kwangwoong Kim, Jeffrey H. Sinsky, Argishti Melikyan, Young-Kai Chen, Guilhem de Valicourt, and Jeffrey Lee. Simultaneous wavelength locking of microring modulator array with a single monitoring signal. *Opt. Express*, 25(14):16040–16046, Jul ts. 57

[78] A. Gazman, C. Browning, Z. Zhu, L. R. Barry, and K. Bergman. Automated thermal stabilization of cascaded silicon photonic ring resonators for reconfigurable wdm applications. In *2017 European Conference on Optical Communication (ECOC)*, pages 1–3, 2017. 57

[79] M. Milanizadeh, S. Ahmadi, M. Petrini, D. Aguiar, R. Mazzanti, F. Zanetto, E. Guglielmi, M. Sampietro, F. Morichetti, and A. Melloni. Control and calibration recipes for photonic integrated circuits. *IEEE Journal of Selected Topics in Quantum Electronics*, 26(5):1–10, 2020. 59, 82, 171

[80] Douglas Oliveira Morais de Aguiar, Maziyar Milanizadeh, Emanuele Guglielmi, Francesco Zanetto, Giorgio Ferrari, Marco Sampietro, Francesco Morichetti, and Andrea Melloni. Automatic tuning of silicon photonics microring filter array for hitless reconfigurable add–drop. *Journal of Lightwave Technol.*, 37(16):3939–3947, Aug 2019. 59, 61, 73, 142, 172

[81] P. Dumais, D. J. Goodwill, D. Celo, J. Jiang, C. Zhang, F. Zhao, X. Tu, C. Zhang, S. Yan, J. He, M. Li, W. Liu, Y. Wei, D. Geng, H. Mehrvar, and E. Bernier. Silicon photonic switch subsystem with 900 monolithically integrated calibration photodiodes and 64-fiber package. *Journal of Lightwave Technology*, 36(2):233–238, 2018. 65

[82] Piero Orlandi, Francesco Morichetti, Michael John Strain, Marc Sorel, Paolo Bassi, and Andrea Melloni. Photonic integrated filter with widely tunable bandwidth. *Journal of Lightwave Technol.*, 32(5):897–907, Mar 2014. 66

[83] Arnaud Dupas, Patricia Layec, Dominique Verchere, Quan Pham Van, and Sébastien Bigo. Ultra-fast hitless 100gbit/s real-time bandwidth variable transmitter with sdn optical control. In *Optical Fiber Communication Conference*, page Th2A.46. Optical Society of America, 2018. 75

[84] Hasitha Jayatilleka, Robert Boeck, Mohammed AlTaha, Jonas Flueckiger, Nicolas A. F. Jaeger, Sudip Shekhar, and Lukas Chrostowski. Automatic tuning and temperature stabilization of high-order silicon vernier microring filters. In *Optical Fiber Communication Conference*, page Th1G.4. Optical Society of America, 2017. 84, 85

[85] Y. Ren, D. Perron, F. Aurangozeb, Z. Jiang, M. Hossain, and V. Van. Silicon photonic vernier cascaded microring filter for broadband tunability. *IEEE Photonics Technology Letters*, 31(18):1503–1506, 2019. 84, 85

[86] G. Griffel. Vernier effect in asymmetrical ring resonator arrays. *Photonics Technology Letters, IEEE*, 12:1642 – 1644, 01 2001. 84, 85, 86

[87] Tymon Barwicz, M.R. Watts, Milo|[scaron] Popovi|[cacute, Peter Rakich, Luciano Socci, Franz K|[auml]|rtner, Erich Ippen, and Henry Smith. Polarization-transparent microphotonic devices in the strong confinement limit. *Nature Photonics*, 1:57–60, 12 2006. 84, 96

[88] R. Soref and B. Bennett. Transparent wavelength switching of resonant filters. In *Conference on Lasers and Electro-Optics/Quantum Electronics and Laser Science Conference and Photonic Applications Systems Technologies*, page CPDA2. Optical Society of America, 2007. 84, 91

[89] Douglas Aguiar, Maziyar Milanizadeh, Emanuele Guglielmi, Francesco Zanetto, Ruiqiang Ji, Sujie Zhou, Yanbo Li, Xiaolu Song, Lewei Zhang, Marco Sampietro, Francesco Morichetti, and Andrea Melloni. Automatic tuning of microring-based hitless reconfigurable add-drop filters. In *Optical Fiber Communication Conference*, page W2A.41. Optical Society of America, 2018. 84, 91, 174

[90] H. A. Haus, M. A. Popovic, and M. R. Watts. Broadband hitless bypass switch for integrated photonic circuits. *IEEE Photonics Technology Letters*, 18(10):1137–1139, 2006. 84

[91] Miloš A. Popović, Hermann A. Haus, and Michael R. Watts. General approach to hitless switching and fsr extension for resonators in integrated photonic circuits. In *Optical Fiber Communication Conference and Exposition and The National Fiber Optic Engineers Conference*, page OWI66. Optical Society of America, 2006. 84

[92] Rohit Chatterjee, Mingbin Yu, Aaron Stein, Dim-Lee Kwong, Lionel C. Kimerling, and Chee Wei Wong. Demonstration of a hitless bypass switch using nanomechanical perturbation for high-bitrate transparent networks. *Opt. Express*, 18(3):3045–3058, Feb 2010. 84

[93] Lukas Chrostowski and Michael Hochberg. *Silicon Photonics Design: From Devices to Systems*. 03 2015. 85, 86

[94] A. Melloni and M. Martinelli. Synthesis of direct-coupled-resonators bandpass filters for wdm systems. *Journal of Lightwave Technology*, 20(2):296–303, 2002. 86, 87

[95] Fengnian Xia, Mike Rooks, Lidija Sekaric, and Yurii Vlasov. Ultra-compact high order ring resonator filters using submicron silicon photonic wires for on-chip optical interconnects. *Opt. Express*, 15(19):11934–11941, Sep 2007. 86

[96] M. Milanizadeh, S. Ahmadi, M. Petrini, D. Aguiar, R. Mazzanti, F. Zanetto, E. Guglielmi, M. Sampietro, F. Morichetti, and A. Melloni. Control and calibration recipes for photonic integrated circuits. *IEEE Journal of Selected Topics in Quantum Electronics*, 26(5):1–10, 2020. 90, 94

[97] Method and device for hitless tunable optical filtering. 91

[98] Yurii Vlasov, William Green, and Fengnian Xia. High-throughput silicon nanophotonic wavelength-insensitive switch for on-chip optical networks. *Nature Photonics*, 2:242–246, 03 2008. 92

[99] Hugo L. R. Lira, Sasikanth Manipatruni, and Michal Lipson. Broadband hitless silicon electro-optic switch for on-chip optical networks. *Opt. Express*, 17(25):22271–22280, Dec 2009. 92

[100] P. Dainesi, A. Kung, M. Chabloz, A. Lagos, P. Fluckiger, A. Ionescu, P. Fazan, M. Declerq, P. Renaud, and P. Robert. Cmos compatible fully integrated mach-zehnder interferometer in soi technology. *IEEE Photonics Technology Letters*, 12(6):660–662, 2000. 95

[101] Antonio Mecozzi. A necessary and sufficient condition for minimum phase and implications for phase retrieval, 2016. 98

[102] D. Pérez, I. Gasulla, and J. Capmany. Toward programmable microwave photonics processors. *Journal of Lightwave Technology*, 36(2):519–532, 2018. 103

[103] Andrea Annoni, Emanuele Guglielmi, Marco Carminati, Giorgio Ferrari, Marco Sampietro, David AB Miller, Andrea Melloni, and Francesco Morichetti. Unscrambling light—automatically undoing strong mixing between modes. *Light: Science & Applications*, 6(12):e17110, 2017. 103, 118, 119

[104] Xiaogang Qiang, Jianwei Wang, Callum Wilkes, Thomas Loke, Sean O'Gara, Laurent Kling, Graham Marshall, Raffaele Santagati, Timothy Ralph, Jb Wang, Jeremy O'Brien, Mark Thompson, and Jonathan Matthews. Large-scale silicon quantum photonics implementing arbitrary two-qubit processing. *Nature Photonics*, 12, 09 2018. 103

[105] Richard Soref. Tutorial: Integrated-photonic switching structures. *APL Photonics*, 3(2):021101, 2018. 142

[106] Daniel Pérez, Ivana Gasulla, José Capmany, and Richard A. Soref. Reconfigurable lattice mesh designs for programmable photonic processors. *Opt. Express*, 24(11):12093–12106, May 2016. 142

[107] Andrea Melloni and Francesco Morichetti. *Componenti e Circuiti per le Comunicazioni Ottiche*. 2010. 147, 151

[108] Schwelb, S., Kokubun, and Y. Ultra-short optical pulse transmission characteristics of vertically coupled microring resonator add/drop filter. 19, 2001. 152, 153

[109] Robi Boeck, Nicolas A.F Jaegerand Nicolas Rouger, and Lukas Chrostowski. Series-coupled silicon racetrack resonators and the vernier effect: theory and measurement. 2010. 152

[110] Ioannis Chremmos, Otto SChweb, and Nikolaos Uzunoglu. *Photonic Microresonator Research and Applications*. 2010. 152, 153

[111] Chinda Chaichuay, Preecha P.Yupapin, and Prajak Saeung. The serially coupled multiple ring resonator filters and vernier effect. XXXIX, No. 1, 2009. 153

[112] David AB Miller. All linear optical devices are mode converters. *Optics Express*, 20(21):23985–23993, 2012. 155, 160

[113] Robert W Boyd. *Radiometry and the detection of optical radiation*. 1983. 159

[114] David A. B. Miller. Self-aligning universal beam coupler. *Optics Express*, 2013. 160, 161, 162, 163

[115] Günther Roelkens, Diedrik Vermeulen, S Selvaraja, R Halir, W Bogaerts, and D Van Thourhout. Grating-based optical fiber interfaces for silicon-on-insulator photonic integrated circuits. *IEEE Journal of Selected topics in quantum Electronics*, 17(3):571–580, 2011. 161

[116] Karel Van Acoleyen, Hendrik Rogier, and Roel Baets. Two-dimensional optical phased array antenna on silicon-on-insulator. *Optics express*, 18(13):13655–13660, 2010. 161

[117] David AB Miller. How complicated must an optical component be? *JOSA A*, 30(2):238–251, 2013. 167

[118] David AB Miller. Establishing optimal wave communication channels automatically. *Journal of Lightwave Technology*, 31(24):3987–3994, 2013. 168

[119] Amnon Yariv. Phase conjugate optics and real-time holography. *IEEE Journal of Quantum Electronics*, 14(9):650–660, 1978. 170

[120] Peter Günter. Holography, coherent light amplification and optical phase conjugation with photorefractive materials. *Physics Reports*, 93(4):199–299, 1982. 170

[121] C Huygens. Traité de la lumiere, 1690. *Lipsiae, GRESSNER e SCHRAMM ed*, pages 125–132, 2005. 170

[122] David A. B. Miller. Huygens's wave propagation principle corrected. *Optics Letter*, 1991. 170

[123] F. Morichetti, M. Milanizadeh, M. Petrini, D. Aguiar, F. Zanetto, M. Sampietro, and A. Melloni. Polarization-transparent silicon photonic add-drop multiplexer with wideband hitless tuneability. *Nature Photonics*, 2020 Under Review. 172

[124] M. Milanizadeh, Tigers Jonuzi, Piero Borga, F. Morichetti, and A. Melloni. Free space optical beam manipulation with integrated silicon photonic mesh. *Optica*, 2020 Under Review. 172

[125] Francesco Zanetto, Vittorio Grimaldi, Fabio Toso, Emanuele Guglielmi, Maziyar Milanizadeh, Douglas Aguiar, Miltiadis Moralis-Pegios, Stelios Pitris, Theoni Alexoudi, Francesco Morichetti, Andrea Melloni, Giorgio Ferrari, and Marco Sampietro. Dithering-based real-time control of complex silicon photonic architectures by means of non-invasive detectors. *IET research journals*, 2020 Under Review. 172

[126] Francesco Zanetto, Alessandro Perino, Matteo Petrini, Fabio Toso, Maziyar Milanizadeh, Francesco Morichetti, Andrea Melloni, Giorgio Ferrari, and Marco Sampietro. Electrical conductance of silicon photonic waveguides. *Optics Letters*, 2020 Under Review. 172

[127] Maziyar Milanizadeh, Matteo Petrini, Francesco Morichetti, and Andrea Melloni. Fsr-free filter with hitless tunability across c+l telecom band. In *Advanced Photonics Conference 2020 (IPR)*. Optical Society of America, 2020. 172

[128] Maziyar Milanizadeh, Elena Damiani, Tigers Jonuzi, Mario Junior Mencagli, Brian Edwards, David A.B. Miller, Nader Engheta, Andrea Melloni, and Francesco Morichetti. Recursive mzi mesh for integral equation implementation. In *European Conference on Integrated Optics 2020 (ECIO)*, 2020. 172

[129] Maziyar Milanizadeh, Matteo Petrini, Francesco Morichetti, and Andrea Melloni. Polarization insensitive tunable hitless filter for extended c band. In *European Conference on Integrated Optics 2020 (ECIO)*, 2020. 173

[130] Matteo Petrini, Maziyar Milanizadeh, Francesco Morichetti, and Andrea Melloni. Fsr free coupled microring resonator filter on extended c-band in silicon photonics. In *European Conference on Integrated Optics 2020 (ECIO)*, 2020. 173

[131] M. Milanizadeh, T. Jonuzi, F. Toso, G. Ferrari, M. Sampietro, D.A.B. Miller, A. Melloni, , and F. Morichetti. Control of programmable photonic integrated meshes for free-space optics applications. In *Advanced Photonics Conference 2020 (PSC)*. Optical Society of America, 2020. 173

[132] M. Milanizadeh, P. Borga, F. Morichetti, D. A. B. Miller, and A. Melloni. Manipulating free-space optical beams with a silicon photonic mesh. In *2019 IEEE Photonics Society Summer Topical Meeting Series (SUM)*, pages 1–2, 2019. 173

[133] Maziyar Milanizadeh, Douglas Aguiar, Francesco Morichetti, and Andrea Melloni. Automatic look up table generation technique for photonic integrated circuits. In *European Conference on Integrated Optics 2019 (ECIO)*, 2019. 173

[134] M. Milanizadeh, D. Aguiar, M. Petrini, E. Guglielmi, F. Zanetto, F. Toso, F. Morichetti, and A. Melloni. Automatic tuning and locking of hitless add-drop filters. In *2019 IEEE 16th International Conference on Group IV Photonics (GFP)*, pages 1–2, 2019. 173

[135] M. Milanizadeh, P. Borga, F. Morichetti, D. A. B. Miller, and A. Melloni. Manipulating free-space optical beams with a silicon photonic mesh. In *2019 IEEE Photonics Society Summer Topical Meeting Series (SUM)*, pages 1–2, 2019. 173

[136] M. Milanizadeh, S. Ahmadi, D. Aguiar, A. Melloni, and F. Morichetti. Efficient thermal crosstalk effect cancelation in photonic integrated circuits. In *2019 Optical Fiber Communications Conference and Exhibition (OFC)*, pages 1–3, 2019. 173

[137] M. Milanizadeh, D. Aguiar, F. Morichetti, and A. Melloni. Automatic configuration and wavelength locking of coupled micro-ring resonators in presence of thermal cross-talk. In *2018 20th International Conference on Transparent Optical Networks (ICTON)*, pages 1–4, 2018. 173

[138] M. Milanizadeh, D. Melati, A. Waqas, F. Morichetti, and A. Melloni. Tuning and locking of integrated optical filters and circuits. In *2017 International Conference on Numerical Simulation of Optoelectronic Devices (NUSOD)*, pages 177–178, 2017. 174

[139] Maziyar Milanizadeh, Douglas Aguiar, Sara Ahmadi, Francesco Morichetti, and Andrea Melloni. A tuning method for photonic integrated circuits in presence of thermal cross talk. In *European Conference on Integrated Optics 2020 (ECIO)*, 2020. 174

[140] Maziyar Milanizadeh, Douglas Aguiar, Francesco Morichetti, and Andrea Melloni. Automatic tuning of microring-based hitless reconfigurable add-drop filters. In *European Conference on Integrated Optics 2020 (ECIO)*, 2020. 174

[141] Douglas Aguiar, Maziyar Milanizadeh, Emanuele Guglielmi, Francesco Zanetto, Marco Sampietro, Francesco Morichetti, and Andrea Melloni. Automatic hitless reconfiguration of silicon photonics microring filters (Conference Presentation). In *Silicon Photonics: From Fundamental Research to Manufacturing*, volume 10686. International Society for Optics and Photonics, SPIE, 2018. 174